POLITECNICO
MILANO 1863

School of Civil, Environmental and Land Management Engineering

Master of Science in Civil Engineering

Size effects of RC interfaces subjected to shear

Supervisor: Prof. Sara Cattaneo

Author: Giovana Milaré Tortelli

Student ID number: 10775879

Academic Year 2021-2022

Table of Content

List of Figures

List of Tables

List of Graphs

Abstract

The shear transfer mechanism along interfaces between concretes of different ages and/or different mechanical properties is a complex problem, that is influenced by many parameters. It is related to applications of repair and strengthening techniques of existing buildings, such as in case of new jacketing or slab overlay, and to constructions of new structures, for instance when precast elements are used. Many authors have studied this problem and its specific applications, proposing different design equations throughout the years. It was found that there are three main shear transfer mechanisms governing the problem: adhesion, friction and dowel action.

The thesis focus on the influence of the size of the specimen and on the concrete strength of both concrete layers on the shear strength. The choice of the first topic is justified by the fact that many proposed existing design equations are based on tests conducted on small specimen, that are not necessarily representative of real structures, while recently a new bigger specimen has been proposed by the EOTA assessment. The choice of the later topic is due to the considerable influence of this parameter.

Numerical analysis, using the commercial software Abaqus, were performed for the proposed studies. To take into consideration the non-linearity of the concrete, the numerical models were elaborated using the Concrete Damaged Plasticity option, in which plasticity parameters and compressive and tensile damage curves are introduced for the modelled concretes.

Initially, a validation of the proposed numerical model was made using experimental results obtained from a research campaign that took place at Politecnico di Milano. After the validation of the model, the size effect analysis was conducted. Finally, a study was conducted on the influence of concrete strength. In the studies of both parameters, an evaluation was made on results concerning load *versus* slip curves, displacement distributions, crushing and cracking patterns and stresses distributions.

1. Chapter One: Introduction

1.1. Background

The addition of new reinforced concrete layers or elements to existing members of a structure are common practices, for instance, when performing repair and strengthening techniques in existing buildings, such as concrete jacketing and increasing of bridge decks' or building slabs' thicknesses, and when using precast elements in the construction of new buildings or bridges, which are often combined to *cast-in-situ* structural members. Examples are provided in Figure 1-1, Figure 1-2 and Figure 1-3. A connection is then established between two concrete parts of different ages and often of different mechanical properties.

Figure 1-1 Example of concrete jacketing, provided by "Jacob Engineers"

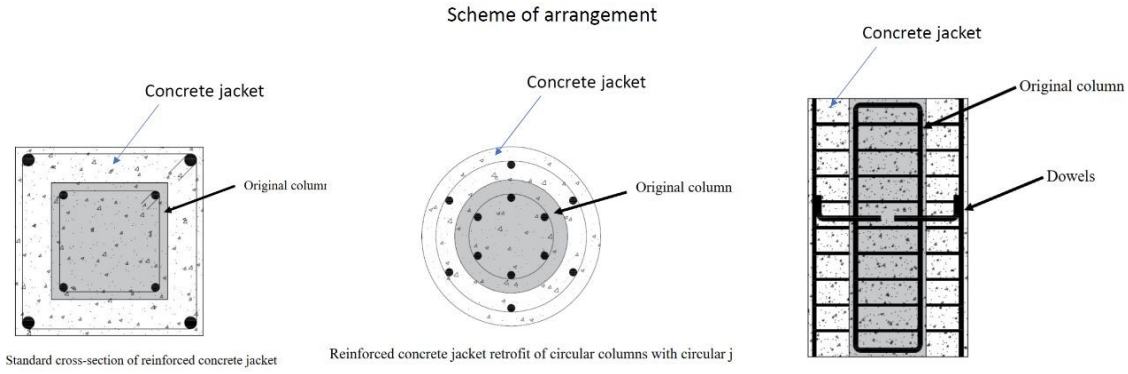

Figure 1-2 Concrete jacketing schematic explanation, provided by "Safety Assessment and Retrofitting of Existing Structures and Infrastructures" course of Politecnico di Torino

a)

b)

c)

Figure 1-3 Examples of connections in precast concrete elements, provided by Holly, I. and Abrahoim, I. (2020) (1)

The connection between the added and the existing concrete parts could become a weakness in the structure, with cracking and debonding of the interface being common problems of reinforced concrete composite member due to incompatibilities between the different materials' properties. Therefore, proper design and detailing are necessary as they should guarantee that the resulting composite element behaves in a monolithic manner. The design and detailing must also aim at ensuring sufficient load bearing resistance and proper transfer of the shear load along the concrete-to-concrete interface.

Several parameters influence the interface transfer of shear load, having effects on it on their own and by interacting with each other. Some of these parameters are related to the concrete layers' properties, such as their strength, thickness and surface

smoothness, others related to the anchorage proposed between the layers, such as the diameter and quantity of the bars, and others related to the actions on the structure, such as their type, magnitude and positioning. Most of these parameters and their interactions have been subject to many studies of different authors.

The interface shear resistance is currently evaluated based on a modified shear friction theory, which was originally developed in the 1960's by Birkeland and Birkeland (1966) (2) and Mast (1968) (3). Several studies and experimental investigations have brought further understanding about the interface shear and then proposed additions to this theory. The theory and the studies resulted on the currently accepted knowledge that the transfer of the shear load between concrete layers relies mainly on three types of mechanisms: dowel action, friction and adhesion; and on the predominant consideration of the following four parameters for design expressions: compressive strength of the concrete of lowest strength, normal stress acting at the interface, shear reinforcement at the interface and roughness of the concrete's surface, as mentioned by Santos, P.M.D. (2009) (4).

1.2. Motivation

Many of the studies conducted on the subject of connections of concrete members cast at different times and with different mechanical properties have used numerical analyses to assess the problem. The simplifying assumption of elastic linear behaviour of concrete is largely adopted in such studies and is justified by the efficiency of producing sufficiently accurate results with significantly reduced computational costs. However, as concrete has in reality a non-linear behaviour, and as the cracking process is significant for the shear transfer mechanism, the use of models that do not use the simplifying assumption of linear elasticity and allow the consideration of the damage process are expected to produce results better fitting the experimental findings. That justifies the choice made in some studies, including this one, to adopt this type of model despite its higher computational costs.

Equations indicated by different design codes of reinforced concrete structures may result in interface shear resistances that differ significantly between each other. One of the reasons for that is the lack of database differentiation between small size tests and structural member tests. Besides that, the roughness of the interface between the concrete layers, which is one of the parameters that affect the shear resistance, is evaluated using roughness coefficients. Those coefficients are mostly based on experimental test data obtained from small size tests, that are not representative of real

structures due to their size. Taking that into consideration, the study of the size effect on concrete connections' problems becomes of interest.

Finally, being the concrete's strength one of the parameters that affect the transfer mechanism of shear load, its study using finite element models derived from a model that considers the non-linear behaviour of concrete and that was validated by comparison with experimental results was also considered to be significant.

1.3. Thesis Organization

This thesis consists of five chapters, being this introduction the first one, in which a general overview on the research subject, the motivation for the development of this work and it organization are presented. The purpose and content of each chapter is briefly presented in this sub-section.

Chapter 2 is composed of a state-of-the-art review on the subject that includes an introduction to the shear friction theory and to some of the main design expressions to evaluate the shear strength at the interface between concrete pieces of different ages and mechanical properties. In addition, a recall to an experimental campaign conducted at Politecnico di Milano is presented.

In chapter 3, the details of all considered models are presented. That is done by describing the initial model created, from which others were derived. That description includes a presentation of the Concrete Damaged Plasticity model provided by Abaqus, with comments on the theory behind it and on how to obtain the input parameters that should be introduced. Other aspects relevant to the creation of the model, such as mesh creation and constraints, interactions and boundary conditions definitions were also introduced.

In chapter 4, the size effect analysis is presented. The main aim of the analysis is to evaluate the influence of the structural members' size (three different dimensions) on the shear stress produced at the interface, considering the same materials and the same applied displacement. The methodology used and the two additional finite element models created for the performance of the analysist are described. Results are presented and discussed, including the comparison of peak loads, maximum interface shear stresses and of distributions of displacements, compressive and tensile damage patterns, shear stresses at the concrete layers and of principal stresses at the anchorage bars.

Chapter 5 presents the numerical analyses performed to evaluate the effect of the concrete's strength on the resulting shear force at the interface. Two high strength

concretes classes were considered for this study: C60/75 and C90/105. The procedures followed to conduct the analyses and their results are presented. From the results, observations are made concerning the comparison of the use of normal strength concrete to the use of high strength concrete and concerning the implications of having composite reinforced concrete structures composed of a high strength layer connected to a normal strength layer.

Finally, in the final section, the conclusions obtained during all the development of this thesis are summarised.

2. Chapter Two: State of the art review

In this chapter, previous research made on the topic of connected concrete layers subjected to shear will be introduced. Many design expressions proposed by different authors throughout the years will be commented on, but most of them will not be presented in detail, as it is not the focus of this chapter to provide a list of proposed design expressions, the focus is only to introduce the theory related to each one of them. Therefore, comments were made regarding the parameters that were included in each expression, that is to say, the parameters that were considered influential for the shear stress resulting on the concrete-to-concrete interface, while experimentally calibrated constant values adopted in the expressions were not evaluated. For a review on the topic that presents the proposed equations, one can refer to by Santos, P.M.D. and Júlio, E.N.B.S. (2012) (5).

The first design expressions proposed to calculate the longitudinal shear strength of concrete-to-concrete interfaces, that were presented in the 1960s by authors such as Hanson (1960) and Anderson (1960), were simple linear expressions, in the format of a constant term (A) summed to the product of the reinforcement ratio (ρ) and another constant parameter (B) ($v = A + B * \rho$). Both constants were experimentally determined by the performance of push-off tests. However, due to the complexity of the problem of concrete-to-concrete connections, the parameters obtained should vary greatly in accordance with the parameters adopted for the performance of the tests, such as the concrete strengths and surface preparation techniques adopted, and thus they differ significantly between authors and produce expressions that could only be considered representative under specific situations.

Following design expressions proposed little modification to the first type, that was commented above. For instance, Mattock and Kaar (1961) proposed an expression in which the constant term became a function of the ratio between the shear span and effective depth of the reinforcement. Saemann and Washa (1964) proposed similar modifications to the initial expression using the shear span-effective depth ratio for the calculation of the previously constants term and multiplying parameter. Gaston and Kriz (1964) proposed expressions of same shape, but as functions of the normal stress (σ_n) at the interface in replacement of the reinforcement ratio.

The shear friction theory had it is initial developments first published in 1966, by Birkeland and Birkeland (1966) (2). This theory proposes that the transfer mechanism of shear force along the contact surface between two concrete layers, when relative slip between both layers occurs, is related to the reinforcement ratio (ρ), its yield strength

(f_y) and internal friction angle (φ). The design expression to calculate the shear stress at the concrete-to-concrete contact surface was then proposed as the multiplication of the term ρf_y, that has been named as clamping stress, by the tangent of φ. The internal friction angle parameter acknowledges the contact surface's roughness.

This theory suggests that the tensile strength of concrete should be neglected, so only the reinforcement resists to tensile forces, and that the transfer of shear forces occur only by friction, caused by action of an external normal force or of the reinforcements crossing the interface, in a mechanism that can be exemplified by a saw-tooth model as the one represented in Figure 2-1. The model represented acknowledges the influence of reinforcement crossing the interface, that compresses the surface as it is tensioned, and the action of external compression forces normal to the contact surface plane. The results obtained by using the simple proposed expression provides results with a good enough accuracy.

The expression adopted by Birkeland and Birkeland (1966) was also adopted by Mast (1968), who proposed modifications to the adopted coefficients of friction and suggested the adoption of an upper limit value.

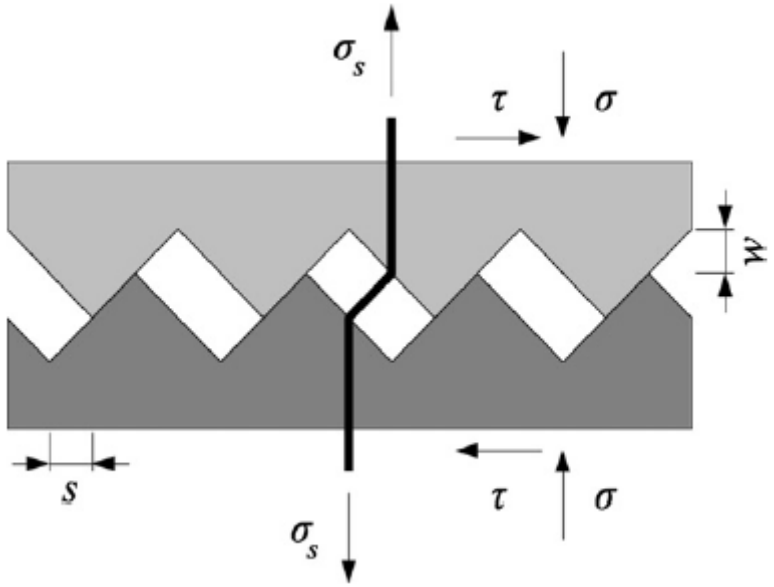

Figure 2-1 Saw-tooth model representation [Santos and Júlio (2012) (5)]

Later, in 1968, Birkeland proposed a non-linear expression for the calculation of the ultimate shear stress at the interface. In the proposed expression, the ultimate shear stress is directly proportional to the square root of the clamping stress, multiplied by an experimentally calibrated factor.

The equations proposed by some of the previously mentioned authors were studied by Hofbeck, Ibrahim and Mattock (1969), who studied the influence of some parameters on the shear strength at the contact surface between concrete layers. The design expression proposed by Birkeland and Birkeland (2) was considered too conservative by the authors, considering concrete specimens with pre-existing cracks along the shear plane. Their studies led to the conclusion that pre-existing cracks along the concrete-to-concrete interface plane can be associated with a decrease in the shear strength and an increase in the relative slip between the two concrete layers. They also concluded that, for clamping stresses of values superior to 4.14 MPa, the increase of concrete strength leads to an increase of the shear strength obtained at the interface. Additionally, they stated that the dowel action was proven to only be significant for specimens with pre-existing cracks along the interface, as the relative slip between layers was too small in initially uncracked specimens.

Mattock and Hawkins (1972) proposed a design expression similar to the initial linear expressions, of format $v = A * x + B$, but as a function of the sum of the clamping stress (ρf_y) to the external normal stress at the interface (σ_n). Upper bound limits were proposed for the ultimate longitudinal shear stress, and a lower bound limit was proposed for the clamping stress. Their expression is known as the “modified shear friction theory”. Two years later, Mattock proposed a modification of the design expression to include the orientation of the reinforcement bars that cross the concrete-to-concrete interface.

The design expressions proposed by Mattock in 1974 and by Birkeland in 1968 were evaluated in terms of their suitability for the design of concrete connections in which transfer of normal forces and bending moments occur, such as corbels and columns foundations. Both of them were found to be suitable, being Birkeland’s design expression found to be more conservative.

Raths (1977) proposed a non-linear design expression, similar to the one proposed by Birkeland in 1968, that includes a constant related to the concrete density as a parameter, in such a way that the expression becomes suitable for normal and lightweight concrete. Shaikh (1978) then proposed a modified version of the shear-friction design expression that includes the effect of the concrete density by calculating an effective coefficient of friction, which is calculated using a constant related to the concrete density as a parameter. The proposed modified expression also includes a capacity reduction factor.

The first design expression that explicitly includes the concrete compressive strength was the one proposed by Loov (1978). The expression proposed was a non-dimensional

one, in which the ratio between the ultimate shear stress at the interface and the concrete strength (f_c) is calculated as function of the ratio $(\rho f_y + \sigma_n)/f_c$, that has its square root multiplied by a constant in the equation. For the use of this design expression, any consistent system of units, such as Imperial Units or the International System of Units (SI), can be used.

Mattock (1981) studied the behaviour of concrete-to-concrete interfaces under cyclic loading, and concluded that a factor of 0.8 should be applied to the shear strength calculated for specimens under monotonic loading. If debonding of the interface between concrete layers occurs, the factor adopted should be of 0.6. The shear transfer mechanism for cracked specimens was found to be the same for specimens under monotonic and cyclic loading.

The concrete strength was also explicitly included in the design expression proposed by Walraven, Frénay and Pruijssers (1987). Their non-linear expression was proposed based on an experimental study they conducted with push-off specimens. The expression consists of the multiplication of a constant to the clamping stress elevated to the power of another constant, being both of these constants functions of f_c. Their publication inspired Mattock to, in 1988, propose a modification to his design expression so it would also acknowledge the concrete strength explicitly. In this modified expression, the constant term (A) is replaced by a function of f_c.

Mau and Hsu (1988) proposed a shear transfer theory from investigations conducted on shear transfer across initially uncracked planes. The shear transfer theory is based on a truss model, that considers the crushing of concrete struts as the main failure mechanism. The design expression proposed by these authors is based on semi-empirical experiments, and it has the same form of the one proposed by Loov in 1978, but instead of taking the square root of the ratio, it is elevated to the power of a parameter whose value was experimentally calibrated. For initially uncracked interfaces, this parameter was calibrated as 0.5, so the expression became of identical shape to the one proposed by Loov.

Lin and Chen (1989) proposed a similar design expression to the shear-friction expression, proposed by Birkeland and Birkeland in 1966, that was the clamping stress multiplied by a coefficient of friction. In the new expression, which was based on experiments conduct with push-off specimens, an equivalent coefficient of friction multiplies the sum of the clamping stress to the applied normal stress at the interface. The equivalent coefficient of friction was proposed as a function of the concrete strength,

the clamping stress and the normal stress applied at the interface. An upper bound limit was proposed for the ultimate shear stress.

Randl (1997) proposed a design expression that explicitly considers the contribution of three shear transfer mechanisms: cohesion, friction and dowel action. Cohesion is associated to the interlocking between aggregates; friction is associated to the surface roughness, to the normal stress acting at the contact surface and to the relative slip between concrete layers; and dowel action is associated to the resistance of the steel reinforcement that crosses the interface. Cohesion and friction are related to the Coulomb shear friction hypothesis. The combination of these three mechanisms can be written as Equation [1].

$$[1]\ \tau = \tau_c + \tau_{sf} + \tau_r$$

In which:

- τ is the total shear stress at the contact surface between the two concrete layers;
- τ_c is the cohesion component of the shear stress;
- $\tau_{sf} = \mu * \sigma_n$ is the shear-friction component of the shear stress;
- $\tau_r = \alpha * \rho * \sqrt{f_c * f_y}$ is the component of the shear stress related to dowel action at the reinforcement bars crossing the interface;
- and α is a coefficient to consider the flexural resistance of the reinforcement bars.

Zilch and Reinecke (2000) (6) proposed, in agreement with Randl that there is a combination of three load carrying mechanisms involved in shear load transfer, and studied the influence of the slip between concrete layers on each one of these mechanisms. The first of those mechanisms is cohesion or adhesion, that occurs due to the chemical bond connections between the particles of both concrete layers, with roughness and concrete strength being influencing factors. This is the first mechanism to be developed and also main mechanism for structures subject to situations in which the relative slip between concrete layers is small, such as when the load acting on the structure is low. The failure mechanism related to adhesion is debonding, that then leads to the shear stresses being transferred by mechanical interlocking. The second mechanism is shear-friction, that occurs when there is compression acting at the interface. The last mechanism is dowel action, that is related to the shear stresses due to slippage acting on the reinforcement that crosses the contact surface. This mechanism's influence increases as the relative slip between concrete layers increases. As yielding occurs at the reinforcement bars, due to the tension created by the slip, they

induce compression at the interface, leading to transfer of shear load by friction. The evolution of each component with the variation of the relative slip between layers, according to the authors, is presented in Figure 2-2.

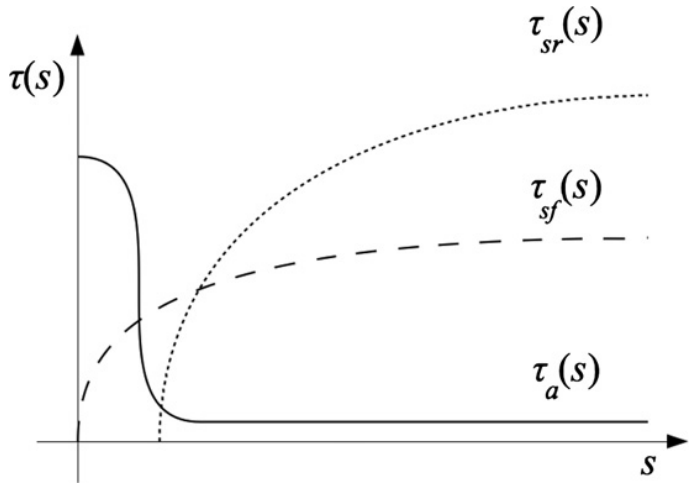

Figure 2-2 Shear stresses associated to load transfer mechanisms as functions of the relative slip between layers, as proposed by Zilch and Reinecke (6)

Mattock and Patnaik proposed modifications to their equations after additional studies, but the format of the expressions and parameters considered (clamping stress and normal stress at the interface plane) did not change significantly.

Kahn and Mitchell (2002) studied the application of shear-friction provisions to high strength concretes and proposed an expression that consists of the sum of concrete strength and clamping stress, both multiplied by different constants.

Gohnert (2003) studied the interface between precast ribs and concrete *cast-in-situ*. He concluded that the ultimate shear stress presents a better correlation with the surface roughness, represented by a texture parameter, than with the concrete compressive strength. Additionally, he stated that the surface roughness should be really measured, instead of specified only by description of the finishing procedure or equipment employed to prepare the surface.

Mansur, Vinayagam and Tan (2008) evaluated some of the design expressions commented above. The conclusions drawn from these evaluations were that the design expressions proposed by Walraven et al., by Mau and Hsu and by Loov and Patnaik result in unsafe predictions of the shear strength at the interface. A new formulation was proposed based on the design expression proposed by Mau and Hsu and calibrated by a series of experimental tests, with a concrete strength ranging from 18 MPa to 100 MPa. However, the new proposed expression was considered unsafe for low values of normalized clamping stresses, that lead to the proposition of a trilinear formulation, so the expression used to calculate the ultimate shear strength should change according to

the interval in which the normalized clamping force fits. The first two equations composing the trilinear formulation are functions of the clamping stress and the concrete compressive strength. The third equation is a constant value.

Santos and Júlio (2009) have developed an experimental study, assessing different curing conditions for the performance of the tests. The authors state that the coefficients of cohesion and friction should be calculated as functions of a texture parameter, the Mean Bally Depth of the primary profile of the surface. They also propose the use of partial safety factors for the coefficients of cohesion and friction. Two design expressions are suggested, separately for the cases in which there is no reinforcement crossing the interface and for the case in which this reinforcement is provided. The latter of these expressions is a function of a friction coefficient, clamping stress and normal stress at the interface. Finally, they propose that the shear resistance portion due to cohesion be disregarded under fatigue or dynamic loads.

Palieraki, Vintzileou and Silva (2021) (7) made an evaluation of publications from some of the authors mentioned above, in order to summarize the parameters adopted in previous research and the range of their values. Additionally, an assessment of efficiency of some proposed design equations was made. In accordance with what was previously presented, it was identified that the main parameters affecting the shear strength of concrete-to-concrete interfaces are: roughness of the interface; reinforcement ratio; magnitude of the shear slip; concrete strength; magnitude of the externally applied normal stress; type of loading and yield strength, anchorage length and diameter of the reinforcement bars. However, the latter two parameters are not usually considered in studies on the topic. A limitation was identified concerning the influence of the anchorage length, as there is a limited distance from the interface in which the steel and surrounding concrete are mobilized. Meanwhile, for small anchorage lengths there may be no mobilization occurrence, and the tensile stresses in the reinforcement may become smaller than the yield stress, leading to a reduction on the contribution of friction. An issue identified was concerning the proposal of design equations based on experimental results is the fact that the interrelation of parameters, that is of considerable complexity, can lead to misinterpretations of the results.

The authors summarized that most of the research made on the topic considers only normal strength (of strength ranging from 15 MPa to 55 MPa) and normal weight concrete. Also, most of the studied specimens had interface areas smaller than 1000 cm^2, with the width being mostly between 10 and 15 cm and the length having mostly from 25 to 50 cm. In the majority of the studies made, the steel reinforcement was composed of bars with diameters ranging from 7 mm to 13 mm, with yield strength of

around 450 MPa, and resulting in a reinforcement ratio between 0.05% and 0.55%. After evaluating previous research made, it is stated that the shear behaviour of concrete interfaces under the action of cyclic loads needs further investigation, as the influence of the parameters of roughness of the interface and of aggregate size plays a crucial role.

On the topic of cyclic actions, Palieraki et al. (2020) (8) developed a study in which a design model was proposed for structures under seismic loading condition. In the study, the effect of friction and dowel action are taken into consideration, while the effect of adhesive bond is neglected due to its mobilization being associated to slip values smaller than the typical ones that occur for seismic conditions. It is stated that the cyclic loading conditions cause force response degradation, with a decrease of resistance occurring in each cycle, a phenomenon that is not yet considered in any design codes or guidelines. The shear slip associated to the maximum resistance also changes with respect the same structures under monotonic loading conditions. The multiplication of design shear equations by a coefficient that accounts for this degradation is then proposed. The magnitude of the resistance reduction depends on roughness of the interface, as smooth interfaces have undergone smaller degradation than rough interfaces and have been proven to be less dependent on the compressive strength of concrete.

Other topics that are not considered by design codes are differential shrinkage and differential stiffness of the two concrete layers. Differential shrinkage is created by curing conditions, while differential stiffness is the product of the mismatch between the Young's modulus of both concrete layers. Santos and Júlio (2011) (9) have studied these topics. It was observed that the bond strength, and with it the ultimate stresses at the interface, increased as the difference of ages between the concrete layers increased, therefore, as the differential shrinkage increased. Additionally, it was observed that the increase in differential stiffness led to an increase in number of cohesive failures, which are failure modes with occurrence of concrete crushing, in replacement of the occurrence of adhesive failures, in which debonding occurs.

The shear displacement along the interface has also not been explored by many authors as an equation parameter to obtain the shear stress. Yang (2016) (10) has proposed comments on the topic. It is stated that the slip along the interface begins with the occurrence of shear cracks in it, that lead to immediate failure in non-reinforced interfaces and to stress flow phenomenon in reinforced ones. That is to say that in reinforced concrete interfaces the relative slip increases at a large rate after the peak stress is reached, with a rapid decrease of shear stresses after the peak, followed by the maintenance of an almost constant value. The shear stress associated to cracking

increases with the increase of applied compressive normal stress, as it reduces the principle tensile stresses along the shear plane.

Most of the experiments performed to study concrete-to-concrete interfaces have used push-off tests configurations. Nevertheless, the new EAD 332347–00-0601-v01 (13) (European Assessment Document) that assess the seismic behaviour of shear interface, introduced a new type of specimen that allows the application of cyclic load. That specimen has a relatively big size with respect to typical specimens used to assess the shear behaviour, but at same time as shown by Cattaneo et al. (2021) (11) that test set-up is the most reliable, considering studies concerning monotonic and reversal cyclic loading. In that study, three test set-ups, including the push-off one, were numerically analysed.

The analysed set-ups are presented in Figure 2-3, and the chosen configuration was Type 2, with the addition of orthogonal constraints to prevent the rotation of the specimen and resulting the perturbative effects due to bending moments. In the figure, the existing concrete layer, with lower mechanical properties, is represented in green colour, while the added concrete layer is represented in grey. The Type 2 configuration has presented the advantages of allowing the application of reversal loading, having the applied load at the same level of the interface and having reduced bending effects affecting the results. However, it has the disadvantage of presenting eccentricity between the applied load and the reaction.

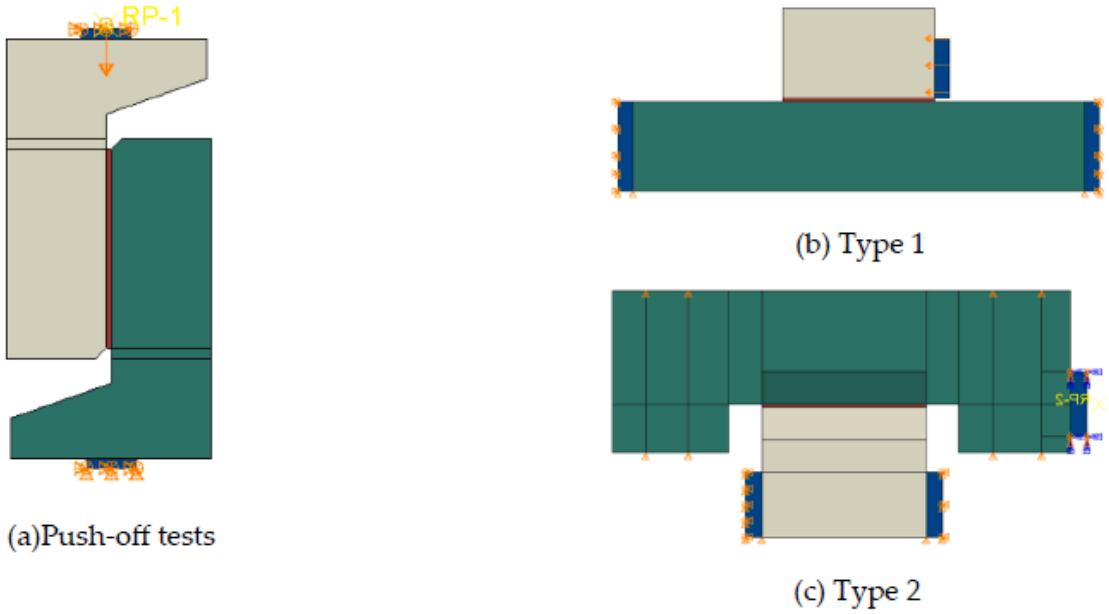

Figure 2-3 Evaluated test set-ups

After the numerical analysis was performed, an experimental campaign was conducted at Politecnico di Milano, adopting the chosen configuration with its two different boundary conditions (with and without orthogonal restraints). Specimens of considerable size were adopted so the experimental results would be significant for real applications. The concrete designed for the experiments was in accordance with the prescription of EOTA-TR048 (12), and the layers were cast three months apart. All specimens were treated in the same way, so they would have same roughness and curing conditions. Monotonic and cyclic loading conditions were evaluated in the campaign, both with displacement-controlled tests. The test protocol chosen was in accordance with the guideline EAD 332347–00-0601-v01 (13).

As a final comment, it is expected that the presented literary revision could introduce the complexity of the topic of connections between concrete layers of different mechanical properties, showing that there are many possibilities of research to be done in the topic, as there are many parameters involved in it, that interact with each other and can lead to different influences on the shear resistance depending on the range. Furthermore, as the topic is related to a wide range of applications, studies can also be developed focusing on one of those applications.

3. Chapter Three: Description of the model

For the development of the work presented in this document, the commercial software SIMULIA Abaqus was used to perform static Finite Elements Analysis. This chapter will be dedicated to the description of the initial model developed in it. Several modifications were made to this initial model so the desired analysis could be achieved. These modifications will be presented in the following chapters as the goals related to each modification are commented on.

3.1. Geometry

Considering the conclusions presented by Cattaneo, S.; Zorzato, G.; Bonati, A. (2021) (11) and the availability of experimental results, the shape and dimensions chosen for the initial geometry of the model were as presented in Figure 3-1 and Figure 3-2.

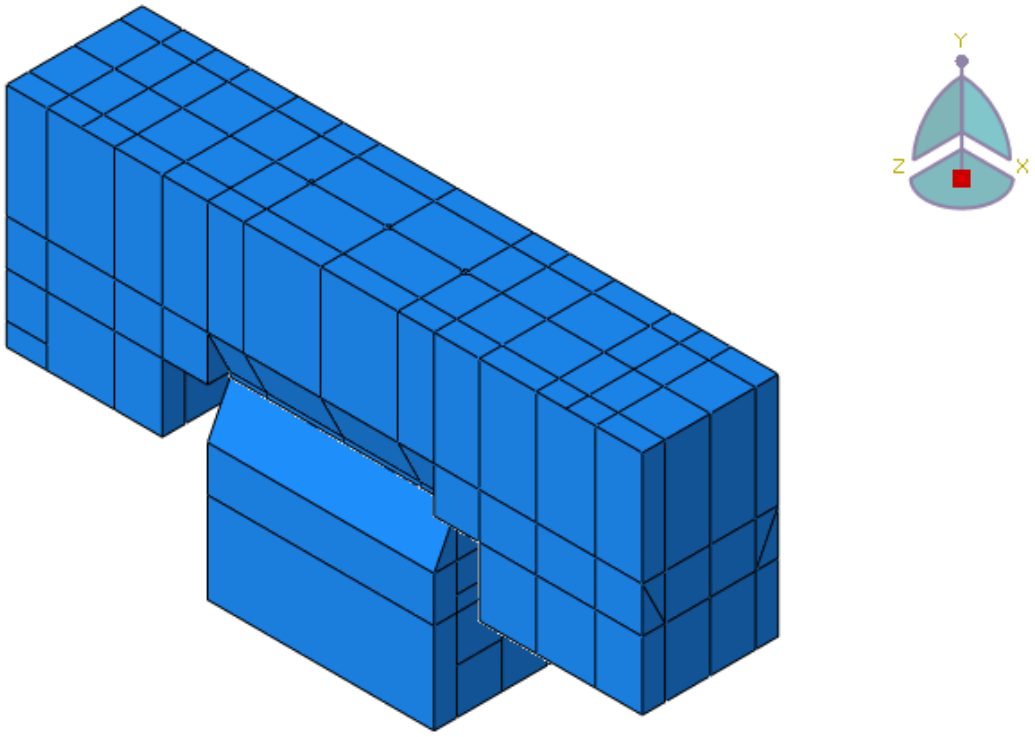

Figure 3-1 Initial geometry of the model

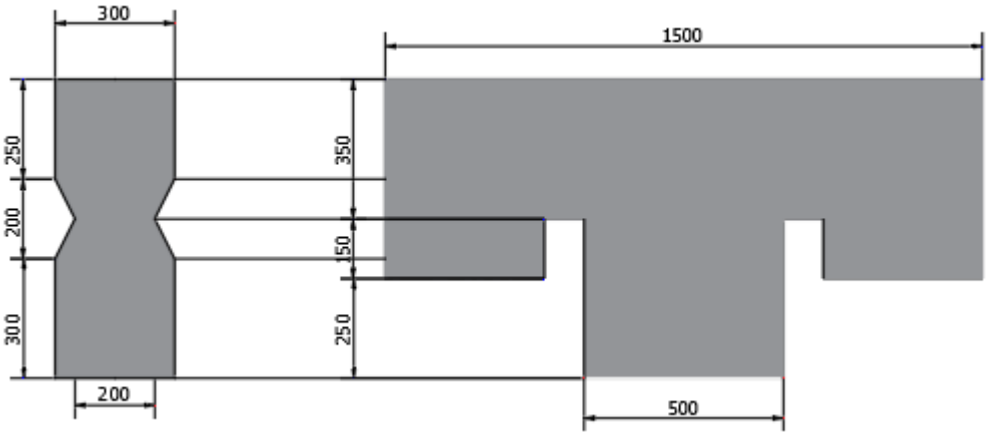

Figure 3-2 Dimensions of the initial geometry [mm]

The proposed rebar setting for the specimen is composed of rebar of diameters 8mm and 12mm, modelled as 1D elements. Besides that, for the connection between both concrete parts three anchors of diameter equal to 14 mm modelled as 3D elements are used. The complete steel setting is presented in Figure 3-3, and details of ϕ8 and ϕ12 rebars are presented in Figure 3-4 and Figure 3-5.

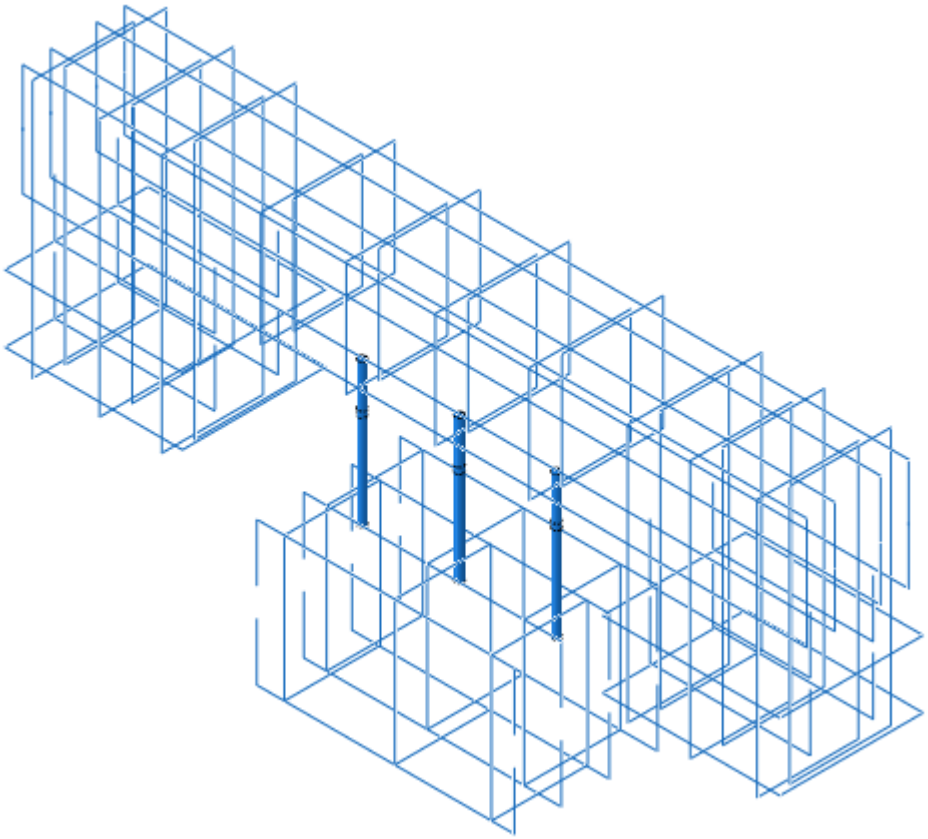

Figure 3-3 Initial steel setting

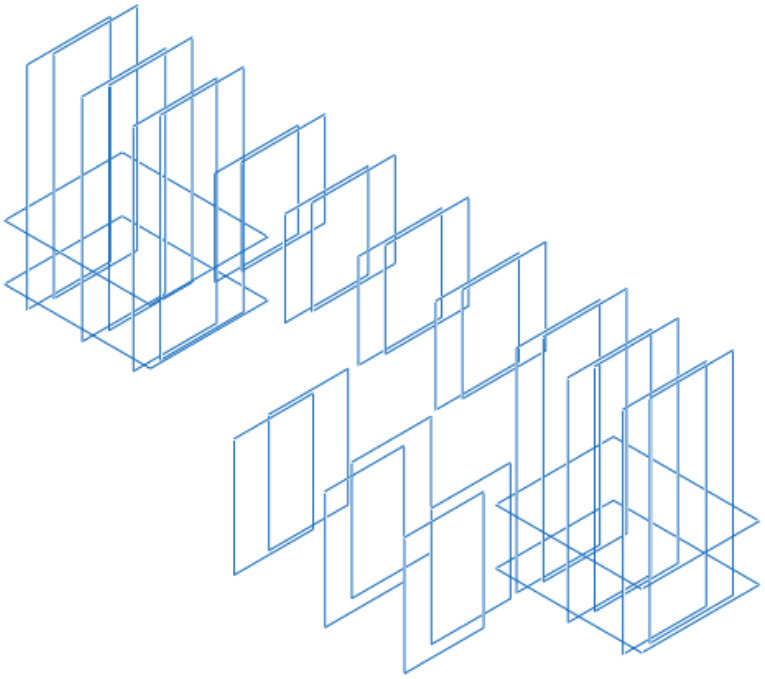

Figure 3-4 Rebar setting - ϕ8mm bars

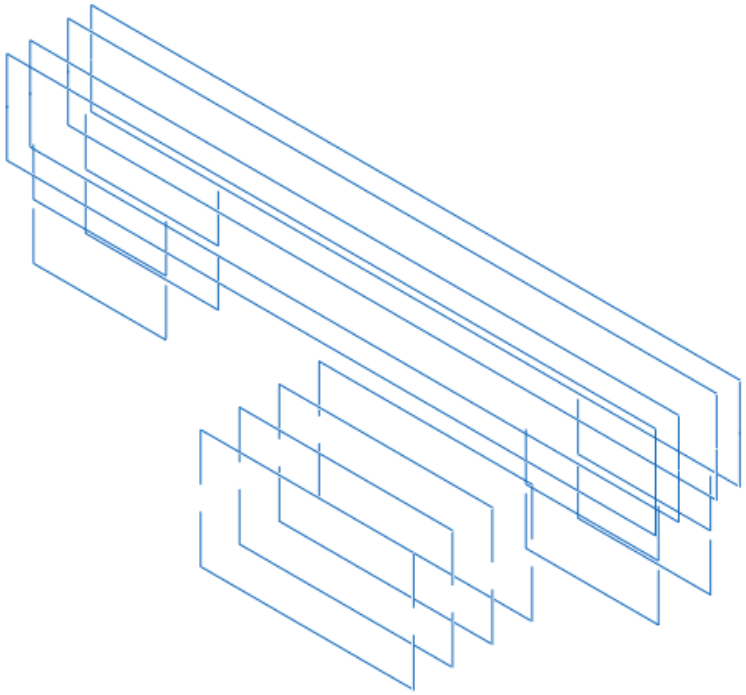

Figure 3-5 Rebar setting - ϕ12mm bars

To allow for a better numerical analysis, the interface between the concrete parts was modelled separately, with a thickness of 10mm.

Orthogonal restraints were used in the experimental tests according to the test procedure defined in EAD 332347–00-0601-v01, with the objective of avoiding rotation of the top concrete part, thus providing a shear stress with limited bending interaction of

the pieces [as explained in (11)]. To introduce those restraints in the model, constraints were defined, avoiding additions in the geometry. The constraints introduced in the model are better explained in Section 3.4.

3.2. Constitutive Model

3.2.1. Concrete Damaged Plasticity model

All analysis presented have been done using the Concrete Damaged Plasticity (CDP) model offered by Abaqus, which represents the inelastic behaviour of concrete related to the fracturing process by using concepts of isotropic damaged elasticity in combination with isotropic tensile and compressive plasticity. It requires that the elastic behaviour of the material be isotropic and linear.

The CDP model is a continuum, plasticity-based damage model, that uses a fictitious crack model based on fracture energy, better capturing the nonlinear behaviour of concrete. In it, tensile cracking and compressive crushing of the concrete are both considered as the main possible failure mechanisms, and accordingly scalar damage variables can be introduced separately for tension and compression. Those damage parameters dictate the degradation of the elastic stiffness of the material, as will be better illustrated later in this section by Equation 2 and Figure 3-7. They can assume values from zero (representing absence of damage) to one (representing total loss of strength).

The CDP model can be used in conjunction with a viscoplastic regularization, by allowing the introduction of a viscoplasticity parameter (μ), which provides additional ductility for the modelled structure. This regularization has a considerable influence on the convergence of the analysis, as it is able to diminish the impact of localized cracking and strain, which can create convergence problems in the softening regime, by allowing stresses to be outside of the yield surface. The viscosity parameter μ must be small compared to the characteristic time increment so it does not compromise the results. The mentioned viscoplastic regularization follows a generalization of the Duvaut-Lions approach.

The model's yield function, that is the one defined by Lubliner et. al. (1989) with the modifications proposed by Lee and Fenves (1998), is controlled by two hardening variables, one associated with tension loading and the other one associated with compression loading. It can be represented as in Figure 3-6. The model considers the effective stress space, being the effective stress ($\bar{\sigma}$) defined as in Equation 2:[2

$$[2] \qquad \bar{\sigma} = \frac{\sigma}{1-d} = E_0 * \left(\varepsilon - \tilde{\varepsilon}_{pl}\right)$$

In which:

- σ denotes the total stress;
- d denotes damage parameter;
- E_0 denotes initial modulus of elasticity;
- ε denotes total strain, with $\varepsilon = \varepsilon_{el} + \varepsilon_{pl}$;
- $\tilde{\varepsilon}_{pl}$ denotes equivalent plastic strain, which is the hardening variable, that can be associated with tension or compression loads.

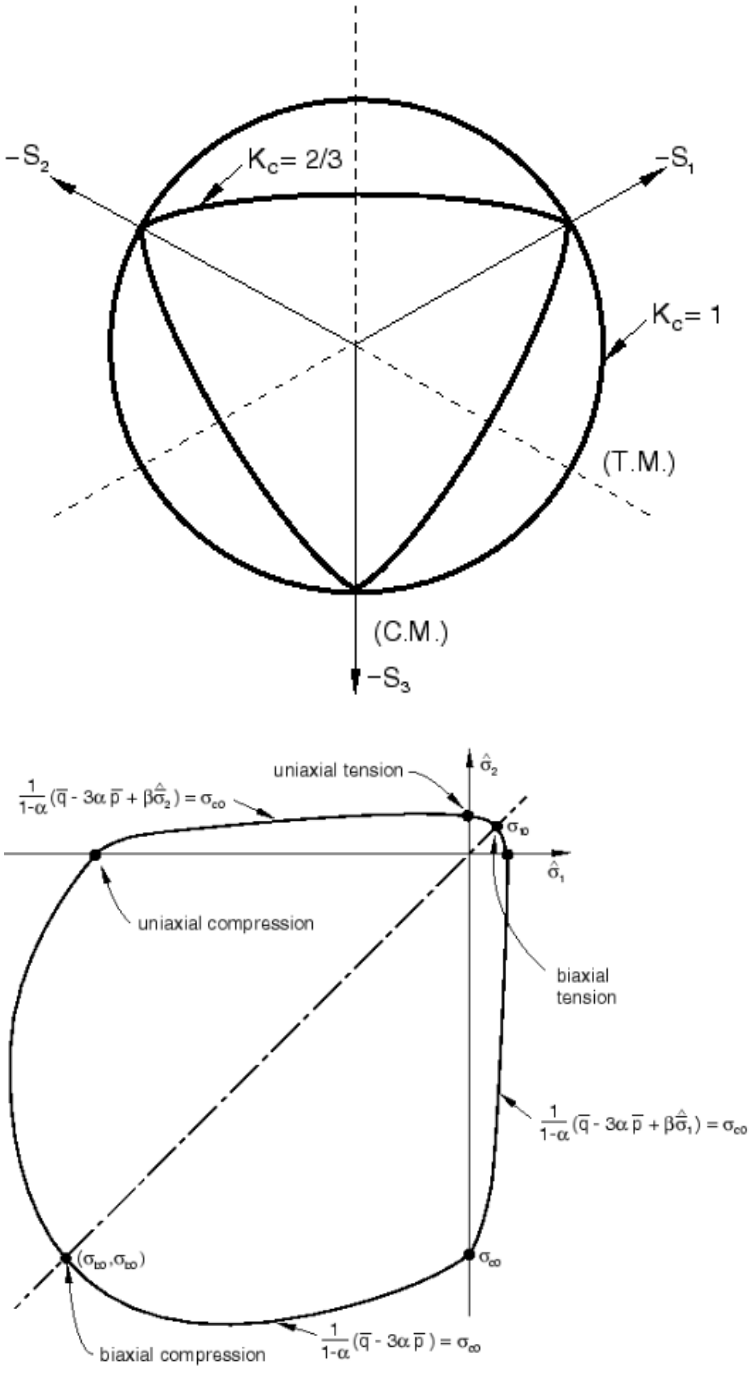

Figure 3-6 Yield surfaces respectively in the deviatoric plane and for plane stress conditions

A non-associated potential plastic flow is assumed by the CDP model. The Drucker-Prager hyperbolic function is adopted to define the flow potential G. Since this definition ensures a continuous and smooth flow potential, it is guaranteed that the flow direction is always uniquely defined. The default flow potential eccentricity (ϵ), that is a parameter for the curvature of the flow potential that dictates the variability of the dilation angle over a range of confining pressures, is $\epsilon = 0.1$. The flow rule can be represented by Equation *3*, in which $\dot{\lambda}$ is a nonnegative plastic multiplier.

$$[3] \qquad \dot{\varepsilon}_{pl} = \dot{\lambda} \frac{\delta G(\bar{\sigma})}{\delta \bar{\sigma}}$$

The stress-strain relations considered for the model are represented in Figure 3-7 for uniaxial loading. As can be seen in the figure, the response is characterized by a linear elastic stress-strain relationship until a limit value of stress, σ_{t0} or σ_{c0}, is reached. Under uniaxial tension, that limit value represents the failure stress, while under uniaxial compression it represents the initial yield stress, that is then followed by the ultimate stress σ_{cu}, reached after a hardening branch. After those values are reached, there is a softening branch in which strain localization is induced in the structure.

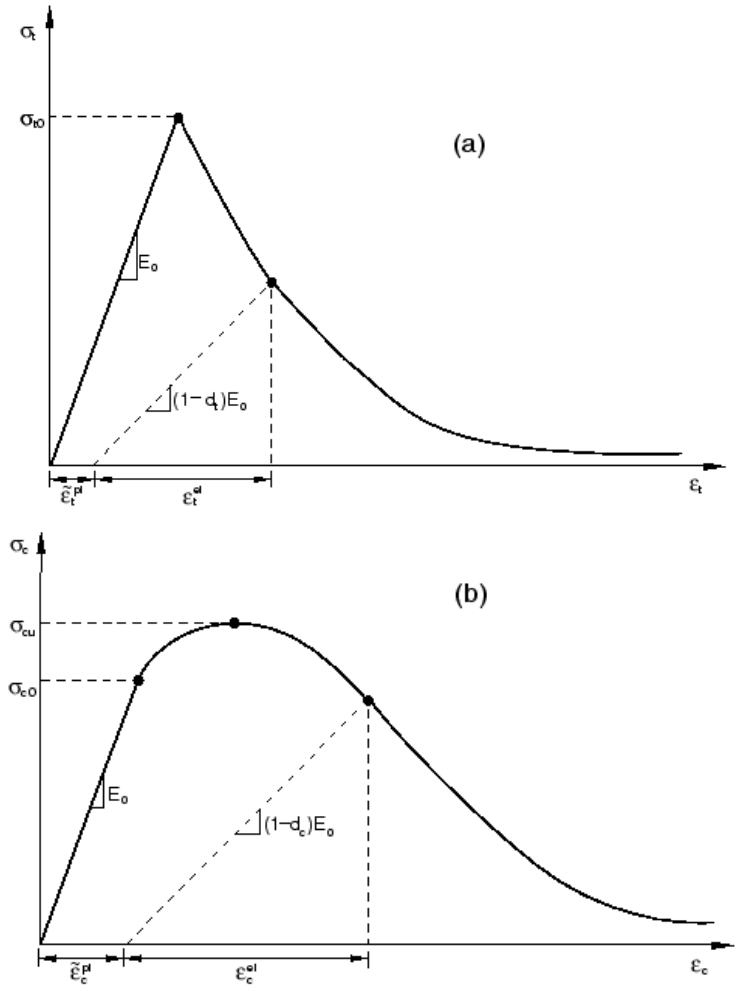

Figure 3-7 Concrete's response to uniaxial loading in (a) tension or (b) compression

Compressive damage curves, given as values of the damage variable d_c *versus* the inelastic strain values $\tilde{\varepsilon}_{c,in}$, must be introduced as input in the Abaqus model. The plastic strain values are then automatically obtained by Abaqus. If they are found to be negative and/or decreasing with increasing inelastic strain an error messaged is issued. Similarly, the tensile damage curves must be introduced, but for them that was done in terms of the damage variable d_t *versus* the cracking displacement w.

The stress-crack opening displacement relationship proposed by Hordijk (1991), presented in Equations *4*, *5* and *6*, is used as reference for the analysis presented in this report.

$$[4] \qquad \frac{\sigma}{f_t'} = f(w) - \left(\frac{w}{w_c}\right) * f(w_c)$$

$$[5] \qquad f(w) = \left(1 + \left(\frac{c_1 * w}{w_c}\right)^3\right) exp\left(-\frac{c_2 * w}{w_c}\right)$$

$$[6] \qquad w_c = 5.14 * \frac{G_f}{f_t'}$$

In which:

- f_t' is the concrete uniaxial tensile strength;
- c_1 and c_2 are material constants, that can be adopted respectively as equal to 3 and 6.93 for normal concrete, as determined by tensile tests on concrete specimen;
- G_f denotes the fracture energy of the concrete, which graphically is equal to the area under the tensile stress-crack displacement curve, which can be calculated as $G_f = 73 * f_{cm}^{0.18}$, in accordance to the CEB-FIP Model Code of 2010 (14);
- w and w_c denote crack opening displacements and its critical value, that is related to the complete loss of tensile stress.

3.2.2. Initially adopted parameters

For the elastic branch, it was adopted $E_c = 31\ GPa$ as elastic modulus for the old concrete, of class C25/30, and $E_c = 32\ GPa$ as elastic modulus of the added concrete, of class C28/35, in accordance with the experiments whose results are used. The Poisson's ratio adopted had a value of 0.18 for both materials. For the modelled interface layer, a lower value was chosen for the modulus of elasticity: $E_c = 1\ GPa$, as adopted in previous analysis (11). A typical density value of 2300 kg/m^3 was chosen for all of those materials.

For the input plasticity parameters of the analysis, the typical values presented on Table 3-1 were initially adopted. In the presented table, f_{b0}/f_{c0} represents the ratio between strengths in biaxial compression and in uniaxial compression, K represents the ratio between deviatoric stresses in uniaxial tension and compression (in absolute values) and μ represents the viscosity, as commented previously.

Table 3-1 Initial plasticity inputs introduced for CDP model

Dilation Angle	Eccentricity	f_{b0}/f_{c0}	K	Viscosity Parameter
35	0.1	1.16	0.667	0.007985

The values initially used as input in the model to represent the compressive and tensile damage curves are presented in Table 3-2 and Table 3-3. The maximum stress and critical crack opening displacement values were determined according to the previously presented calculations (Equations [4] to [6]). For the tensile damage curve, the evolution of the stresses as the displacement increases is described by Equation [7], in which $w_{ch} = G_f/f_t'$, suggested by Focacci, F. et al (2020). From that evolution, the damage parameters were obtained. For the compressive damage curve, the parameters were extracted from the experimental data.

[7] $$\sigma_m(w) = f_t * \left[\left(1 + 0.199 * \left(\frac{w}{w_{ch}}\right)^3\right) * e^{-1.35*\frac{w}{w_{ch}}} - 0.00533 * \frac{w}{w_{ch}}\right]$$

Table 3-2 Initially adopted tensile damage curve

C25/30		
Gf (N/m)	ft (MPa)	Wc (mm)
90	1.6	0.289
W (mm)	б (MPa)	d
0.000	1.600	0.000
0.014	1.133	0.272
0.029	0.817	0.469
0.043	0.611	0.598
0.058	0.478	0.681
0.072	0.391	0.735
0.087	0.333	0.772
0.101	0.290	0.799
0.116	0.255	0.820
0.130	0.225	0.839
0.145	0.197	0.857
0.159	0.170	0.874
0.173	0.145	0.890
0.188	0.120	0.905
0.202	0.098	0.919

C28/35		
Gf (N/m)	ft (MPa)	Wc (mm)
100	1.8	0.286
W (mm)	б (MPa)	d
0.000	1.800	0.000
0.014	1.275	0.272
0.029	0.920	0.469
0.043	0.687	0.598
0.057	0.538	0.681
0.071	0.440	0.735
0.086	0.374	0.772
0.100	0.326	0.799
0.114	0.287	0.820
0.129	0.253	0.839
0.143	0.222	0.857
0.157	0.192	0.874
0.171	0.163	0.890
0.186	0.135	0.905
0.200	0.110	0.919

0.217	0.077	0.932	0.214	0.086	0.932
0.231	0.058	0.944	0.228	0.065	0.944
0.246	0.041	0.955	0.243	0.046	0.955
0.260	0.025	0.964	0.257	0.028	0.964
0.275	0.012	0.973	0.271	0.013	0.973
0.289	0.000	0.980	0.286	0.000	0.980

Table 3-3 Initially adopted compressive damage curve

C25/30			C28/35		
ε	б (MPa)	d	ε	б (MPa)	d
0.000	12.750	0.000	0.000	14.280	0.000
0.000	16.000	0.000	0.000	17.920	0.000
0.000	18.750	0.000	0.000	21.000	0.000
0.000	21.000	0.000	0.000	23.520	0.000
0.000	22.750	0.000	0.000	25.480	0.000
0.000	24.000	0.000	0.000	26.880	0.000
0.001	24.750	0.000	0.001	27.720	0.000
0.001	25.000	0.000	0.001	28.000	0.000
0.001	24.764	0.009	0.001	27.736	0.009
0.001	24.123	0.035	0.001	27.018	0.035
0.001	23.185	0.073	0.001	25.968	0.073
0.001	22.059	0.118	0.001	24.706	0.118
0.001	20.833	0.167	0.001	23.333	0.167
0.001	19.578	0.217	0.001	21.928	0.217
0.002	18.342	0.266	0.002	20.543	0.266
0.002	17.157	0.314	0.002	19.216	0.314
0.002	16.040	0.358	0.002	17.965	0.358
0.002	15.000	0.400	0.002	16.800	0.400
0.002	14.040	0.438	0.002	15.725	0.438
0.002	13.158	0.474	0.002	14.737	0.474
0.002	12.350	0.506	0.002	13.832	0.506
0.002	11.612	0.536	0.002	13.005	0.536
0.002	10.938	0.563	0.003	12.250	0.563
0.003	10.321	0.587	0.003	11.560	0.587
0.003	9.757	0.610	0.003	10.928	0.610
0.003	9.241	0.630	0.003	10.350	0.630
0.003	8.768	0.649	0.003	9.820	0.649
0.003	8.333	0.667	0.003	9.333	0.667
0.003	7.933	0.683	0.003	8.885	0.683
0.003	7.565	0.697	0.003	8.473	0.697
0.003	7.224	0.711	0.003	8.091	0.711
0.003	6.910	0.724	0.003	7.739	0.724
0.003	6.618	0.735	0.004	7.412	0.735
0.003	6.347	0.746	0.004	7.108	0.746

0.004	6.094	0.756	0.004	6.826	0.756
0.004	5.859	0.766	0.004	6.563	0.766
0.004	5.640	0.774	0.004	6.317	0.774
0.004	5.435	0.783	0.004	6.087	0.783
0.004	5.243	0.790	0.004	5.872	0.790
0.004	5.062	0.798	0.004	5.670	0.798
0.004	4.893	0.804	0.004	5.480	0.804
0.004	4.734	0.811	0.004	5.302	0.811
0.004	4.583	0.817	0.005	5.133	0.817
0.004	4.442	0.822	0.005	4.975	0.822
0.004	4.308	0.828	0.005	4.825	0.828
0.004	4.181	0.833	0.005	4.683	0.833
0.005	4.061	0.838	0.005	4.548	0.838
0.005	3.947	0.842	0.005	4.421	0.842

For the reinforcement and anchorage bars, the steel chosen was of class B450C. It was defined as an elastic-perfectly plastic material, with elastic modulus $E_s = 210\ GPa$, Poisson's ratio equal to 0.3, yield stress of 450 MPa and zero plastic strain (as necessary to define perfect plasticity). Its density was set as 7850 kg/m^3. The concrete behaviour is considered independently of the steel bars by Abaqus, being effects associated with the steel/concrete interface modelled approximately by the introduction of tension stiffening into the concrete model.

3.3. Mesh Creation

The creation of the mesh was done using the automatic tools provided by Abaqus, adding partitions to the model when necessary to ensure a good quality of the mesh. The result is presented in Figure 3-8.

The element type selected by Abaqus for the 3D modelled parts, namely the top and bottom concrete pieces, the interface layer and the anchors, is linear hexahedral elements of type C3D8. The size ranges from approximately 1.5 mm in regions that require more refinement, such as near the anchors, to around 20 mm in regions that allow a rougher mesh, such as the edges of concrete parts that are interfaces with other parts.

For the 1D modelled parts, which are the reinforcement bars, linear line elements of type B31 were chosen. As these elements do not require much refinement, their meshes reach element sizes up to 50 mm.

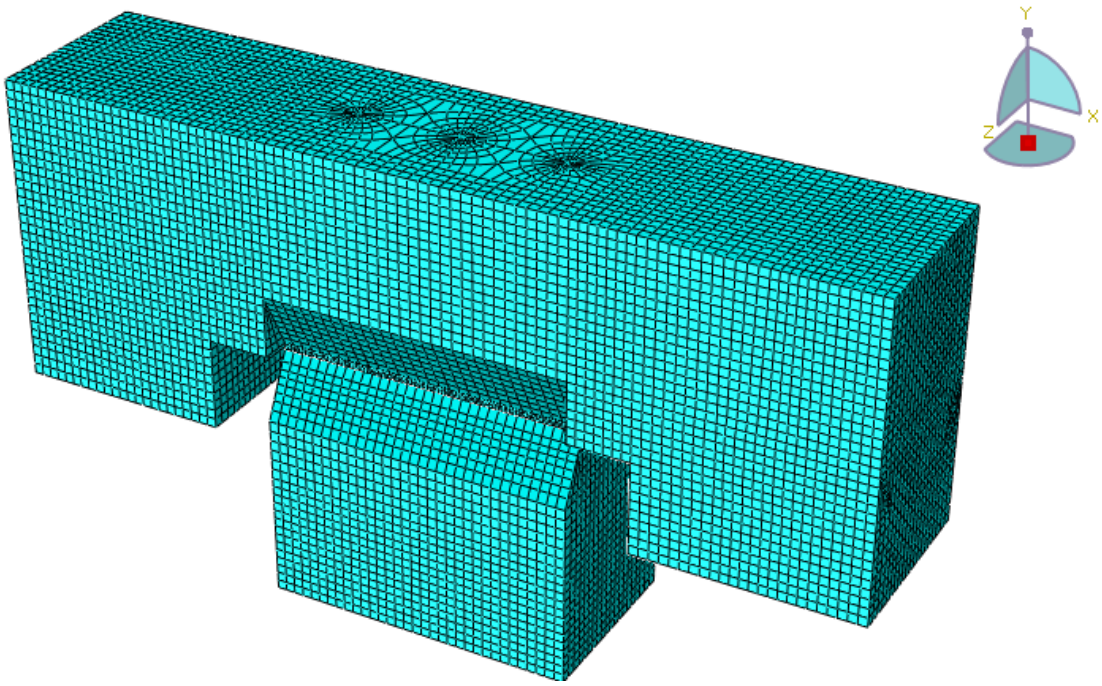

Figure 3-8 Mesh created

3.4. Constraints, Interactions and Boundary Conditions

To complete the model, constraints, interactions and boundary conditions were defined. For their definition, five reference points (RP) were picked, as presented in Figure 3-9.

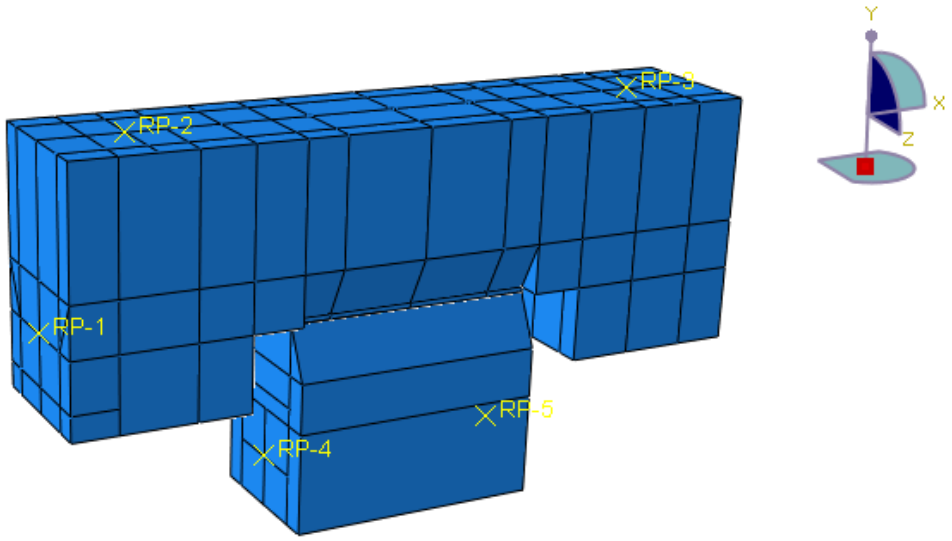

Figure 3-9 Location of reference points

Nine constraints were defined in the model. Five of them are constraints of type Kinematic Coupling that constraint all degrees of freedom of the surfaces around each reference point, being each constraint related to one RP, using the reference points as control points. These constraints are useful for the definition of boundary conditions, as will be commented afterwards in this section. The constraints related to RP-2 and RP-3

are the ones used to model the orthogonal restraints, as commented previously on Section 3.1.

Other two constraints are of type Tie, they introduce master-slave relations between the top and bottom surfaces of the interface layer (slave surfaces) and the surfaces of the top concrete piece (existing concrete) and the bottom concrete piece (added concrete) that are in contact with the interface layer (master surfaces).

Finally, the remaining two constraints define the rebar settings as embedded in the top and bottom concrete parts.

Interactions were set in the model to define the relationship between the anchors and the concrete parts. As there are three anchors and three concrete parts (top piece, interface layer and bottom piece), nine interactions were set, each relating one anchor to one concrete part. They were defined as surface-to-surface contact with finite sliding, with the anchor surfaces defined as master surfaces and the concrete's defined as slave surfaces. The tangential behaviour of the interactions was set by defining a friction coefficient of 0.8 and the normal behaviour was set by defining a pressure-overclosure of type hard contact.

Five boundary conditions were defined, each one related to one reference point and therefore, due to the constraints mentioned above, to the region around it. The first one, associated with RP-1, is used to define the applied displacement that controls the experiment. For that purpose, the first degree of freedom (U1) is associated to a value of 10 mm while a value of zero is associated with the remaining degrees of freedom. The value of U1 is then related to an amplitude from 0 to 1, discretized in steps of 0.1, that is associated with time.

The boundary conditions associated with RP-2 and RP-3 leave U1 free, in other words, they do not associate any value to U1, and the remaining degrees of freedom are associated to zero. That is to say that the top concrete part is left free to move in U1 direction, as necessary to evaluate the influence of the applied displacement in RP-1, which is the purpose of the simulation. Other degrees of freedom are restrained so they do not influence the results, that should focus on the U1 displacement, simulating the orthogonal restraints used in the experiment.

The remaining boundary conditions, associated to RP-4 and RP-5, associate all degrees of freedom to zero values. That means that the bottom concrete piece is restrained, which allows for a better evaluation of the slip produced between both pieces and the resistance created by the interaction of them, which, again, is the objective of the study.

4. Chapter Four: Validation of numerical model

The model presented in the Chapter 3 had its results compared to experimental results available from the concrete specimen whose geometry was used as reference for the model development. Specifically, the load *versus* displacement curves, which are presented in Graph 4-1 and Graph 4-2, was chosen as focus for the result comparison. From that comparison, adjustments to the model's input values were made until the numerical analysis presented results with enough compatibility with the experimental ones. The geometry of the model did not suffer any adjustment, as it was considered representative of the specimen to a satisfactory level.

This chapter is dedicated to presenting the adjustments attempted in the model and the knowledge obtained concerning the impact of the studied input variables in the load *versus* displacement curve of the model. Each sub-section of this chapter will be dedicated to the study of how one input variable influences the results, and a final sub-section will report some additional considerations extracted from the studies.

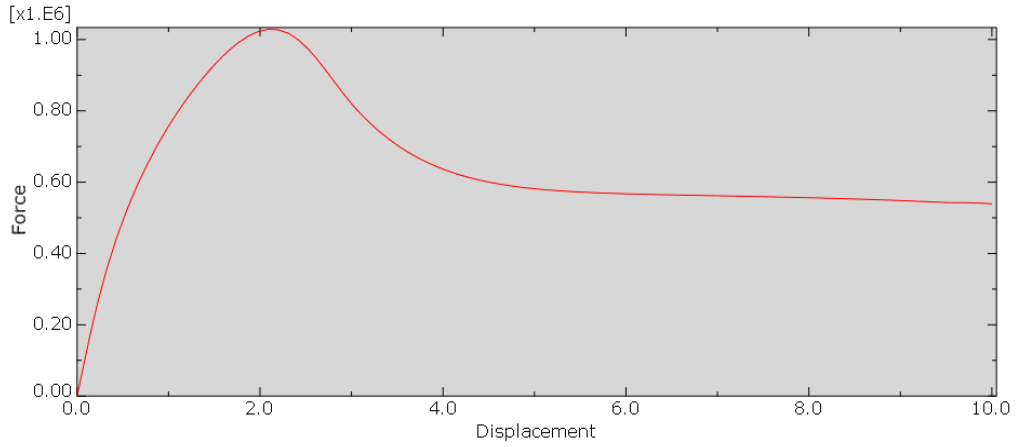

Graph 4-1 Load (N) versus slip (mm) curve obtained from the initial input values

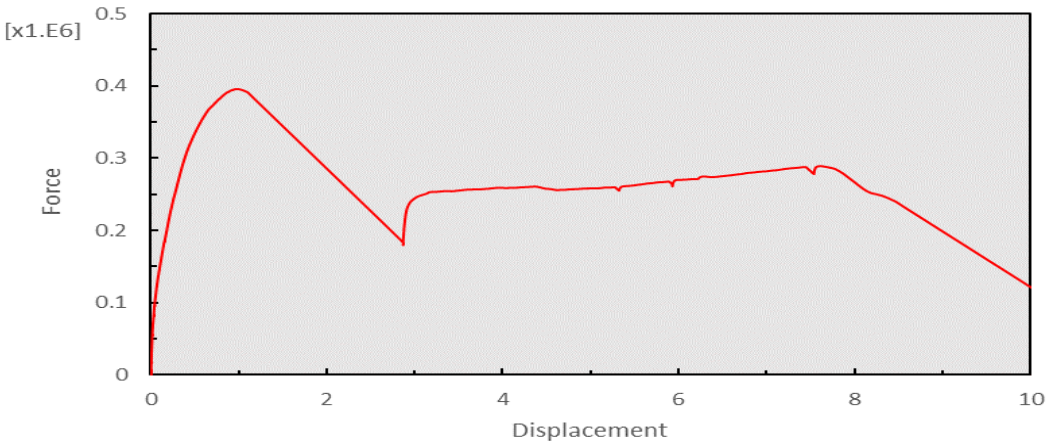

Graph 4-2 Experimental results

The parameters associated with concrete's strength, concrete uniaxial tensile strength (f_t') and fracture energy (G_f), are responsible for the definition of the tensile damage curve, and therefore their values were modified in attempts to establish a damage curve whose associated results were a better fit to the experimental ones. As the compression damage curve was considered well-adjusted to the experiment, no modifications were proposed to it.

Three basic models (Models I, II and III) were created by changing those parameters between each of them. Therefore, they are differentiated among each other by their tensile damage curves. For Model I, the initial parameters were adopted, as displayed in

Table 4-1 along with the parameters adopted for the other models. The tensile damage curve for Model I was presented in Table 3-2, for Models II and III they are presented next, in Table 4-2 and Table 4-3.

For these models, the main modifications were made to the concrete uniaxial tensile strength values. Later in this chapter, additional simulations, that were made to analyse the results' sensitivity to the fracture energy values, are introduced and commented on.

Table 4-1 Parameters chosen for each proposed model

	C25/30		C28/35	
	G_f (N/m)	f_t' (MPa)	G_f (N/m)	f_t' (MPa)
Model I	90	1.6	100	1.8
Model II	90	1.8	110	2
Model III	90	1.2	100	1.4

Table 4-2 Damage tensile curve for Model II

C25/30		
Gf (N/m)	ft (MPa)	Wc (mm)
90	1.8	5.140
W (mm)	б (MPa)	d
0.000	1.800	0.000
0.013	1.275	0.272
0.026	0.920	0.469
0.039	0.687	0.598
0.051	0.538	0.681
0.064	0.440	0.735
0.077	0.374	0.772
0.090	0.326	0.799
0.103	0.287	0.820
0.116	0.253	0.839
0.129	0.222	0.857
0.141	0.192	0.874
0.154	0.163	0.890

C28/35		
Gf (N/m)	ft (MPa)	Wc (mm)
110	2	0.283
W (mm)	б (MPa)	d
0.000	2.000	0.000
0.014	1.416	0.272
0.028	1.022	0.469
0.042	0.763	0.598
0.057	0.597	0.681
0.071	0.489	0.735
0.085	0.416	0.772
0.099	0.362	0.799
0.113	0.319	0.820
0.127	0.281	0.839
0.141	0.246	0.857
0.155	0.213	0.874
0.170	0.181	0.890

0.167	0.135	0.905	0.184	0.151	0.905
0.180	0.110	0.919	0.198	0.122	0.919
0.193	0.086	0.932	0.212	0.096	0.932
0.206	0.065	0.944	0.226	0.072	0.944
0.218	0.046	0.955	0.240	0.051	0.955
0.231	0.028	0.964	0.254	0.032	0.964
0.244	0.013	0.973	0.269	0.015	0.973
0.257	0.000	0.980	0.283	0.000	0.980

Table 4-3 Damage tensile curve for Model III

C25/30			C28/35		
Gf (N/m)	**ft (MPa)**	**Wc (mm)**	**Gf (N/m)**	**ft (MPa)**	**Wc (mm)**
90	1.2	0.386	100	1.4	0.367
W (mm)	**б (MPa)**	**d**	**W (mm)**	**б (MPa)**	**d**
0.000	1.200	0.000	0.000	1.400	0.000
0.019	0.850	0.272	0.018	0.991	0.272
0.039	0.613	0.469	0.037	0.715	0.469
0.058	0.458	0.598	0.055	0.534	0.598
0.077	0.358	0.681	0.073	0.418	0.681
0.096	0.294	0.735	0.092	0.342	0.735
0.116	0.250	0.772	0.110	0.291	0.772
0.135	0.217	0.799	0.129	0.254	0.799
0.154	0.192	0.820	0.147	0.224	0.820
0.173	0.169	0.839	0.165	0.197	0.839
0.193	0.148	0.857	0.184	0.172	0.857
0.212	0.128	0.874	0.202	0.149	0.874
0.231	0.108	0.890	0.220	0.127	0.890
0.251	0.090	0.905	0.239	0.105	0.905
0.270	0.073	0.919	0.257	0.086	0.919
0.289	0.058	0.932	0.275	0.067	0.932
0.308	0.043	0.944	0.294	0.050	0.944
0.328	0.030	0.955	0.312	0.035	0.955
0.347	0.019	0.964	0.330	0.022	0.964
0.366	0.009	0.973	0.349	0.010	0.973
0.386	0.000	0.980	0.367	0.000	0.980

4.1. Viscosity Parameter (μ)

The viscosity parameter was evaluated in using the three basic models. Parameters were chosen according to the goal, which was to find reasonable input values that approximate the numerical results to the experimental ones. For the simulations whose results are presented next, the value of dilation angle adopted was 15° and the values of the remaining parameters were the same as the initial ones, presented in Chapter 3. The results of these simulations are presented in Graph 4-3, Graph 4-4 and Graph 4-5.

In the analysis performed with Model III, different viscosity parameters were introduced separately in the two concrete parts considered, while in simulations performed with Models I and II the value of the parameter was always equal in both concrete parts in each analysis.

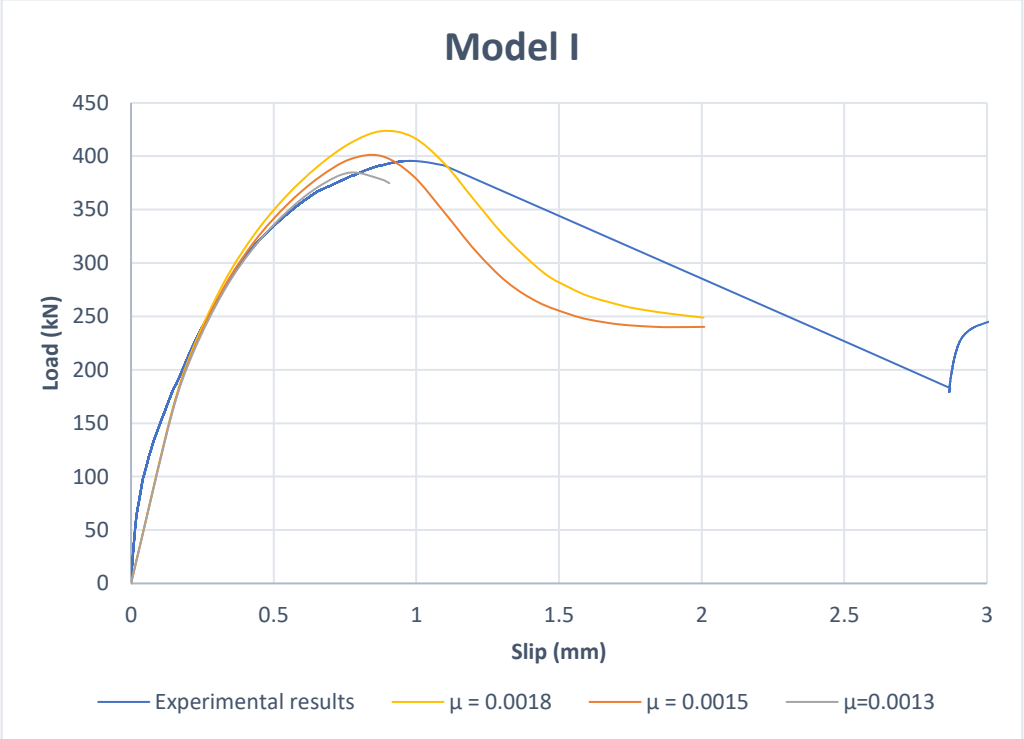

Graph 4-3 Viscosity analysis in Model I

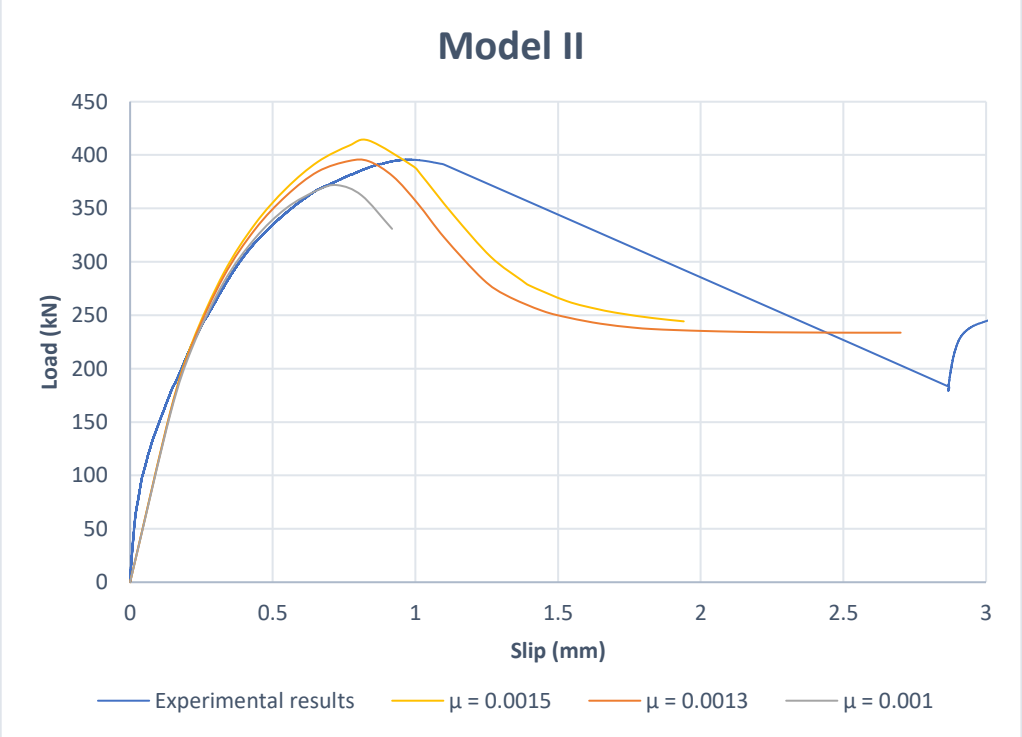

Graph 4-4 Viscosity analysis in Model II

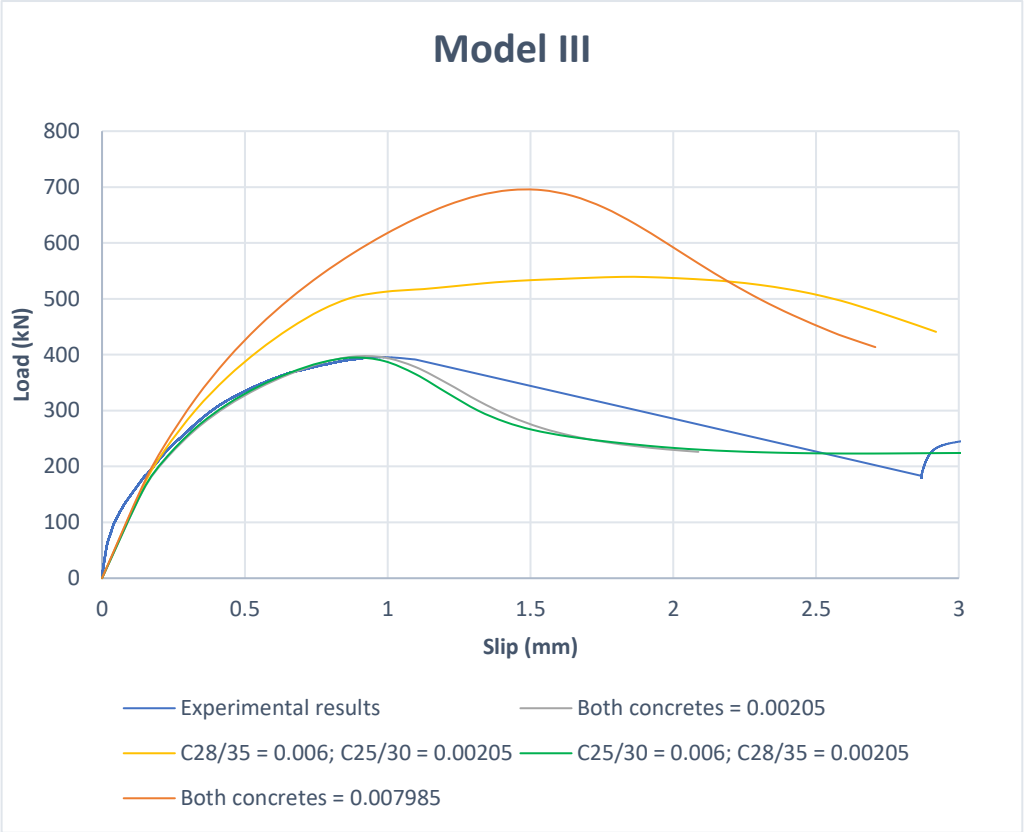

Graph 4-5 Viscosity analysis in Model III

From the presented results it is possible to observe that the viscosity parameter has a considerable influence on the value of the peak load. The parameter and the resulting peak load show, in the range of values considered, a relationship with almost linearly direct proportionality. That is to say that decreasing μ the obtained loads decrease, with the peak load following a linear trend with the viscosity variation, as can be seen in Graph 4-6.

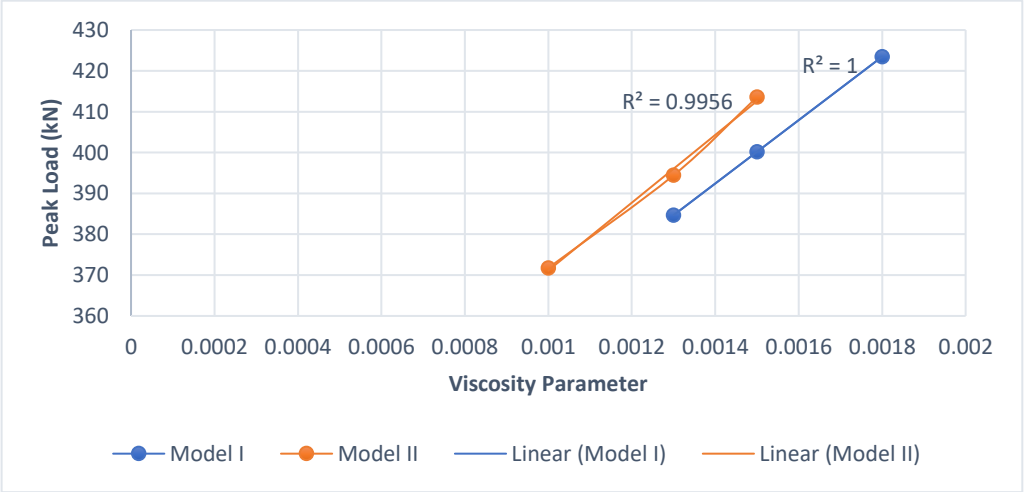

Graph 4-6 Peak Load variation according to the Viscosity Parameter

From the results of Model III, it is also possible to observe that the influence of the viscosity parameter of the concrete of lower strength (C25/30) on the peak load is very small. That can be seen by comparing the results of the simulation with both $\mu = 0.00205$ to the ones of the simulation in which $\mu = 0.00205$ only for C28/35. Even though C25/30 has a higher viscosity parameter in this second simulation, the peak load obtained is practically the same in both analyses.

In contrast, in the simulation in which $\mu = 0.00205$ for C25/30 and $\mu = 0.006$ for C28/35 (therefore higher than for C25/30) the peak load obtained is higher than that of the simulation with $\mu = 0.00205$ for both concretes, and the shape of the load *versus* displacement curve is different from the ones previously obtained. That demonstrates that increasing μ only for the concrete of highest strength influences the peak load, while increasing it only for the concrete of lowest strength practically does not impact the peak load. It also demonstrates that higher viscosity parameters associated with the concrete of highest strength in comparison with the one associated with the concrete of lowest strength leads to distortions in the shape of the load *versus* slip curve, while the opposite does not cause distortion in its shape.

The impact of the viscosity parameter on the convergence of the simulation and on its computational cost (evaluated mostly in terms of the time it took to process the models) were evident. That observation was expected in accordance with what was presented in Chapter 3 about the viscoplastic regularization of CDP models.

By decreasing the viscosity parameter from its initially adopted value of 0.007985, the computational cost to reach the end of the simulation (in other words, to reach a slip of 10 mm) increased immensely, so after reaching a slip of 2 to 3 mm, which are in the softening branch, it took a very long time to process each model. As the focus was to compare the behaviour around the peak load to the experimental results, the simulations were killed after reaching a satisfactory value for that purpose.

Taking that into consideration, it was necessary to find a combination of values that lead to both a peak load that was reasonably close to the experimentally obtained one and to an acceptable computational cost.

The importance of the viscoplastic regularization was highlighted by a simulation performed in Model I in which the viscosity parameter was set as $\mu = 0.00001 = 1\text{x}10^{-5}$ and the dilation angle was set as 28°. Its results, which are presented in Graph 4-7, allow the observation that the shape of the curve becomes distorted when the viscosity parameter is set to a value that is too small. The softening branch obtained in this

simulation reaches higher values than the supposed peak load, which is a completely unexpected behaviour for the proposed model.

As will be better discussed in the following section, it was necessary to balance the value of the dilation angle so a reasonable peak load could be obtained with viscosity values that were large enough to avoid this type of distortions.

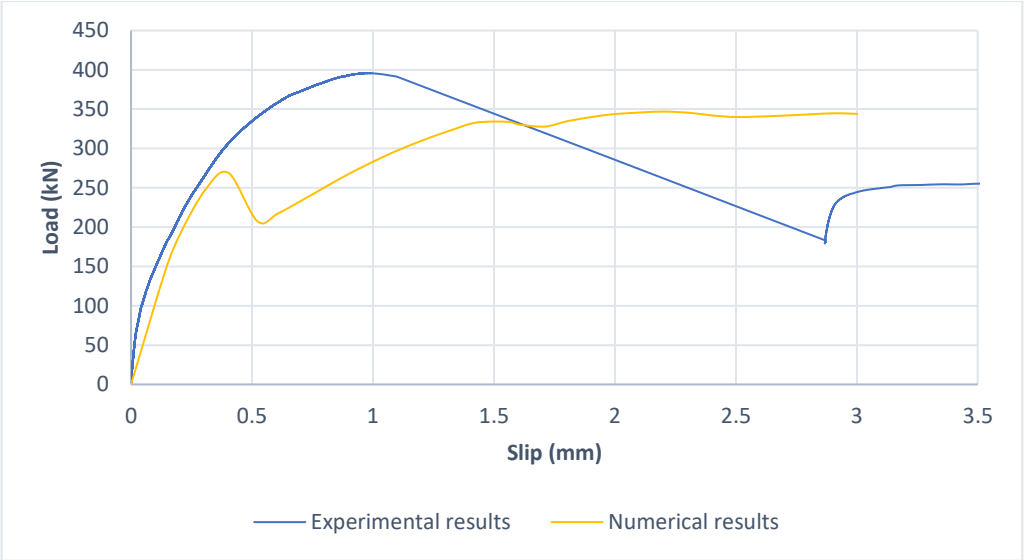

Graph 4-7 Results of Model I with μ= 0.00001

4.2. Dilation Angle

As the viscosity parameter, the dilation angle was also evaluated in the three different basic models (Models I, II and III), which are differentiated among each other by their tensile damage curves. The results explored in this section are presented in Graph 4-8, Graph 4-9 and Graph 4-10.

The values of viscosity adopted in the simulations presented in this section were 0.0018, 0.001 and 0.007985 respectively for Models I, II and III. The values of the remaining parameters were the same as the ones initially adopted.

Once again, in the analysis performed with Model III different values of dilation angle were introduced separately in the two concrete parts considered, while in the simulations performed with Models I and II the value introduced was always equal in both concrete parts in each analysis.

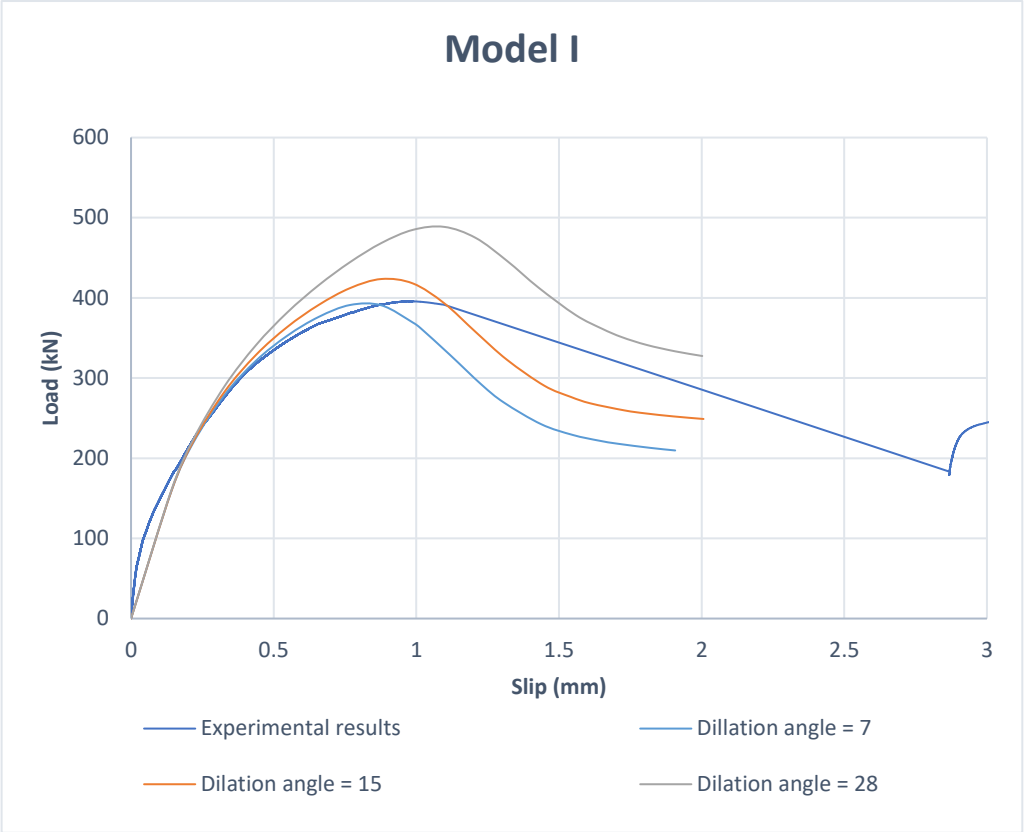

Graph 4-8 Dilation angle analysis in Model I

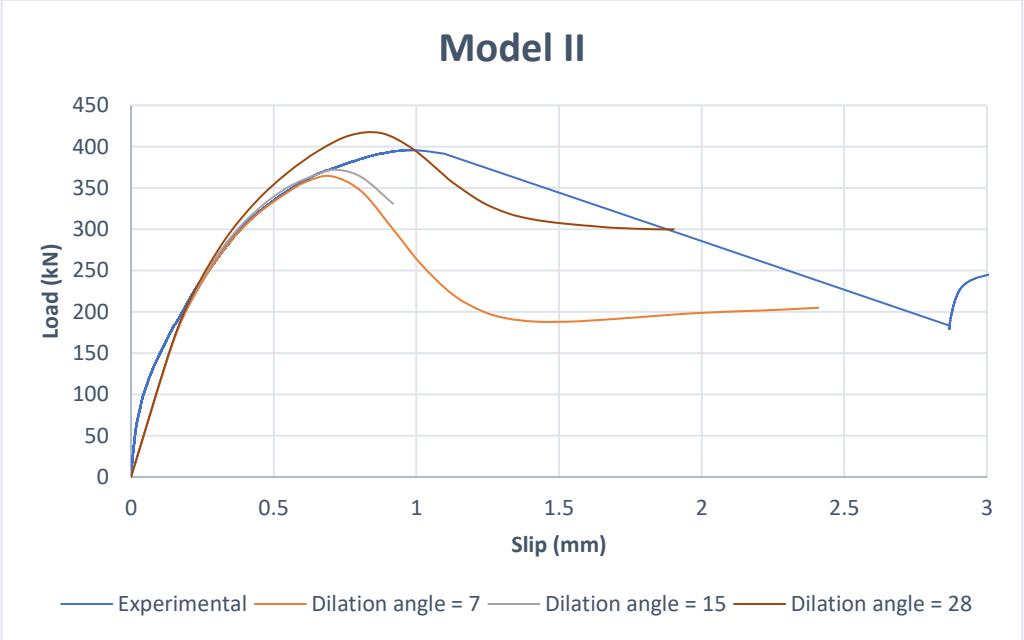

Graph 4-9 Dilation angle analysis in Model II

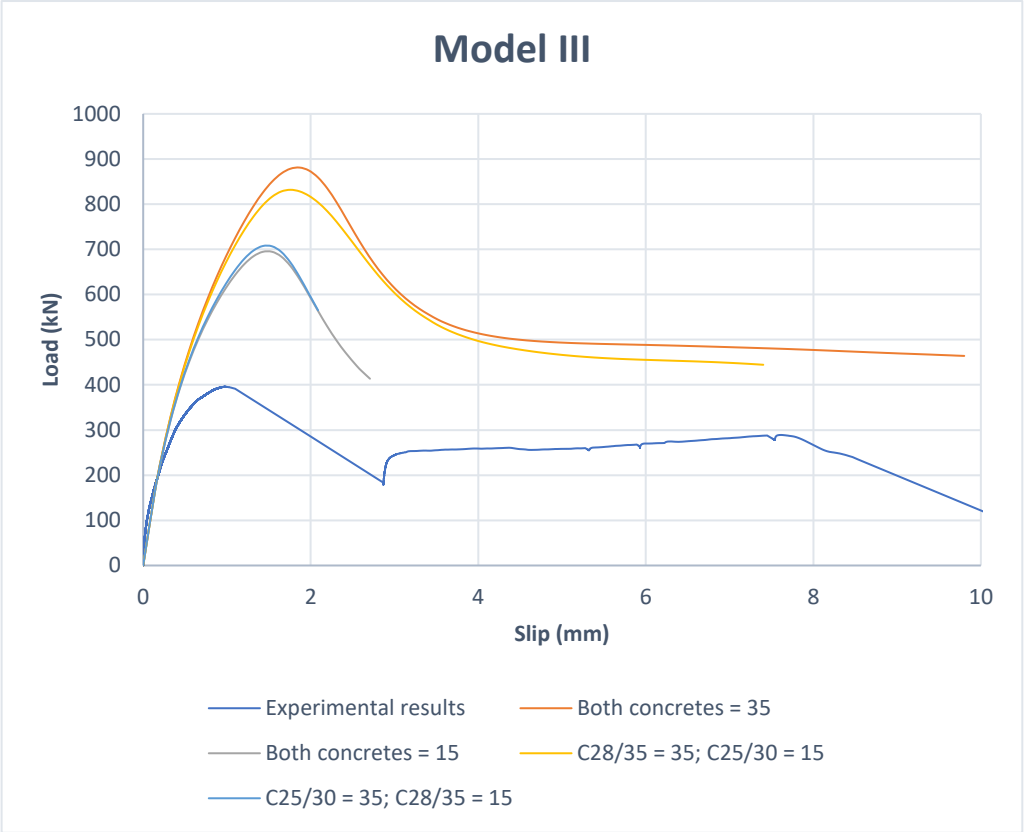

Graph 4-10 Dilation angle analysis in Model III

Observing the results, it becomes evident that the dilation angle also has a considerable influence on the value of the peak load, as was already introduced at the end of the previous section.

However, the sensibility of the peak load to variations in the dilation angle is considerably smaller than its sensitivity to variations in the viscosity parameter. For instance, in Model I to obtain an increase of 10.1% in the peak load it was necessary to increase the viscosity parameter by 38.5%, while to obtain an increase of 8.3% in the peak load the dilation angle had to be increased by 114.3%. In Model II, while an increase of 50% in the viscosity parameter led to an increase of 11.2% in the peak load, it was necessary to increase the dilation angle by 86.7% to obtain a similar increase in the peak load, of 12.0%.

As can be seen in Graph 4-11, the peak load and the dilation angle present an approximately linear direct relationship in the range of values considered, as was observed also for the viscosity parameter. Comparing Graph 4-11 to Graph 4-6 it can be seen that the linear trend that occurs for the viscosity parameter has a higher inclination than the one that occurs for the dilation angle, which agrees to the observations presented in the previous paragraph.

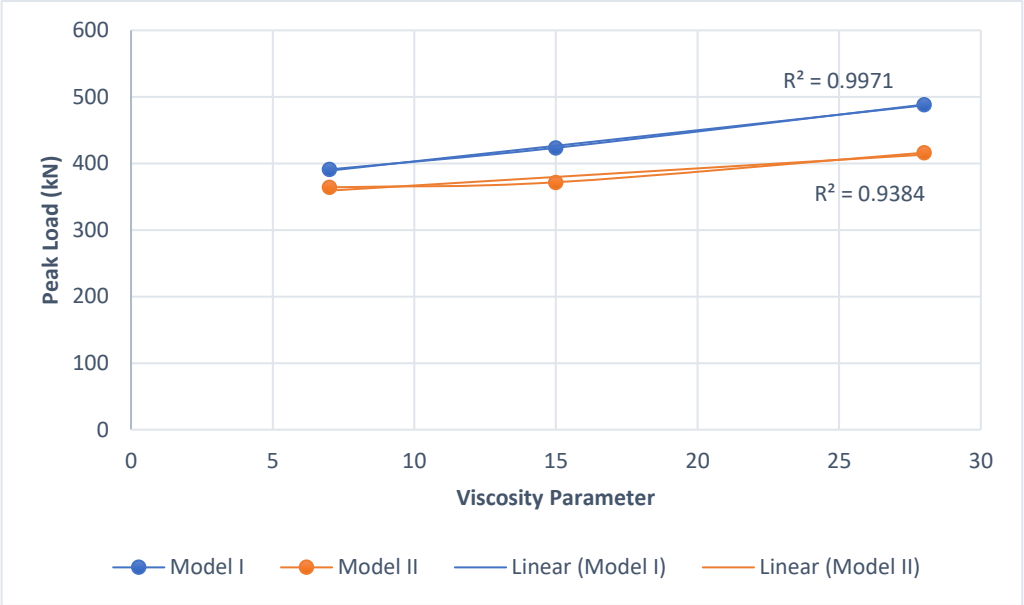

Graph 4-11 Peak Load variation according to the Dilation Angle

Observing the results of Model III, it is noticeable that the dilation angle of the concrete of higher strength (C28/35) is more influential on the value of the peak load than the dilation angle of the concrete of lowest strength (C25/30).

Comparing the results of the simulation in which both concretes had its dilation angles set as 15° to the ones of the simulation in which the dilation angle of C25/30 was set to 35° and the one of C28/35 was set to 15°, it can be seen that the peak loads obtained are practically the same. Therefore, one can conclude that setting a higher dilation angle value to the concrete of lowest strength in comparison to the one of highest strength has a small impact on the resulting peak load. However, it has a considerable impact on the computational cost, as the simulation with the different dilation angle values reached a smaller displacement value after running for approximately the same amount of time as the simulation with equal dilation angles in both concrete pieces.

Moreover, comparing the simulations in which both concretes had the same dilation angles, of 35° (orange curve) and 15° (grey curve) to the one in which the highest strength concrete was set with a higher dilation angle than the lowest strength concrete (namely, the dilation angle values were 35° and 15° respectively, represented by the yellow curve), it can be seen that the peak load obtained in the later is between the ones obtained in the other two mentioned simulations, considerably closer to the one with dilation angles of value 35°. That indicates that when a lower dilation angle is set to the concrete of lowest strength, both dilation angle values influence the peak load, being the concrete of highest strength more influential to the result. Furthermore, also in this comparison an impact on the computational cost can be observed, as the slip value

reached in the simulation with different dilation angle from one concrete to the other was also in-between the values reached in the other simulations. Comparing only the orange and yellow curves, it can be said that the decrease of lowest strength concrete's dilation angle led to a decrease in the slip value reached for a certain running time of the simulation.

4.3. Eccentricity

The analysis of the influence of the value set for the eccentricity of the concretes was made with Model II, adopting a viscosity parameter of 0.0013 and a dilation angle of 15°. The initially adopted value for the eccentricity, which was the value used in most simulations commented on in this report, was $\epsilon = 0.1$, as already mentioned. For the analysis, the half, $\epsilon = 0.05$, and the double, $\epsilon = 0.2$, of this value were used as input.

As can be seen in Graph 4-12 displayed below, the change of the eccentricity value led to practically no change in the load *versus* slip curve. For the simulation in which the eccentricity was set as 0.2, a small increase in the peak load could be noticed in comparison to the simulation in which $\epsilon = 0.1$. However, the curve around the peak load also presents a less smooth curvature for the simulation with $\epsilon = 0.2$, which is a non-desirable behaviour, as it is further from the behaviour of the experimentally obtained curve.

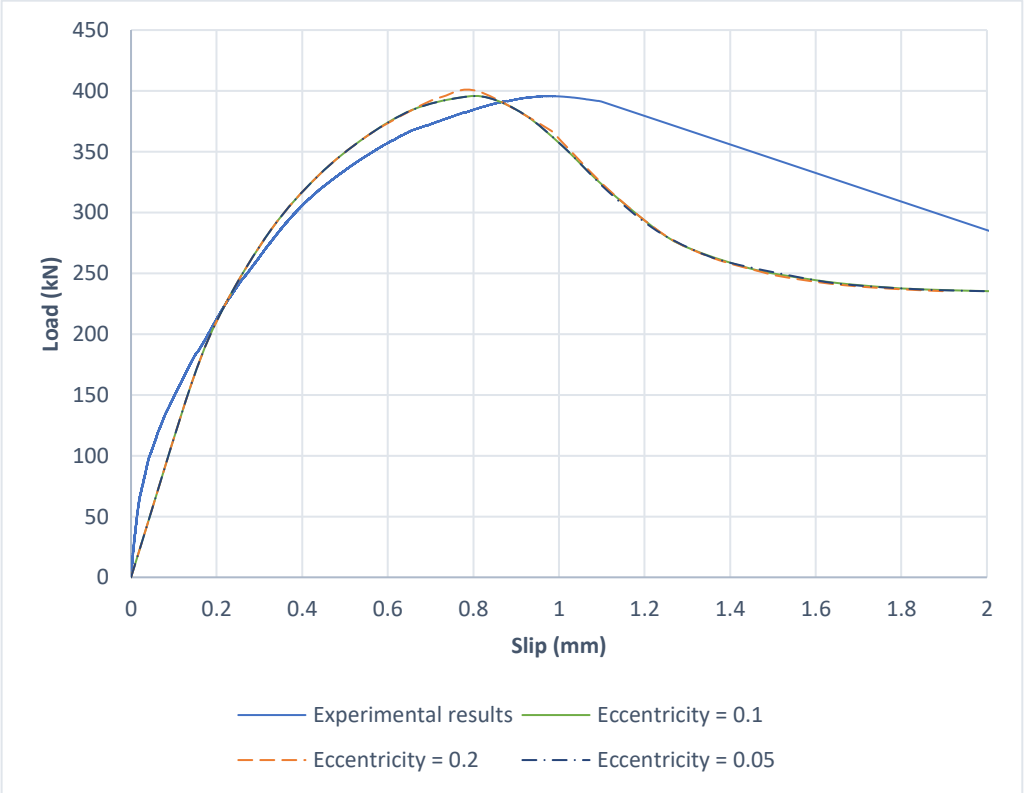

Graph 4-12 Eccentricity analysis in Model II

Taking those observations into consideration, it was decided to adopt the initial value, $\epsilon = 0.1$, for the remaining analysis.

4.4. Biaxial over Uniaxial Compression Strengths (f_{b0}/f_{c0})

The influence of the ratio between biaxial and uniaxial compression strengths (f_{b0}/f_{c0}) was analysed using as base Model II with a dilation angle of 15° and a viscosity parameter set as 0.0015. The value of $\frac{f_{b0}}{f_{c0}} = 1.16$, which was adopted in most models created for the analyses presented, including the initial one presented in Chapter 3, was chosen for the first simulation of this section. To analyse this parameter's influence on the results, the value $\frac{f_{b0}}{f_{c0}} = 2$ was chosen for the second simulation.

Observing the results presented in Graph 4-13 it becomes noticeable that the increase in f_{b0}/f_{c0} leads to an increase in the resulting loads. Even so, the change in the results is not very significant, especially in the branches before and close to the peak load. The previous statement can be illustrated by the fact that in the simulations performed an increase of 72.4% in the parameter f_{b0}/f_{c0} caused an increase of only 1.3% in the peak load.

Seeing as the impact of this parameter was found to be considerably small, it was decided to avoid further attempts of adjusting it, adopting the value $f_{b0}/f_{c0} = 1.16$ in all simulations with the exception of the second one created for this section's analysis.

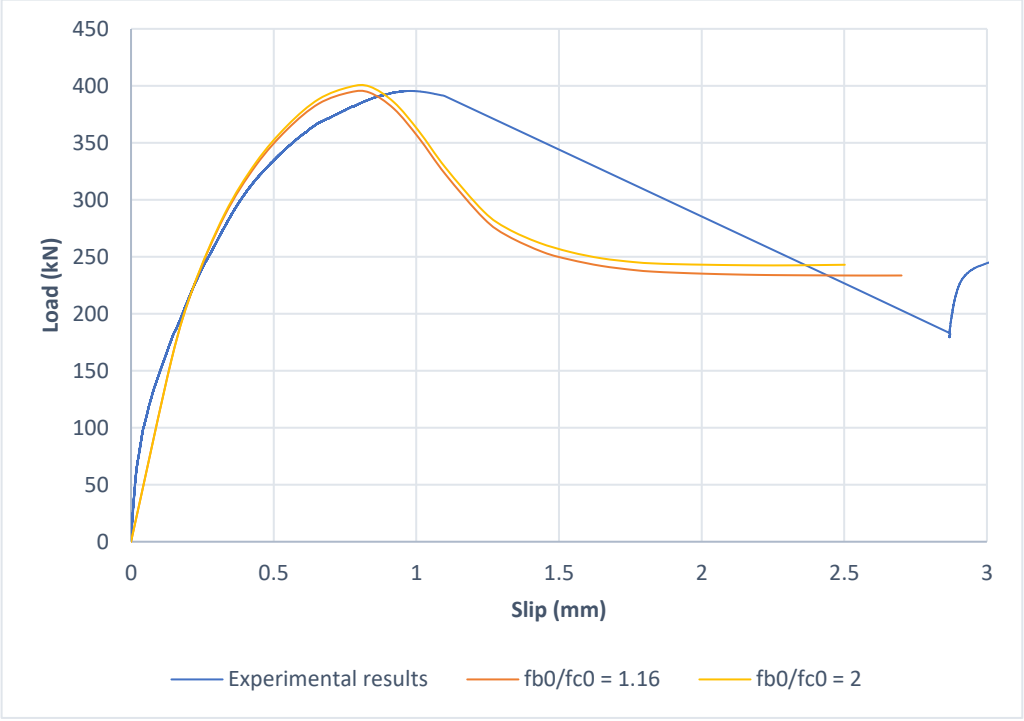

Graph 4-13 Strengths Ratio (f_{b0}/f_{c0}) analysis in Model II

4.5. Concrete's Strength Parameters

A comparison between Models I and II was made adopting a dilation angle of 15°, a viscosity parameter of 0.0015 and the remaining parameters with its initial values. Observing the results presented in Graph 4-14 it can be seen that Model II, which has higher values of concrete uniaxial tensile strength for both concretes, led to a higher peak load. In the graphs previously presented, which contain results that refer to only one model in each graph, the slip value associated to the peak load increases with the increase of the peak load. In this graph, however, the highest peak load is associated with a slightly smaller slip value than the one associated with the smallest peak load. That indicates that the concrete strength's parameters have an influence on the relationship between the value of the peak load and the value of the corresponding slip.

To better investigate the indication introduced, a comparison between the Models was made adjusting the parameters in each one to obtain similar peak load values in the three models' results. Observing the results in Graph 4-15 one could conclude that, for a fixed peak load, higher values of concrete uniaxial tensile strength lead to lower slip values associated with the peak load. In this study, the sequence from highest to lowest f_t' was Model II > Model I > Model III and the sequence from highest to lowest slip value associated with the peak was the opposite, Model III > Model I > Model II.

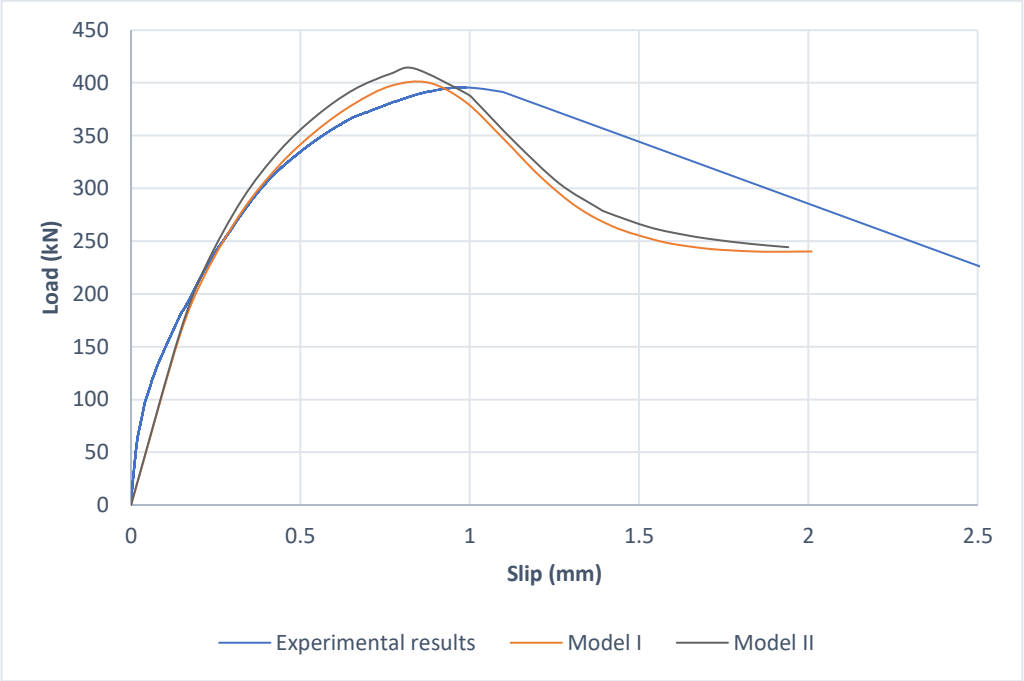

Graph 4-14 Comparison between results of Models I and II

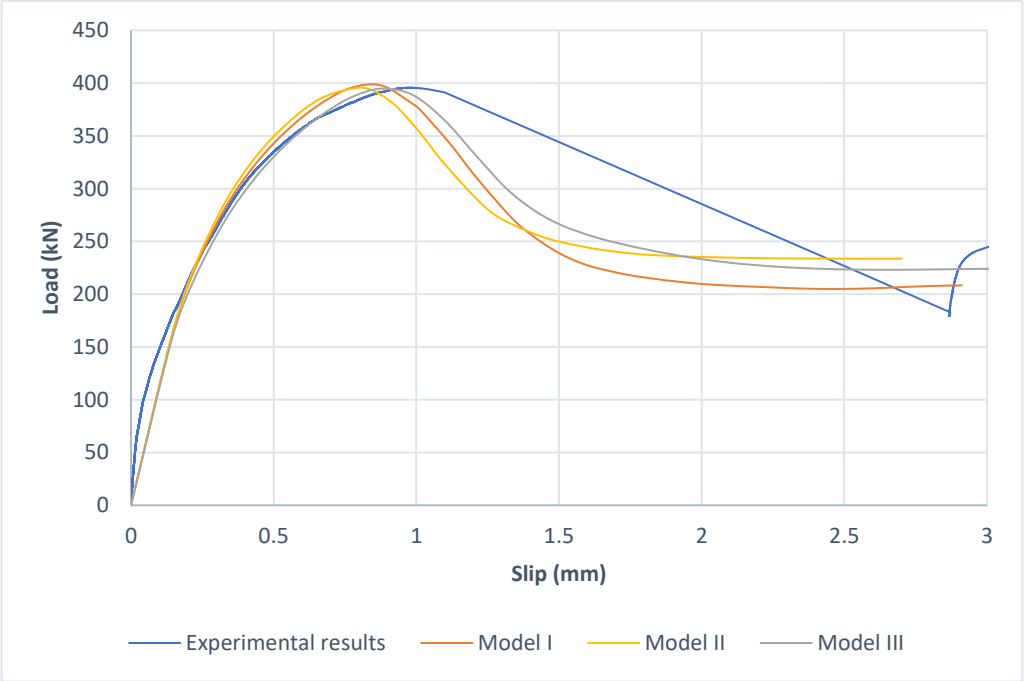

Graph 4-15 Comparison of curves with similar peak load values

The analysis of the fracture energy's influence on the load *versus* slip curve was made by changing its value in Model III, with adopted values of 15° for the dilation angle and 0.00205 for the viscosity parameters. Remaining parameters had their initial values maintained. The initial fracture energy value, presented in

Table 4-1, had its value increased and decreased by 20% for the simulations performed for this analysis. An additional simulation was performed, with the fracture energy set as 120 N/m for C25/30 and 125 N/m for C28/35. The purpose of this last simulation was to evaluate the effect of changing the ratio between the fracture energies of both concretes.

The results of the introduced simulations are presented in Graph 4-16. As it is considerably difficult to see differences in the results from one simulation to the other, one can conclude that the fracture energy's impact on the load *versus* slip curve is negligible. Therefore, the changes in results from one model to the other that were presented previously in this subsection can be attributed completely to the difference in the concrete uniaxial tensile strength values between the models.

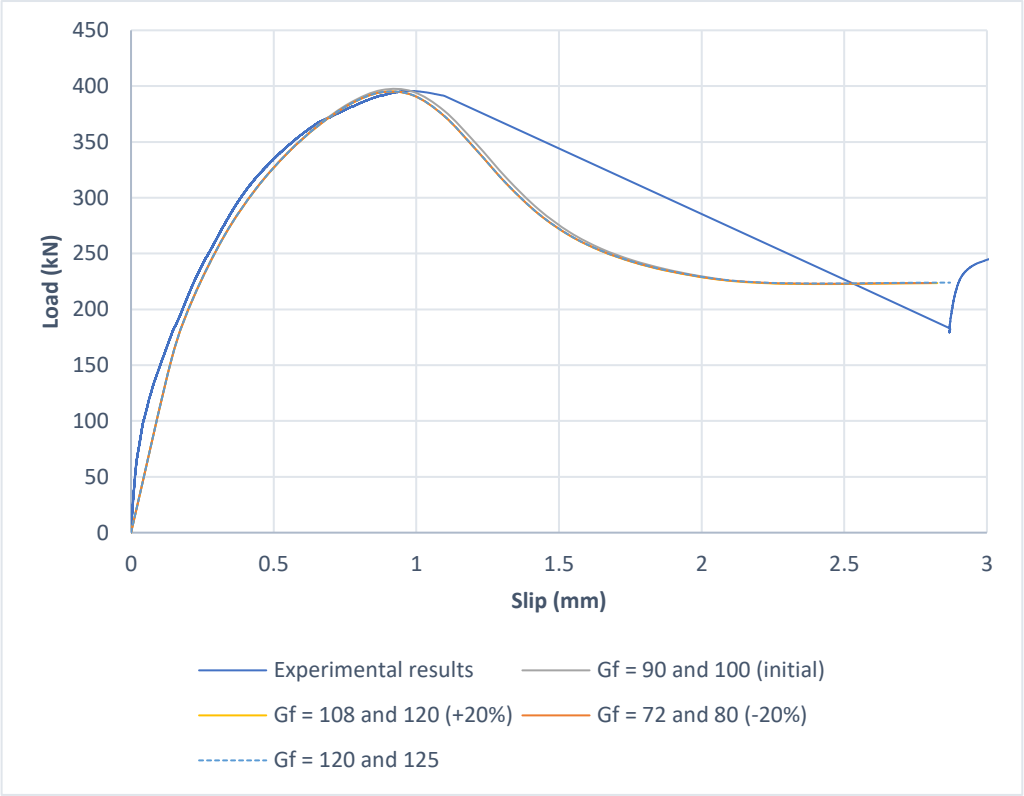

Graph 4-16 Analysis of fracture energy's impact on results

4.6. Additional Considerations about the Results

For the first final considerations of this chapter, a comparison was made using two simulations made with Model I in which the dilation angle and viscosity parameter were adjusted so similar peak load values were obtained in both simulations. The other parameters had their initial values maintained, and the values of dilation angle and viscosity parameter chosen, respectively, were 5° and 0.002 in the first simulation and 15° and 0.0015 in the second one.

The results of both simulations are presented in Graph 4-17. From them, two main conclusions were drawn. The first one is that those results are in agreement with what was commented on the previous section regarding the relation between the Model used, which is mainly dictated by the concrete's uniaxial tensile strengths defined, and the peak load – associated slip relationship. That is to say that for these simulations, which were made from the same model and resulted in very similar peak loads, the slip values associated to the peak obtained were practically the same in both of them, and that confirms the influence of f_t' on the slip value that was previously commented.

For the second conclusion, the load obtained after the softening branch is observed. Taking into consideration also the curves used for the analyses of dilation angle's and viscosity parameter's influences on the results, for instance the ones presented in Graph

4-3 and Graph 4-8, one can conclude that for models with similar peak loads the one with lowest viscosity parameter value will be the one with the highest final load (load kept approximately constant after the softening branch). Graph 4-8, in which the curves are differentiated only by their dilation angle values, and Graph 4-3, in which the curves are differentiated only by their viscosity parameter values, are useful to draw this conclusion because in the first graph one can observe that the curves are practically parallel to one another, while in the later the distance between the curves is diminished as the slip value increases.

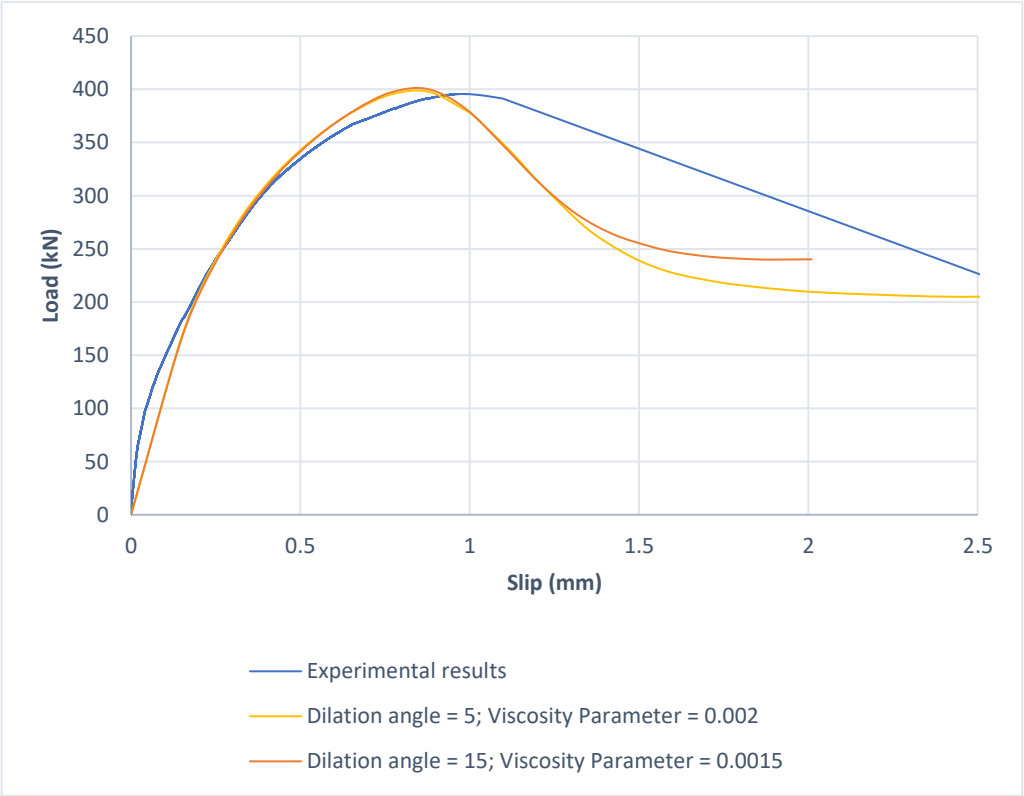

Graph 4-17 Analysis of dilation angle versus viscosity parameter

Finally, taking all the analyses presented into consideration, a combination of parameters that resulted in the curve closest to the experimental values was chosen for the models created for following analyses. Model III was chosen as base, and the remaining chosen values of parameters are presented in Table 4-4.

Table 4-4 Chosen plasticity inputs for CDP model

Dilation Angle	Eccentricity	f_{b0}/f_{c0}	K	Viscosity Parameter	
				C25/30	C28/35
15	0.1	1.16	0.667	0.006	0.00205

5. Chapter Five: Size effect analysis

From the validated model described in the previous chapters, a size effect analysis was proposed. The main purpose of this analysis was to evaluate how the size of the specimen influences on the obtained shear stress at the interface.

This chapter is dedicated to the description of the models created to perform the size effect analysis and the presentation of the results obtained and the conclusions drawn from them.

5.1. Modelling

Two additional models were created, using the validated model previously described as reference. The validated model will be identified as “Size I” in this chapter. The additional models will be identified as “Size II” and “Size III”. The values adopted for the input parameters on all models were the ones presented at the end of the previous chapter. Therefore, the models are only differentiated by their geometry.

For Size II, the dimensions of Size I in axis x and y were modified by application of a 0.5 factor, while the thicknesses (dimensions in z axis) were maintained. Similarly, for Size III the same modifications were made, but with the use of a 0.25 factor. The geometries of each model are presented in Figure 3-2, Figure 5-1 and Figure 5-2, respectively.

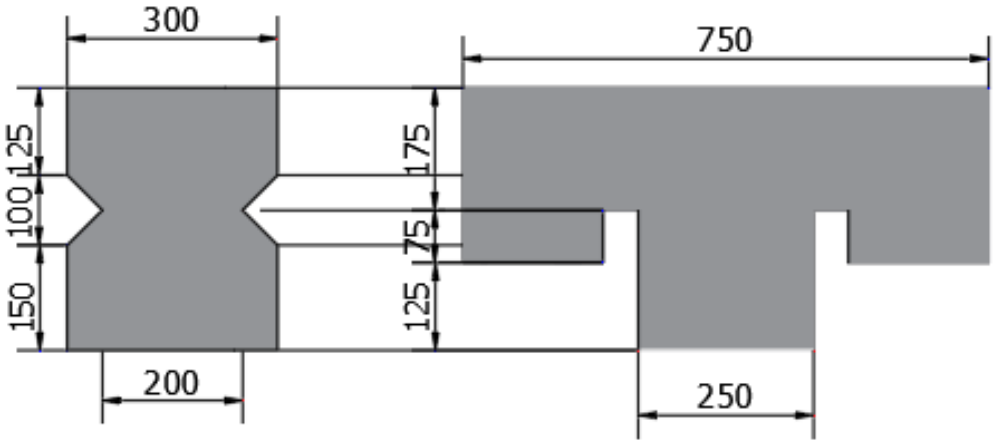

Figure 5-1 Dimensions of Size II model [mm]

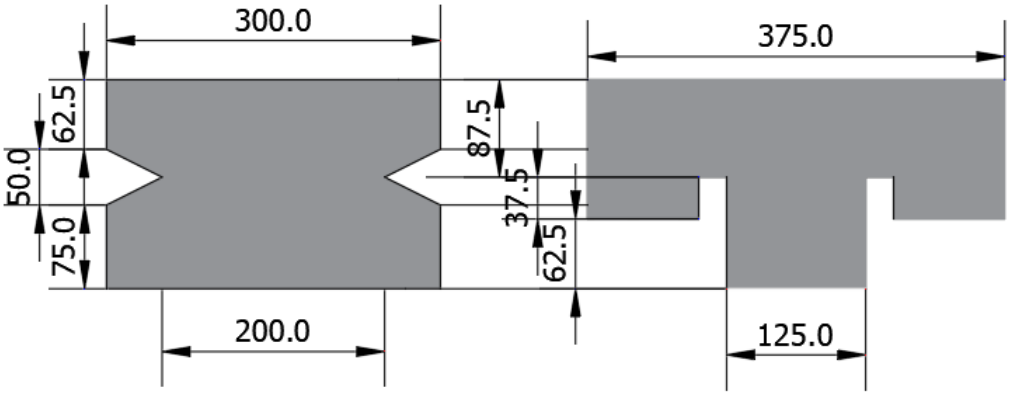

Figure 5-2 Dimensions of Size III model [mm]

In Size I model, as already mentioned, three steel anchor bars of diameter equal to 14 mm were used to connect the two concrete parts. In Size II model, only two anchor bars were modelled, with the same diameter as the previous model, and in Size III, one anchor bar was used, also maintaining the same diameter as the other models.

The mesh creation process was also the same for all models. The constraints and boundary conditions already presented were defined for all models. As the interactions defined refer to the anchor bars that connect both concrete parts, being each anchor associated to three interactions, only six interactions were defined for Size II and three interactions were defined for Size III, following the same reasoning as the ones defined for the original model.

5.2. Comparison of Resulting Loads

The Load *versus* Slip curves obtained for each one of the models are presented in Graph 5-1. From the graph, two main observations can be made. The first one is that the resulting loads decrease as the size of the specimen decreases. That is to say that the highest loads obtained were associated with Size I and the lowest loads were associated with Size III. The second observation is that ductility increases as the size of the specimen decreases. That becomes evident by the inclination of the curves, being higher ductility associated to smaller inclinations, in such a way that for a fixed load value, more ductile specimens have higher associated slip values.

To better evaluate the evolution of the loads according to the size of the specimen, the peak loads obtained were plotted against the contact area between both concrete parts of each model, as presented in Graph 5-2. A linear trendline was created for the data. Even though the trendline is well adjusted to the data, with $R^2 = 0.9806$, it is visibly noticeable that the peak loads do not increase linearly with the contact area's increase.

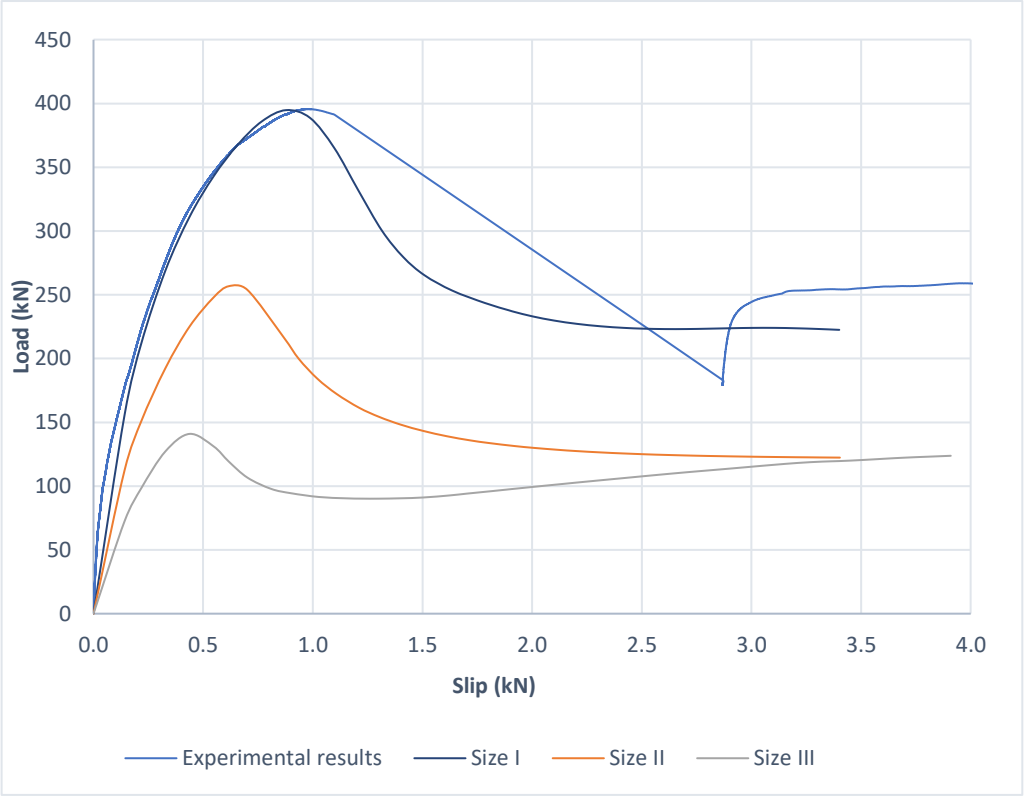

Graph 5-1 Load versus slip curves for Sizes I, II and III models

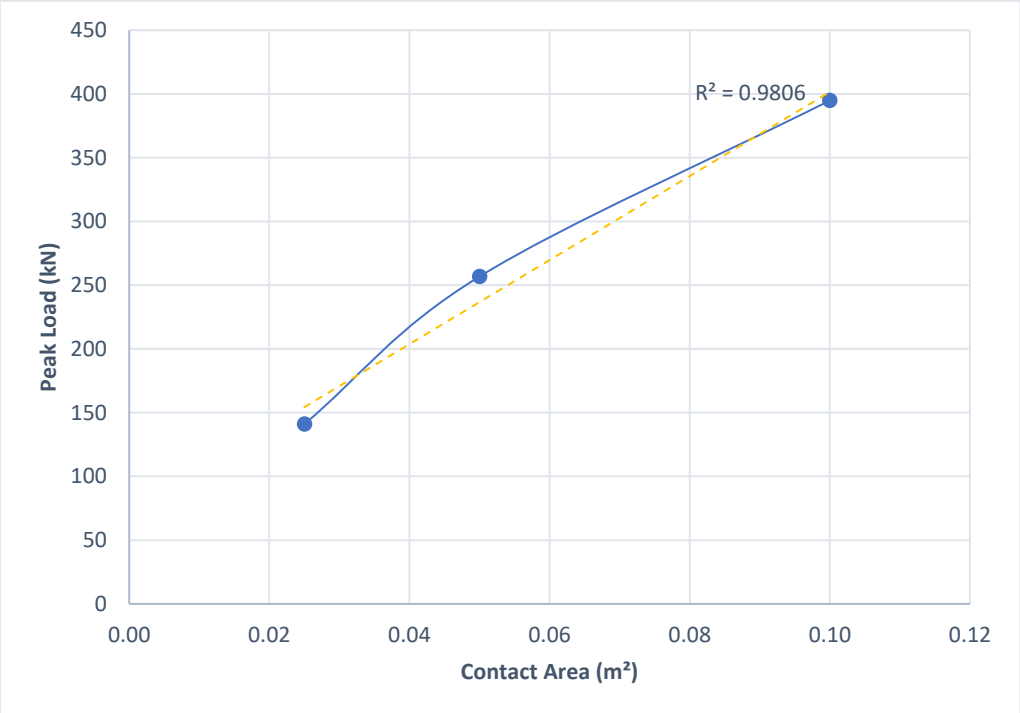

Graph 5-2 Peak load variation according to contact area

After evaluating the peak load *versus* contact area evolution, a new plot, presented in Graph 5-3, was created to evaluate the evolution of the maximum shear stress

obtained between the concrete pieces with the variation of the contact area. By visually inspecting the data, one can notice that the maximum shear stress decreases linearly with the increase of the contact area between the concrete parts, and therefore with the increase of the spacemen's size. A linear trendline was also created for the data in it, obtaining a nearly perfect adjustment, with $R^2 = 0.9984$. The trendline agrees with the conclusion that can be drawn from a visual inspection of the data.

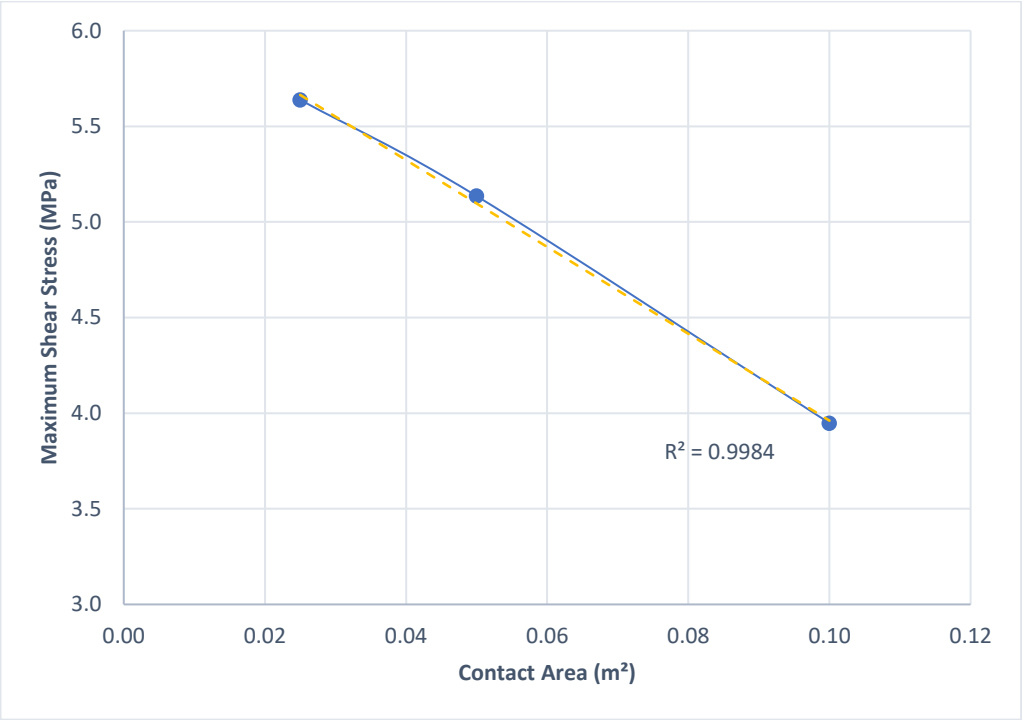

Graph 5-3 Maximum shear stress variation according to contact area

The results presented in this section were summarized in Table 5-1, presented below.

Table 5-1 Summary of results for size effect analysis

	Contact Area [mm x mm]	Peak Load [kN]	Displacement associated to Peak Load [mm]	Average Shear Strength [MPa]
Size I	500 x 200	394.81	0.878	3.95
Size II	250 x 200	256.77	0.617	5.14
Size III	125 x 200	140.96	0.438	5.64

5.3. Comparison of Displacements Distributions

The distribution of displacements is also affected by the change in the specimen's dimensions. By observing Figure 5-3, Figure 5-4 and Figure 5-5 one can confirm the previous statement, as it is visible that, in XY plane, for Size I model, the displacement

field is better described by lines almost parallel to x axis, while for Size II it is better described by lines with varying inclinations with respect to x axis and for Size III, by concentric quarters of circles. Despite the changes in the shape of the field, the lowest displacements are concentrated on the bottom left corner of the specimens for all three models considered.

Besides that, it is noticeable that as the dimensions of the specimen decrease, the portion of the specimen with practically zero displacement (dark blue in the figures below) also decreases. That is to say that the ratio between the volume of the region of null displacement and the total volume of the specimen decreases.

In the YZ plane, one can observe additionally that even though there is a change in the distribution of displacements, the symmetry with respect to y axis is maintained in all models. That is expected considering that in all models there is symmetry of the specimen, both concerning geometry and materials, and of the applied displacement with respect to y axis in this plane.

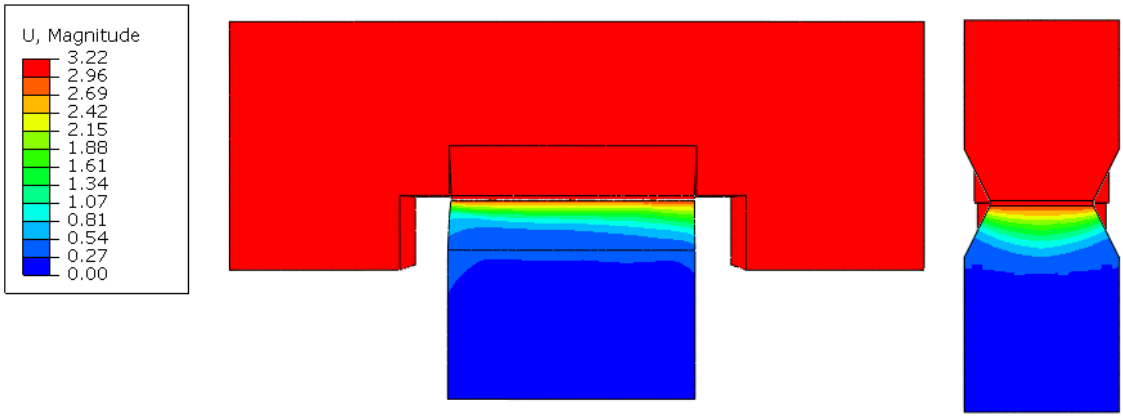

Figure 5-3 Distribution of Displacements in Size I model [mm]

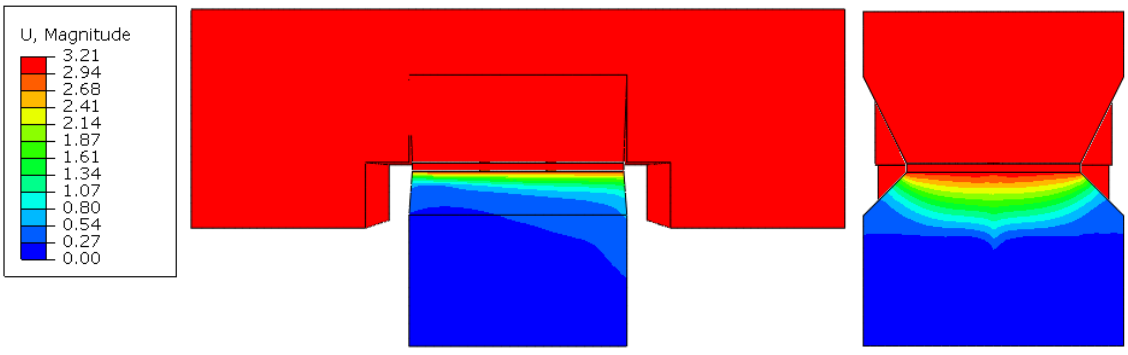

Figure 5-4 Distribution of Displacements in Size II model [mm]

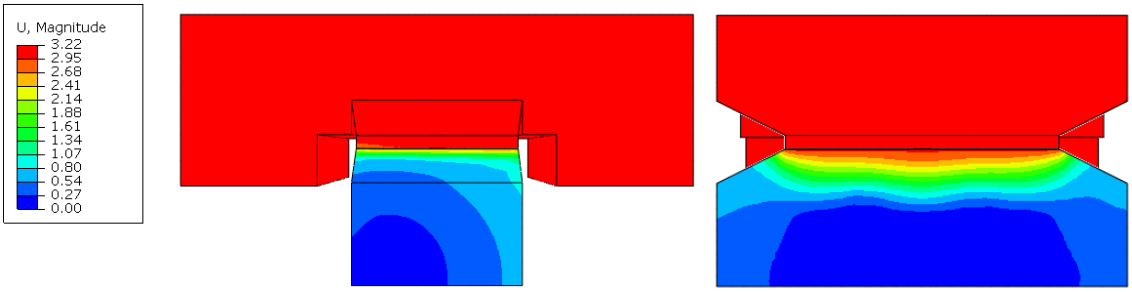

Figure 5-5 Distribution of Displacements in Size III model [mm]

5.4. Comparison of Damage Distributions

The distributions of compressive and tensile damages obtained in the simulations represent, respectively, the crushing pattern and the cracking pattern expected for the specimen.

Comparing Figure 5-6, Figure 5-7 and Figure 5-8, it is noticeable that the crushing pattern at the exterior of the specimen (that is to say, at points at the maximum and minimum coordinates in z axis) does not present significant changes as the size of the specimen is modified.

However, at the interior of the specimen, which can be observed in the YZ cut, the proportional penetration of the crushing damage increases as the size of the specimen decreases. A change in the shape of the crushing pattern can also be observed at the interior of the specimens, being the penetration under the extremities of the contact surface increasingly higher than the penetration at the middle.

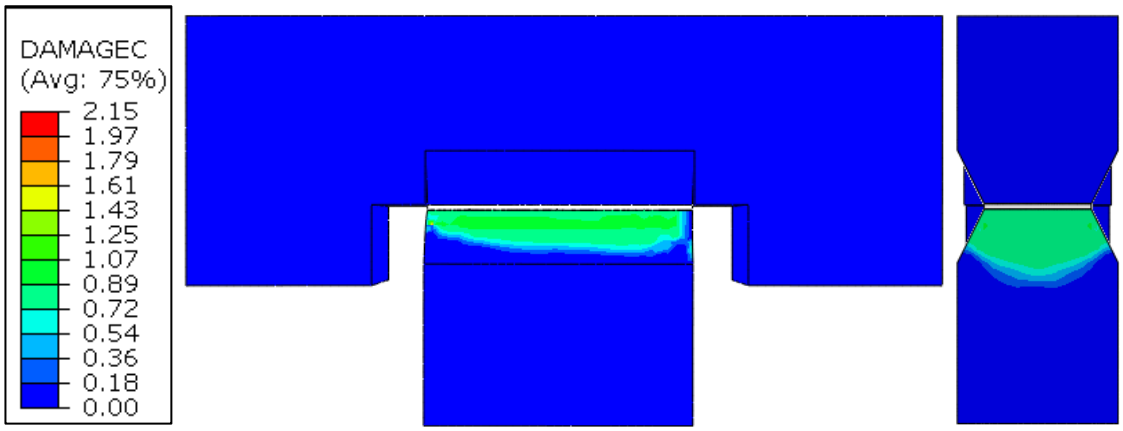

Figure 5-6 Distribution of Compressive Damage in Size I model

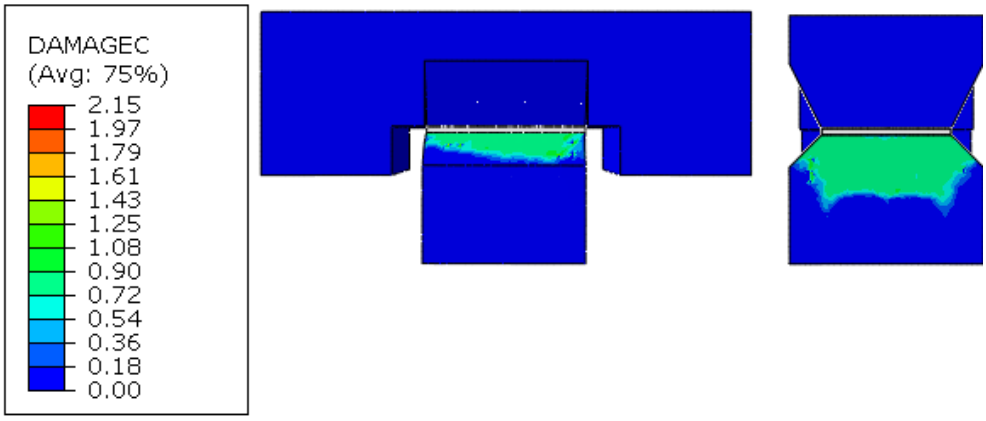

Figure 5-7 Distribution of Compressive Damage in Size II model

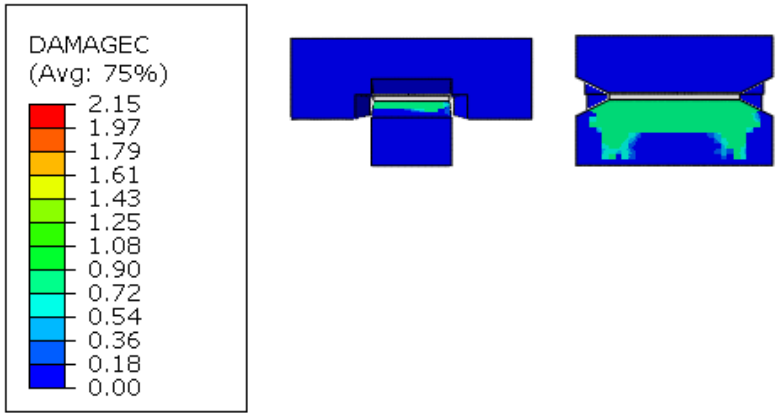

Figure 5-8 Distribution of Compressive Damage in Size III model

Regarding the cracking pattern, which can be observed in Figure 5-9, Figure 5-10 and Figure 5-11, similar changes to the crushing pattern can be observed in the YZ plane, concerning the cracks at the interior of the specimen. That is to say that an increase in the proportional penetration, specially under the extremities of the interface layer, can be observed.

However, at the extremities of the specimens, which can be observed in the XY plane representation, a slight decrease in the proportional penetration of the cracks occurs as the size of the specimen decreases. Despite that, the overall shape of the cracking pattern does not change significantly from one model to the other, being the cracked portion of the right larger than the one at the left.

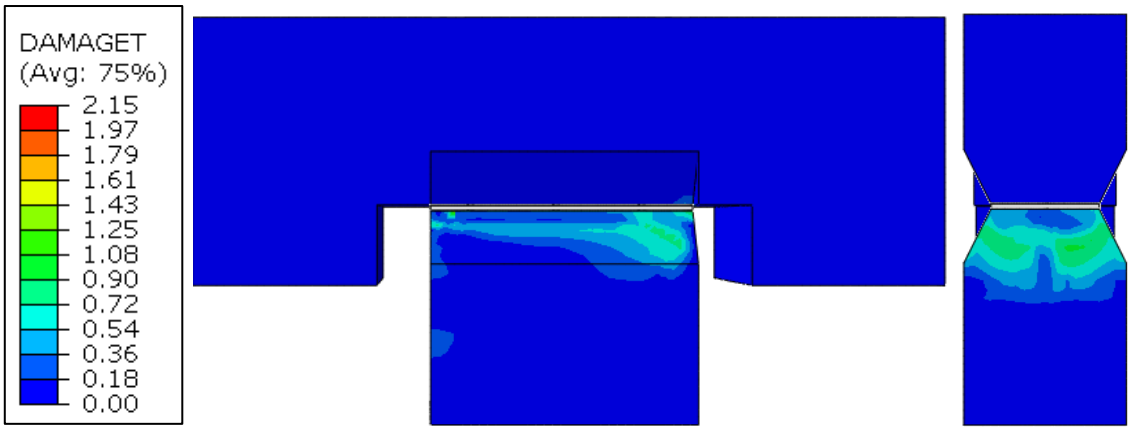

Figure 5-9 Distribution of Tensile Damage in Size I model

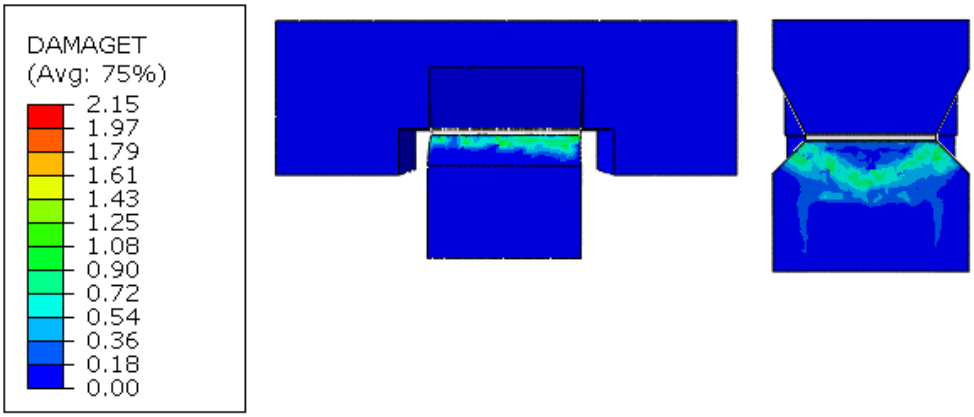

Figure 5-10 Distribution of Tensile Damage in Size II model

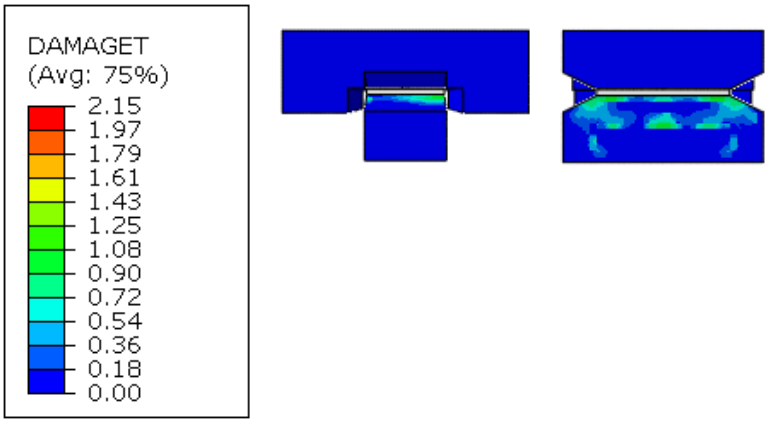

Figure 5-11 Distribution of Tensile Damage in Size III model

5.5. Comparison of Shear Stresses Distributions along the Interface

In this section, the shear stress along the interface will be presented for each model considering, in each one, two sections defining paths along the x axis: the first one at the middle of the interface, therefore passing through the anchors (path a) and the second one at one quarter of the interface (path b), as illustrated in Figure 5-12, for Size I model.

All stresses presented were extracted from the top of the interface layer, where it is in contact with the concrete of lowest strength and for slips of 3 mm.

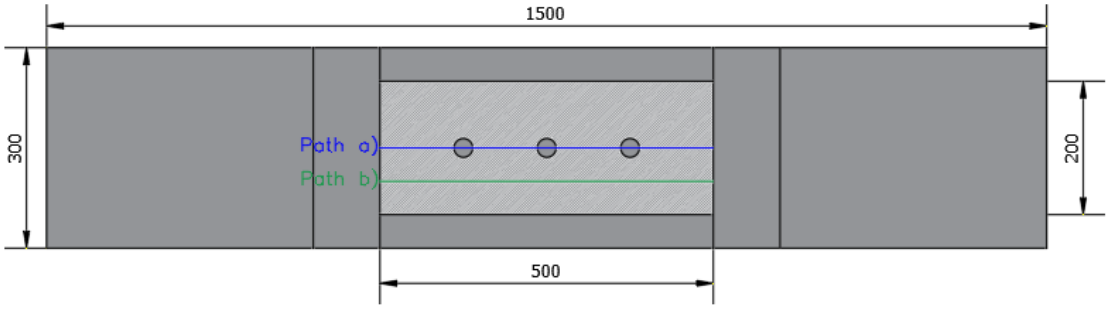

Figure 5-12 Position of paths a) and b) for Size I model

In Graph 5-4, Graph 5-6 and Graph 5-8, that contain the shear stresses along path a) in each model, the anchorage bars were included in the corresponding positions with its Von-Mises stresses represented by colours, in accordance with the scale presented in Figure 5-13. It is noticeable that in all models the higher values of shear stress occur at the initial section of the interface, that is, the section closest to point of application of displacement, and around the anchorage bars. Comparing the graphs, it can be seen that higher shear stresses near the anchors occur for models of smaller dimensions, namely, the highest shear stress occurs in Size III model, as occurred for the maximum shear stresses, presented previously in Graph 5-3. However, the shear stress values at the initial point of the interface decrease with the decrease in dimensions, in such a way that for Size I the highest shear stress occurs at that point while for Sizes II and III the shear stresses around the anchors surpass the ones at the initial section.

Graph 5-5, Graph 5-7 and Graph 5-9 present the shear stresses along path b) in the three models. It can be observed in them that the higher shear stresses occur at the beginning of the contact surface, in other words the section closest to the point of application of displacement, and then decrease along the x direction until reaching very small values near the end of the surface.

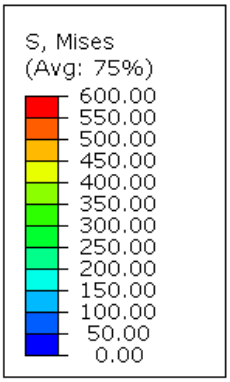

Figure 5-13 Scale of stresses used for the representation of the anchorage bars

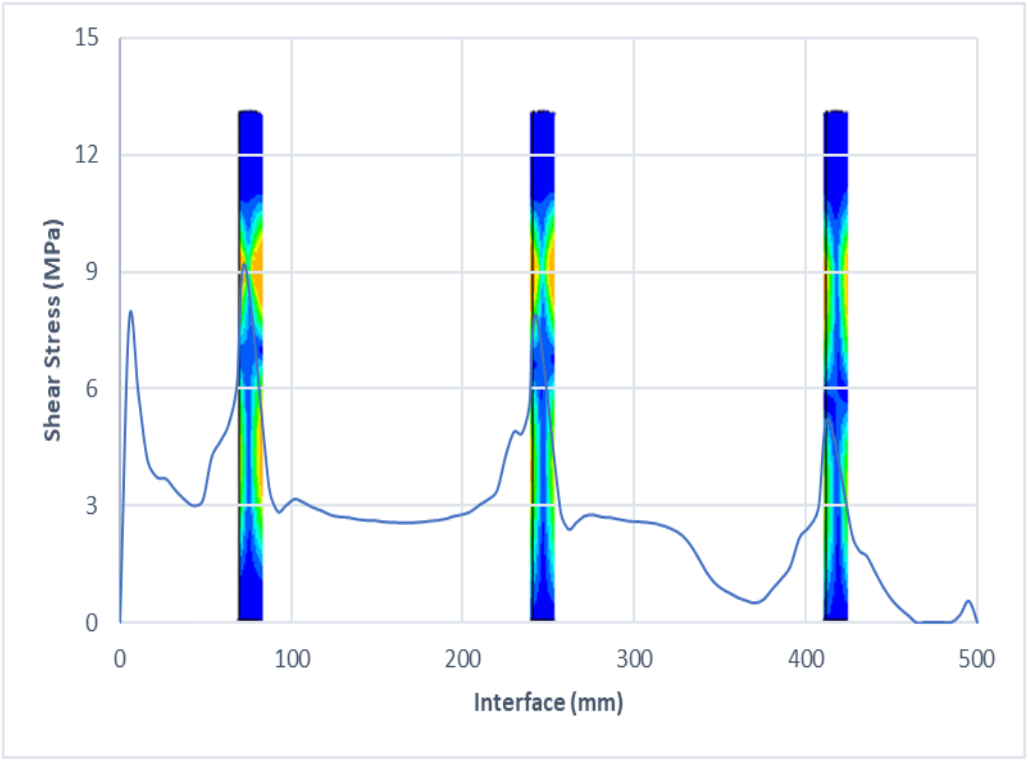

Graph 5-4 Shear stress along path a) in Size I model

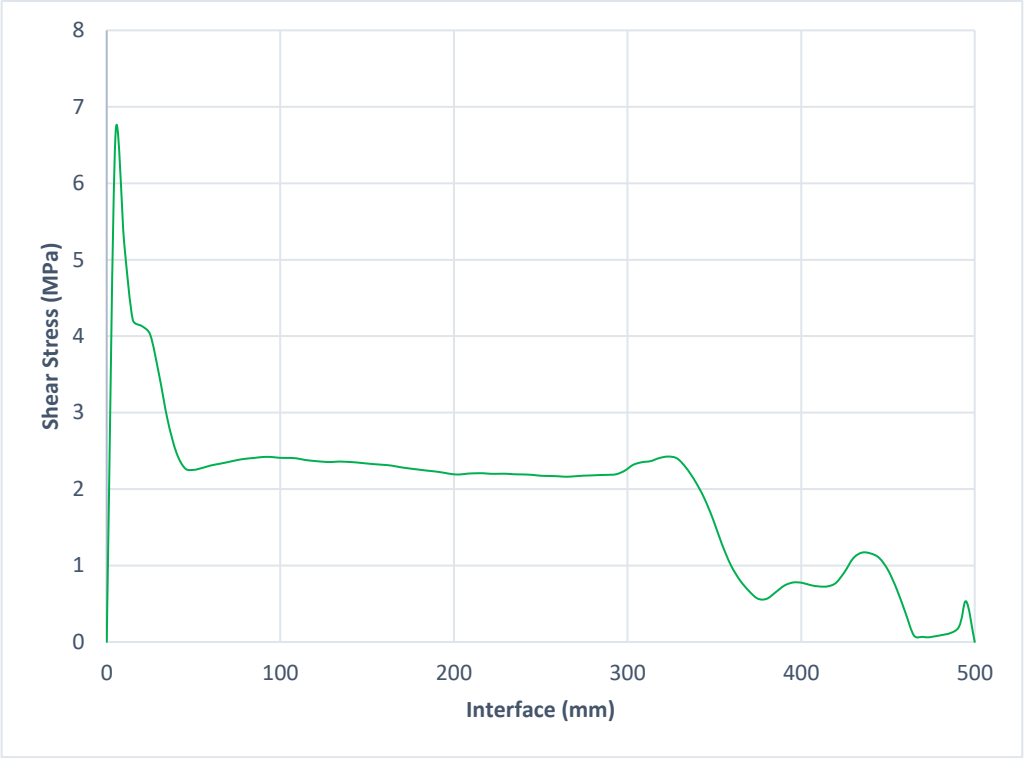

Graph 5-5 Shear stress along path b) in Size I model

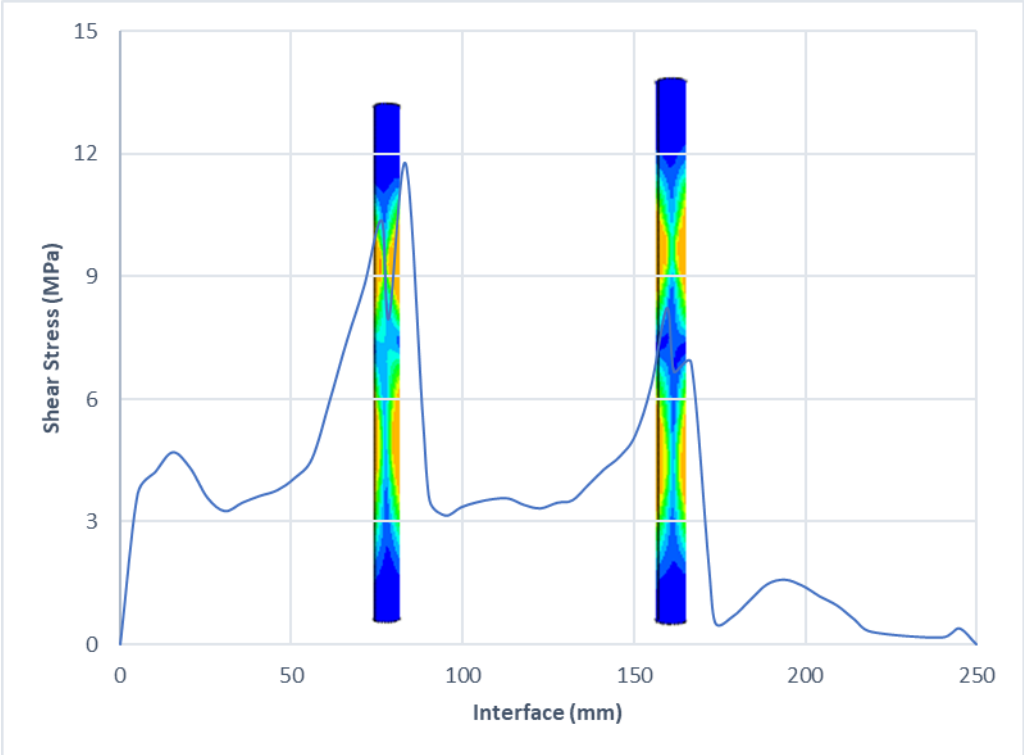

Graph 5-6 Shear stress along path a) in Size II model

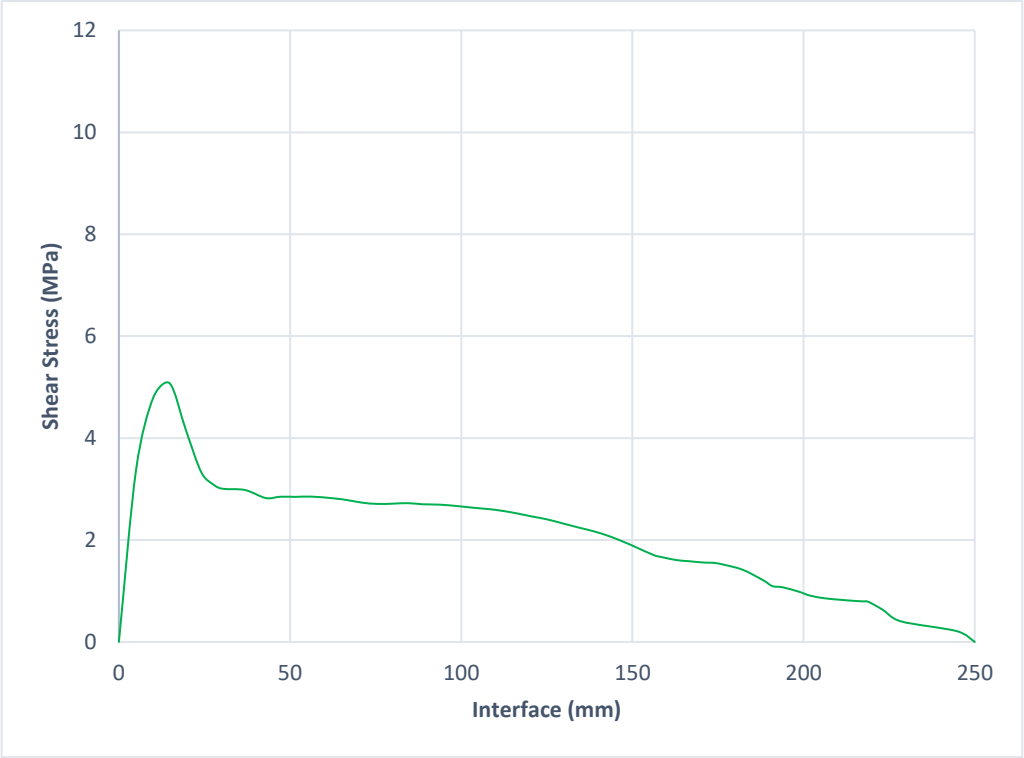

Graph 5-7 Shear stress along path b) in Size II model

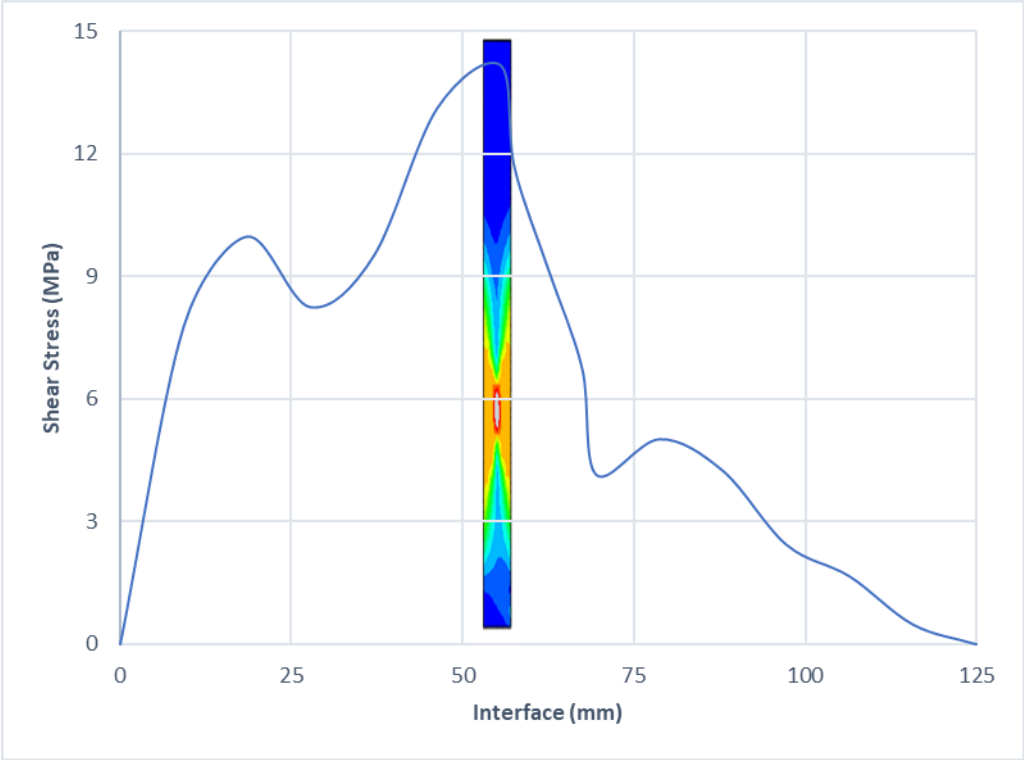

Graph 5-8 Shear stress along path a) in Size III model

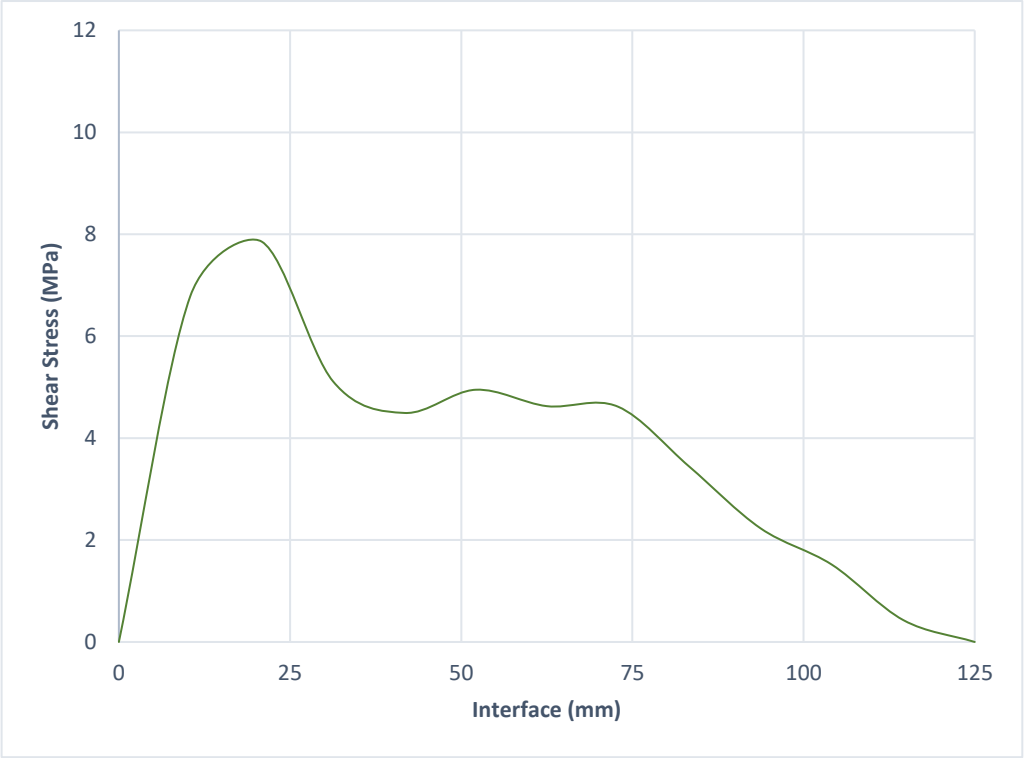

Graph 5-9 Shear stress along path b) in Size III model

5.6. Comparison of Principal Stresses Distributions

The principal maximum and minimum stresses in the anchors of each model are presented in this section, in Figure 5-14, Figure 5-15 and Figure 5-16. The anchors are presented in their deformed configuration. It can be noticed that the stress distribution and deformation are practically the same in Sizes I and II models. However, for Size III anchor, whose size was reduced proportionally to the dimensions of the specimen (namely, it was reduced by a 0.25 factor), the deformed shape is similar to the portion of same total length in Size I's anchor, and the stress distribution corresponds to it.

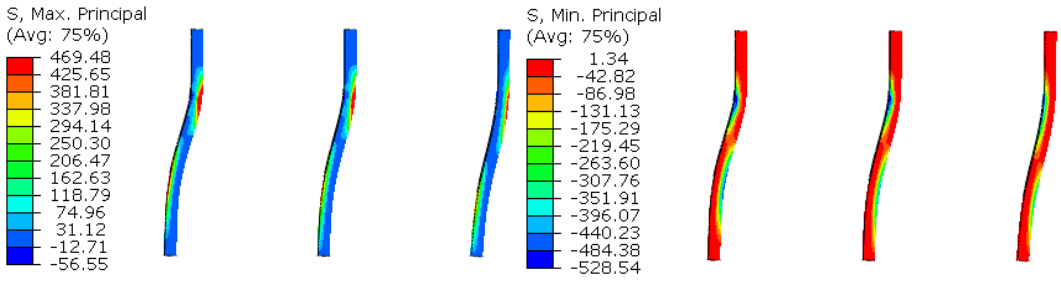

Figure 5-14 Maximum and minimal principal stresses in Size I model's anchors

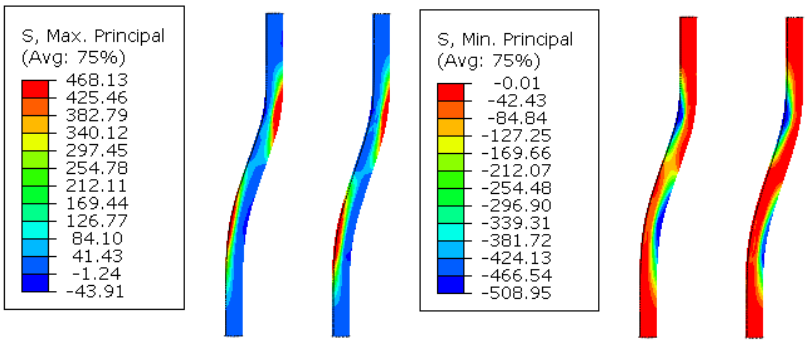

Figure 5-15 Maximum and minimal principal stresses in Size II model's anchors

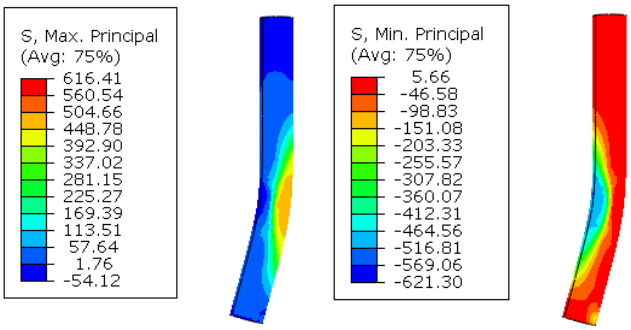

Figure 5-16 Maximum and minimal principal stresses in Size III model's anchor

In Figure 5-17, Figure 5-18 and Figure 5-19, the minimal principal stresses can be observed in the concrete layers of the three models. It is noticeable that the distribution of minimal principal stresses overall is of similar shape for all specimens' sizes studied, with the highest stresses (considering absolute values) of the top concrete layer concentrated at the left side, that is the one where the application of the displacement occurs, and at the points where the condition of orthogonality restraint is imposed (Reference Points 2 and 3). For the bottom concrete layer, stresses are of higher absolute value at the right side, specially near the point of imposition of restraints for this layer (Reference Point 5).

Around the interface, there can be made similar observations to the ones made in the previous subsection, concerning the shear stresses along path b) at the contact surface. That is to say that it can be seen that higher absolute values of stresses occur at the left of the contact area, decreasing going to the right along the x axis. Additionally, higher absolute values of minimal principal stresses occur for models of smaller dimensions, as occurs for the shear stresses.

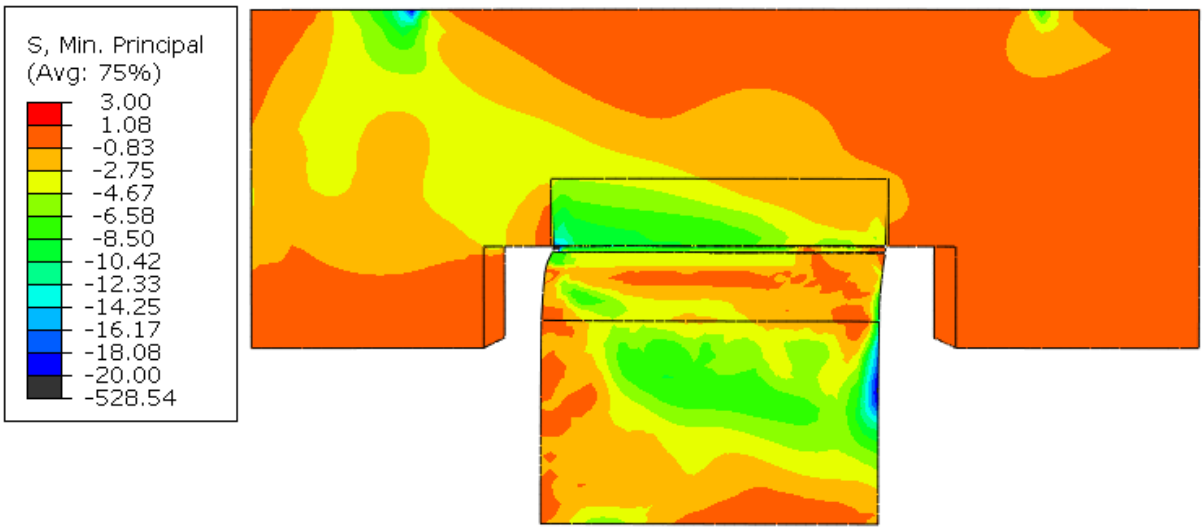

Figure 5-17 Minimal principal stresses in Size I model

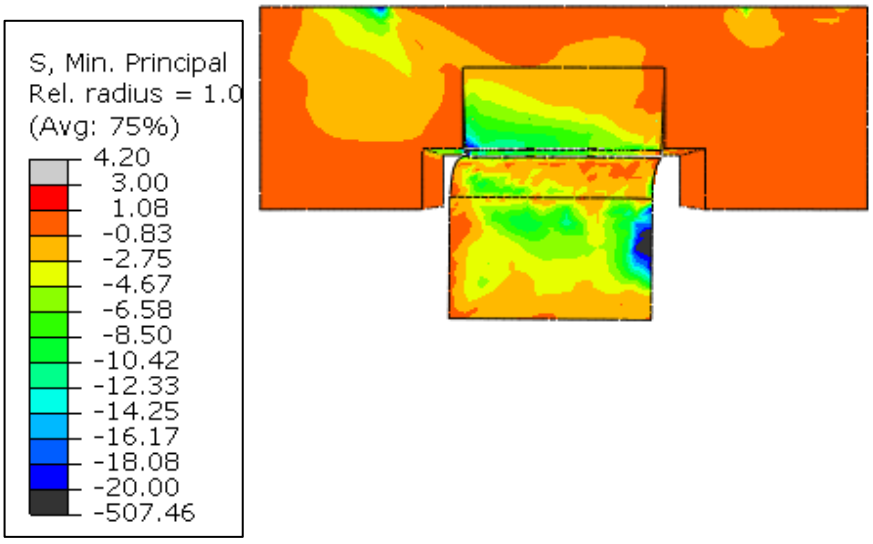

Figure 5-18 Minimal principal stresses in Size II model

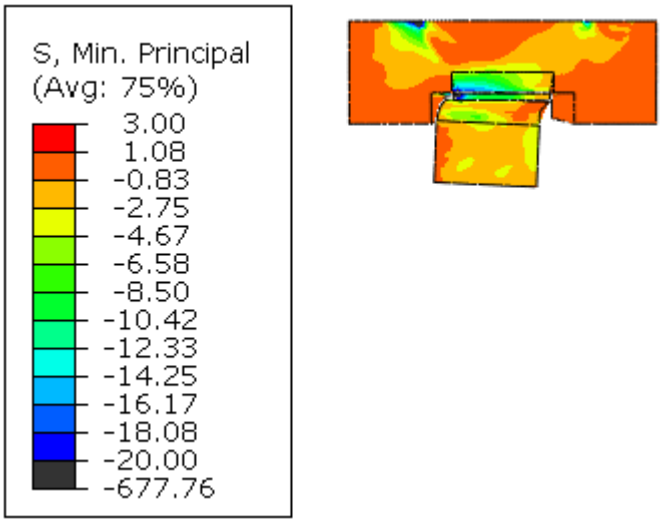

Figure 5-19 Minimal principal stresses in Size III model

6. Chapter Six: Analysis of concrete strength's influence

Starting again from the validated model described in previous chapters, an analysis was performed to evaluate the effect of concrete strength on the behaviour of concrete-to-concrete interfaces. High strength concretes were included in the study.

This chapter is dedicated to the description of the Abaqus models created for the performance of the analysis and to the presentation and discussion of the results obtained from them.

6.1. Modelling

Five models were used for the analysis proposed in this chapter. The first one is the model that resulted from the validation process, presented at the end of Chapter 3. The other models were created by modifying the material parameters of the first model, specifically their Young's modulus and damage and tensile curves. The concrete strength classes chosen for each model, respectively for the existing concrete layer (top layer, with lower concrete strength) and for the added concrete (bottom layer, with higher concrete strength) were:

- Model I: C25/30 and C28/35;
- Model II: C25/30 and C60/75;
- Model III: C28/35 and C60/75;
- Model IV: C25/30 and C90/105;
- Model V: C60/75 and C90/105.

The geometry of concrete parts, anchors and reinforcement bars, meshing, constraints, boundary conditions and interactions are therefore identical for all models, as are the material parameters in the Plasticity section of Concrete Damaged Plasticity models, that were presented previously, in Table 4-4.

The material parameters for C25/30 and C28/35 have been previously presented in Chapters 3 and 4, in Table 3-3 and Table 4-3. The parameters of C60/75 and C90/105, specified in accordance with Table 3.1 of Eurocode 2 and with the methodology for determining damage curves presented in Chapter 3, are presented below, in Table 6-1, Table 6-2 and Table 6-3.

Table 6-1 Material parameters of C60/75 and C90/105

	E_{cm} (GPa)	f_{cm} (MPa)	G_f (N/m)	f_t (MPa)	W_c (mm)
C60/75	39	68	103.1	3.1	0.171
C90/105	44	98	110.1	3.5	0.162

Table 6-2 Tensile damage curve for C60/75 and C90/105

C60/75		
W (mm)	**б (MPa)**	**d**
0.000	3.100	0.000
0.009	2.195	0.272
0.017	1.584	0.469
0.026	1.183	0.598
0.034	0.926	0.681
0.043	0.758	0.735
0.051	0.645	0.772
0.060	0.562	0.799
0.068	0.495	0.820
0.077	0.436	0.839
0.085	0.382	0.857
0.094	0.330	0.874
0.103	0.280	0.890
0.111	0.233	0.905
0.120	0.189	0.919
0.128	0.149	0.932
0.137	0.112	0.944
0.145	0.079	0.955
0.154	0.049	0.964
0.162	0.023	0.973
0.171	0.000	0.980

C90/105		
W (mm)	**б (MPa)**	**d**
0.000	3.500	0.000
0.008	2.479	0.272
0.016	1.788	0.469
0.024	1.336	0.598
0.032	1.045	0.681
0.040	0.856	0.735
0.049	0.728	0.772
0.057	0.634	0.799
0.065	0.559	0.820
0.073	0.492	0.839
0.081	0.431	0.857
0.089	0.372	0.874
0.097	0.316	0.890
0.105	0.263	0.905
0.113	0.214	0.919
0.121	0.168	0.932
0.129	0.126	0.944
0.137	0.089	0.955
0.146	0.055	0.964
0.154	0.026	0.973
0.162	0.000	0.980

Table 6-3 Compressive damage curves for C60/75 and C90/105

C60/75		
ε	**б (MPa)**	**d**
0.00E+00	30.600	0.000
8.27E-05	38.400	0.000
1.50E-04	45.000	0.000
2.36E-04	50.400	0.000
3.41E-04	54.600	0.000
4.64E-04	57.600	0.000
6.06E-04	59.400	0.000
7.67E-04	60.000	0.000
8.60E-04	59.434	0.009

C90/105		
ε	**б (MPa)**	**d**
0.00E+00	45.900	0.000
8.27E-05	57.600	0.000
1.50E-04	67.500	0.000
2.36E-04	75.600	0.000
3.41E-04	81.900	0.000
4.64E-04	86.400	0.000
6.06E-04	89.100	0.000
7.67E-04	90.000	0.000
8.60E-04	89.151	0.009

9.69E-04	57.895	0.035
1.09E-03	55.645	0.073
1.22E-03	52.941	0.118
1.35E-03	50.000	0.167
1.48E-03	46.988	0.217
1.61E-03	44.022	0.266
1.74E-03	41.176	0.314
1.87E-03	38.496	0.358
1.99E-03	36.000	0.400
2.11E-03	33.696	0.438
2.23E-03	31.579	0.474
2.34E-03	29.641	0.506
2.46E-03	27.869	0.536
2.57E-03	26.250	0.563
2.67E-03	24.771	0.587
2.78E-03	23.418	0.610
2.88E-03	22.179	0.630
2.99E-03	21.043	0.649
3.09E-03	20.000	0.667
3.19E-03	19.040	0.683
3.29E-03	18.156	0.697
3.39E-03	17.339	0.711
3.48E-03	16.583	0.724
3.58E-03	15.882	0.735
3.67E-03	15.232	0.746
3.77E-03	14.627	0.756
3.86E-03	14.063	0.766
3.95E-03	13.536	0.774
4.05E-03	13.043	0.783
4.14E-03	12.582	0.790
4.23E-03	12.150	0.798
4.32E-03	11.743	0.804
4.41E-03	11.360	0.811
4.50E-03	11.000	0.817
4.59E-03	10.660	0.822
4.68E-03	10.339	0.828
4.77E-03	10.035	0.833
4.86E-03	9.747	0.838
4.95E-03	9.474	0.842

9.69E-04	86.842	0.035
1.09E-03	83.468	0.073
1.22E-03	79.412	0.118
1.35E-03	75.000	0.167
1.48E-03	70.482	0.217
1.61E-03	66.033	0.266
1.74E-03	61.765	0.314
1.87E-03	57.743	0.358
1.99E-03	54.000	0.400
2.11E-03	50.543	0.438
2.23E-03	47.368	0.474
2.34E-03	44.461	0.506
2.46E-03	41.803	0.536
2.57E-03	39.375	0.563
2.67E-03	37.156	0.587
2.78E-03	35.127	0.610
2.88E-03	33.268	0.630
2.99E-03	31.565	0.649
3.09E-03	30.000	0.667
3.19E-03	28.560	0.683
3.29E-03	27.233	0.697
3.39E-03	26.008	0.711
3.48E-03	24.874	0.724
3.58E-03	23.824	0.735
3.67E-03	22.848	0.746
3.77E-03	21.940	0.756
3.86E-03	21.094	0.766
3.95E-03	20.304	0.774
4.05E-03	19.565	0.783
4.14E-03	18.873	0.790
4.23E-03	18.224	0.798
4.32E-03	17.614	0.804
4.41E-03	17.041	0.811
4.50E-03	16.500	0.817
4.59E-03	15.990	0.822
4.68E-03	15.508	0.828
4.77E-03	15.052	0.833
4.86E-03	14.620	0.838
4.95E-03	14.211	0.842

6.2. Comparison of Resulting Loads

The Load *versus* Slip curves obtained for each one of the models are presented in Graph 6-1. From the graph, it is possible to observe that there is a considerable increase in the loads for models with high strength concretes compared to Model I, that has only normal strength. Meanwhile, comparing the models with high strength concretes between each other, it is possible to see that there is a variation in the load, but it is less significant than the variation from Model I. The overall shape of the curve does not vary significantly from one model to the other, however a change in the stiffness of the curves can be seen. That is associated with the ductility of the models, being higher stiffness associated with smaller ductility.

To better evaluate the changes of load and ductility, two additional graphs were elaborated. In Graph 6-2, the peak loads obtained were plotted against the characteristic cylinder compressive strength of the added concrete. Different colours and formats were used to identify the concrete strength class of the existing concrete. In a similar manner, Graph 6-3 presents the plot of the slip values associated with the peak load against the characteristic cylinder compressive strength of the added concrete.

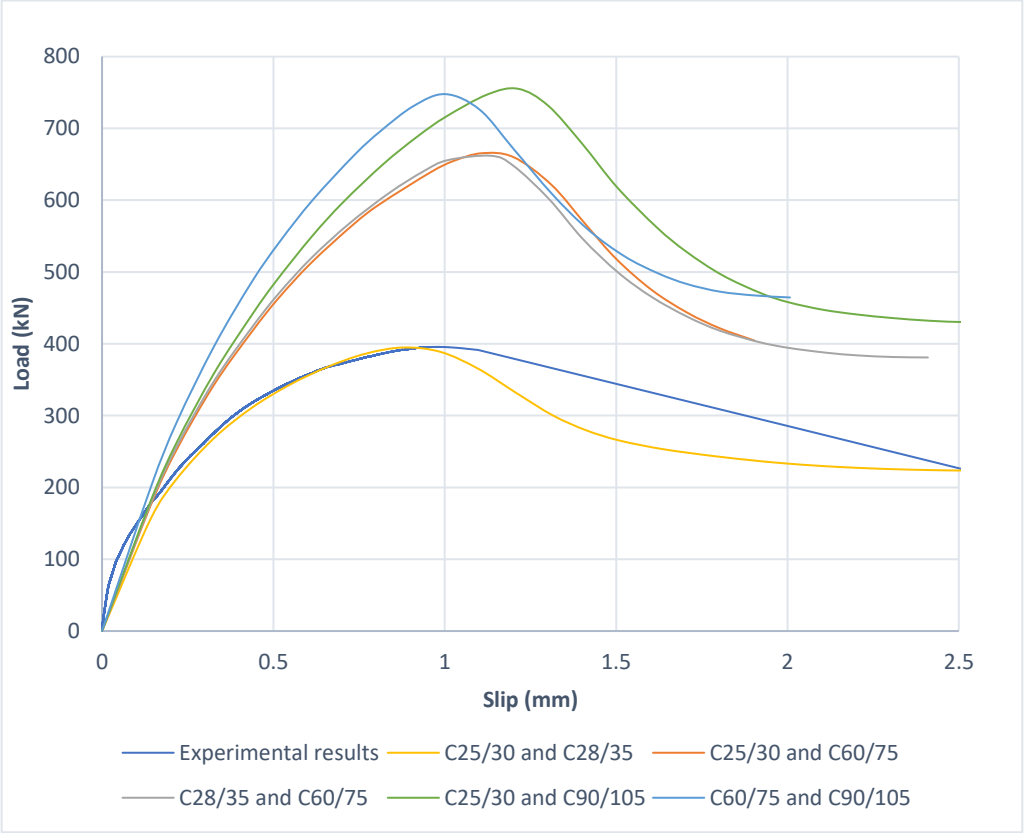

Graph 6-1 Load versus slip curves for all models

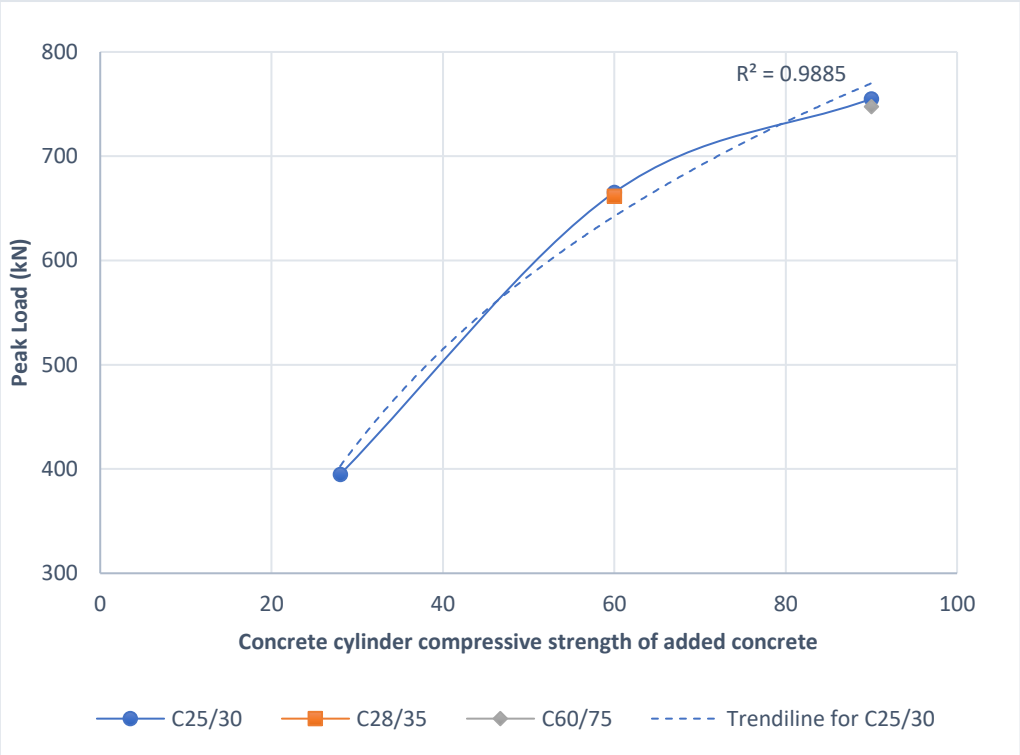

Graph 6-2 Peak load variation according to concrete strength

Observing the peak loads plot, it is visible that, keeping fixed the parameters of the existing concrete layer, the increase in strength class of the added concrete layer leads to a non-linear increase in the peak load. As already mentioned, even though the difference in the characteristic cylinder compressive strength between the first and second points and the second and third points are similar to each other in the C25/30 curve, it is visible that the peak load variation is significantly larger between the first and second points than between the second and third points, being the first variation approximately three times the second one. The trendline found to best fit the data has a logarithmic shape, being defined by Equation [8], but even though it is well-adjusted, with $R^2 = 0.9885$, the fit is visually not very satisfactory. In the equation, *x* represents the concrete cylinder compressive strength of added concrete

$$[8] \qquad Peak\ Load = 314.52 * ln(x) - 645.32$$

Additionally, comparing the peak loads obtained for models whose added concrete layer have the same strength class, it can be seen that the peak load variation occurring due to the variation of concrete strength class of the existing concrete layer is practically negligible, being a variation of the order of 1%. Therefore, one can conclude that the strength class of the concrete of lowest strength does not have considerable influence on the resulting peak load.

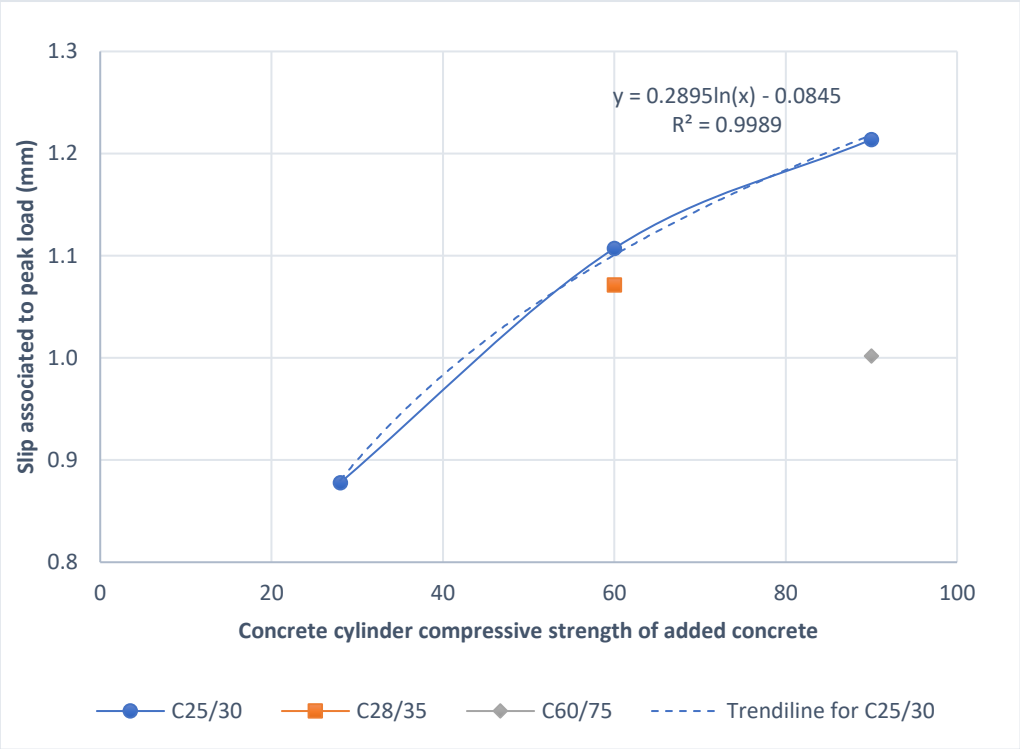

Graph 6-3 Slip value associated with the peak load, varying according to concrete strength

From the plot of the slip values associated to the peak load, it can be seen that the increase of strength class of the added concrete layer leads to increase of the slip value. A logarithmic trendline, defined by Equation [9], was created for this data, obtaining a nearly perfect adjustment, with $R^2 = 0.9989$. The variable *x* represents the concrete cylinder compressive strength of added concrete in the equation. However, the increase of strength class of the existing concrete layer has presented the opposite results, leading to a decrease in the slip associated to the peak load. As the peak load does not vary significantly from this increase while the slip value does, it can lead to the conclusion that the strength class of the existing concrete layer is influential for the ductility of the interface behaviour, being its increase associated to a decrease in ductility.

$$[9] \qquad Slip\ value = \ 0.2895 * ln(x) \ - \ 0.0845$$

The results presented above were summarized in Table 6-4, that is presented below.

Table 6-4 Summary of results for concrete strength analysis

	Concrete strength of top layer	Concrete strength of bottom layer	Peak Load [kN]	Displacement at Peak Load [mm]	Average Shear Strength [MPa]
Model I	C25/30	C28/35	394.81	0.878	3.95
Model II	C25/30	C60/75	665.29	1.107	6.65
Model III	C28/35	C60/75	661.81	1.072	6.62
Model IV	C25/30	C90/105	755.07	1.214	7.55
Model V	C60/75	C90/105	747.62	1.002	7.48

6.3. Comparison of Displacements Distributions

By observing Figure 6-1 to Figure 6-5, one can see that the distribution of displacements is affected by the change in the strength classes of the concrete layers. It can be seen that, in XY plane, the displacement field in the bottom concrete layer is very similar for Models II to V, while Model I presents a larger portion of the layer with practically null displacements (dark blue region in the figures). In the top concrete layer, for Model I the displacement field is practically constant, while for the other models the larger displacement values are concentrated at the bottom of the left side (the side of application of displacement) and at the top of the right side. It also can be observed that the portion of the top layer with the largest displacement value increases as the ratio between concrete strengths of both layers decreases, being the smallest portion present in Model IV, in which it can also be observed that the smallest displacements of this layer are concentrated at the bottom of the right side and at the interface with the bottom layer.

In the YZ plane, one can observe that the symmetry with respect to y axis is maintained in all models and the shape of the distribution is also similar in all of them. That is expected considering that in all models there is symmetry of the specimen, both concerning geometry and materials, and of the applied displacement with respect to y axis in this plane.

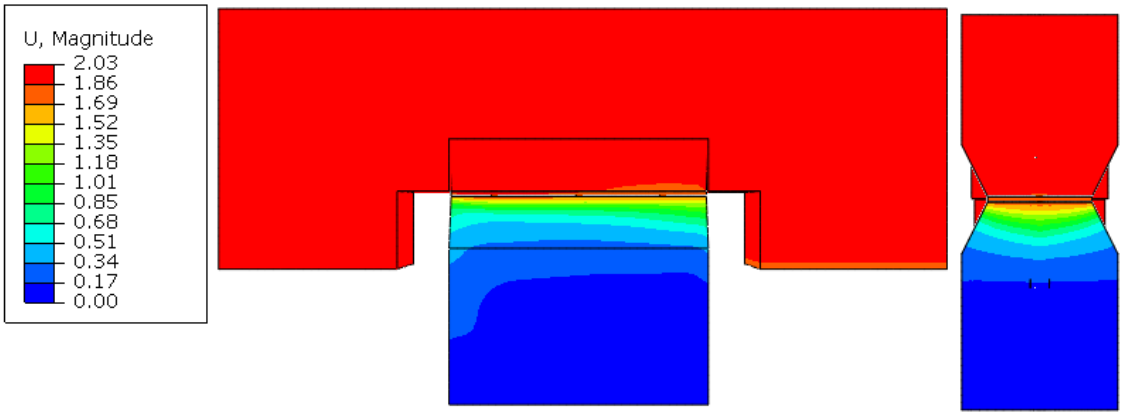

Figure 6-1 Distribution of Displacements in Model I (Bottom C28/35-Top C25/30) [mm]

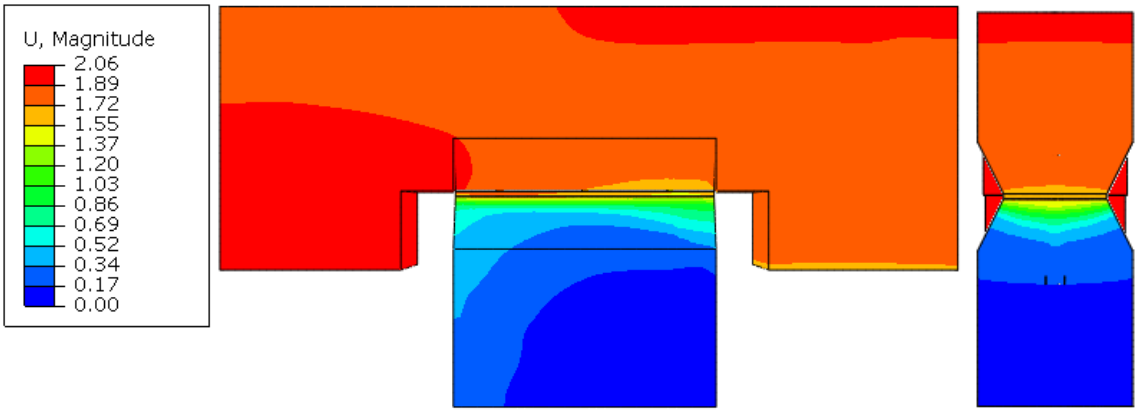

Figure 6-2 Distribution of Displacements in Model II (Bottom C60/75-Top C25/30) [mm]

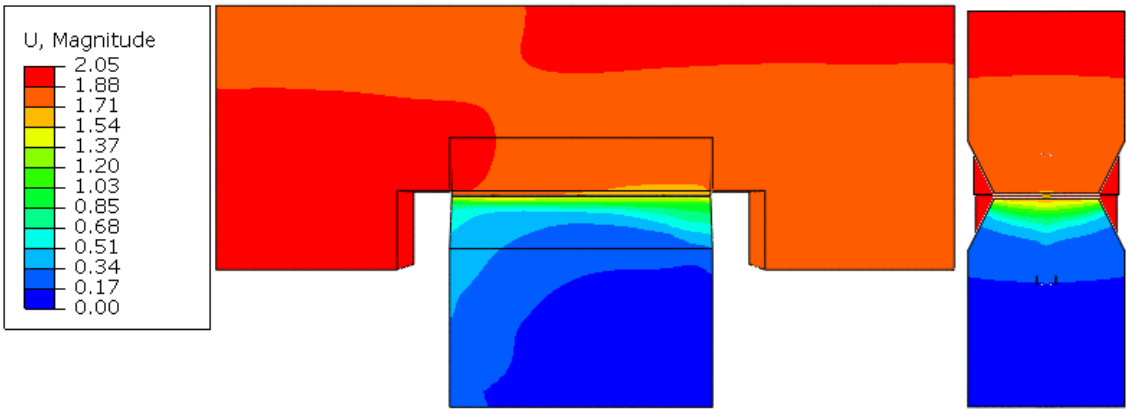

Figure 6-3 Distribution of Displacements in Model III (Bottom C28/35-Top C28/35) [mm]

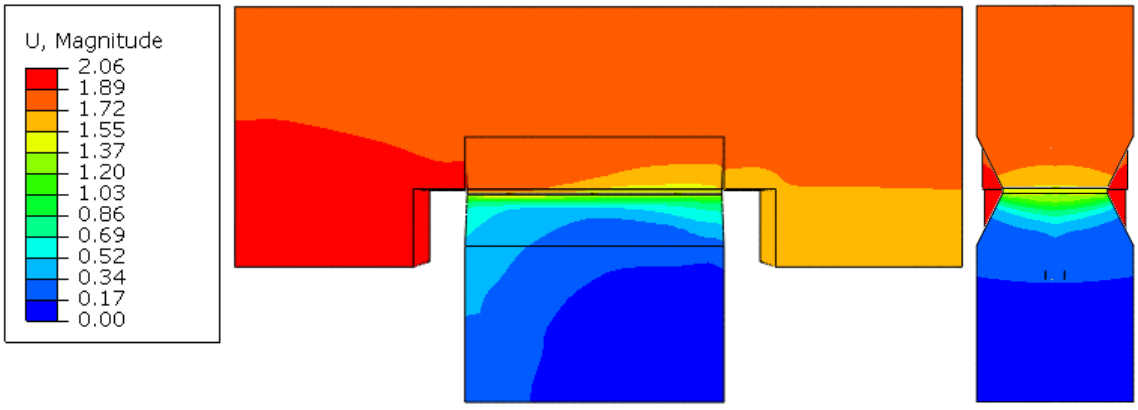

Figure 6-4 Distribution of Displacements in Model IV (Bottom C90/105-Top C25/30) [mm]

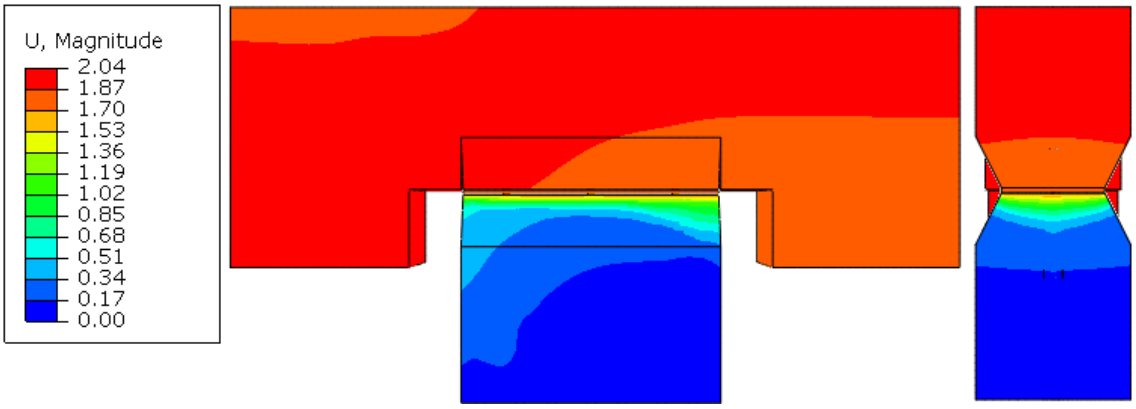

Figure 6-5 Distribution of Displacements in Model V (Bottom C90/105-Top C60/75) [mm]

6.4. Comparison of Damage Distributions

As already mentioned, the distributions of compressive and tensile damages obtained in the simulations represent, respectively, the crushing pattern and the cracking pattern of the specimens.

Observing Figure 6-6 to Figure 6-10, one can notice that the crushing pattern both at the exterior and the interior of the specimen do not present significant changes as the strength class of the concrete layers is modified. In Model II and specially in Model V, that have respectively the second and first highest ratios between the concrete strengths of both layers, damage can be seen also at the top concrete layer, something that does not occur in the other models.

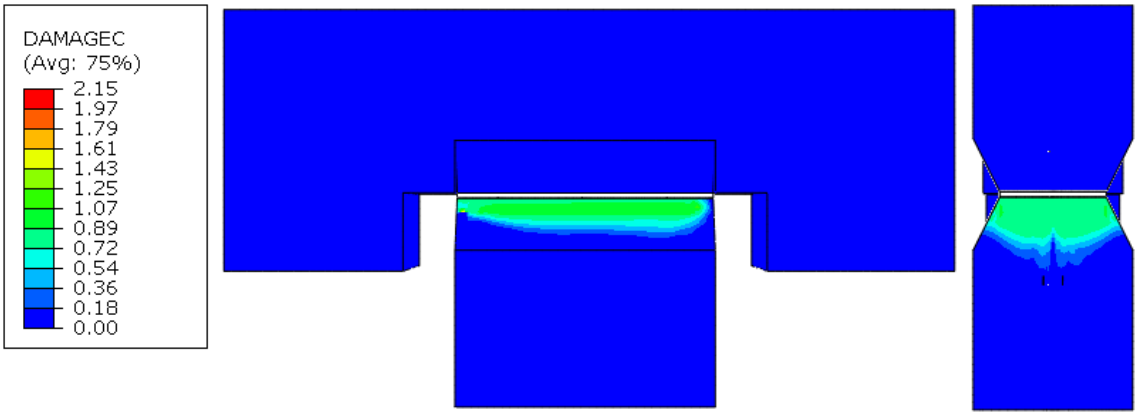

Figure 6-6 Distribution of Compressive Damage in Model I (Bottom C28/35-Top C25/30)

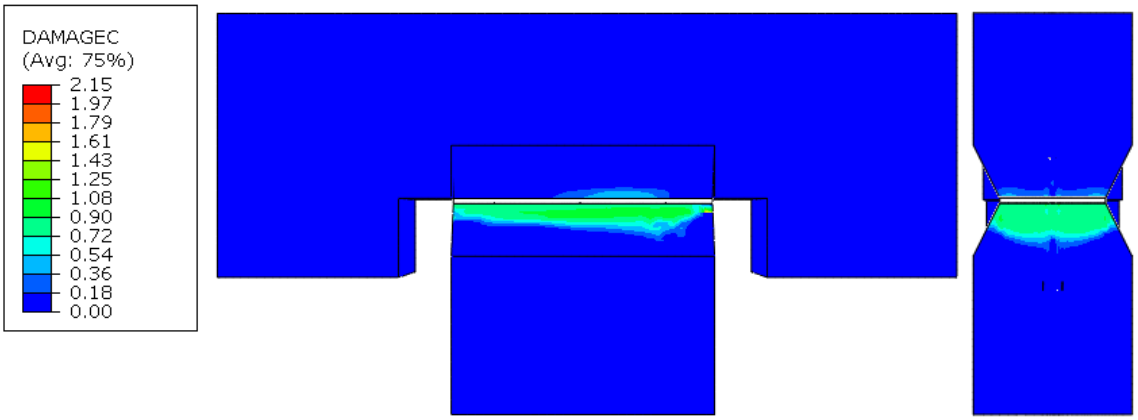

Figure 6-7 Distribution of Compressive Damage in Model II (Bottom C60/75-Top C25/30)

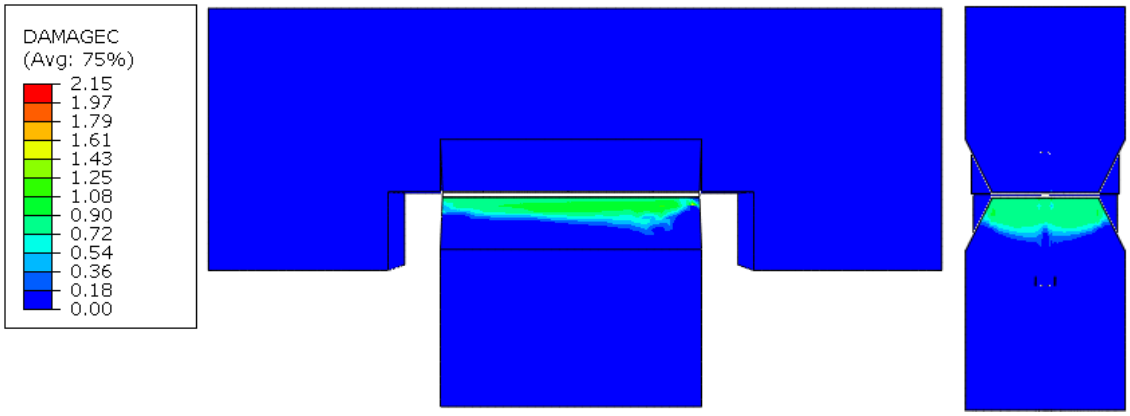

Figure 6-8 Distribution of Compressive Damage in Model III (Bottom C28/35-Top C28/35)

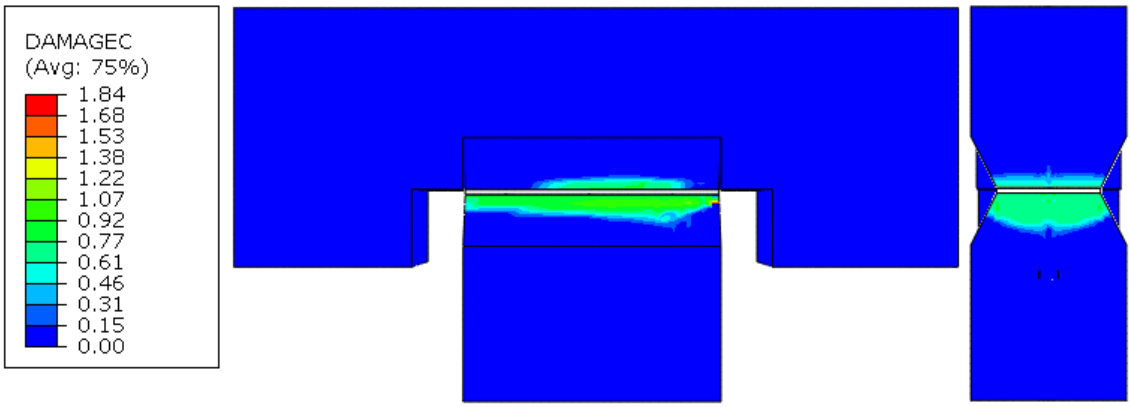

Figure 6-9 Distribution of Compressive Damage in Model IV (Bottom C90/105-Top C25/30)

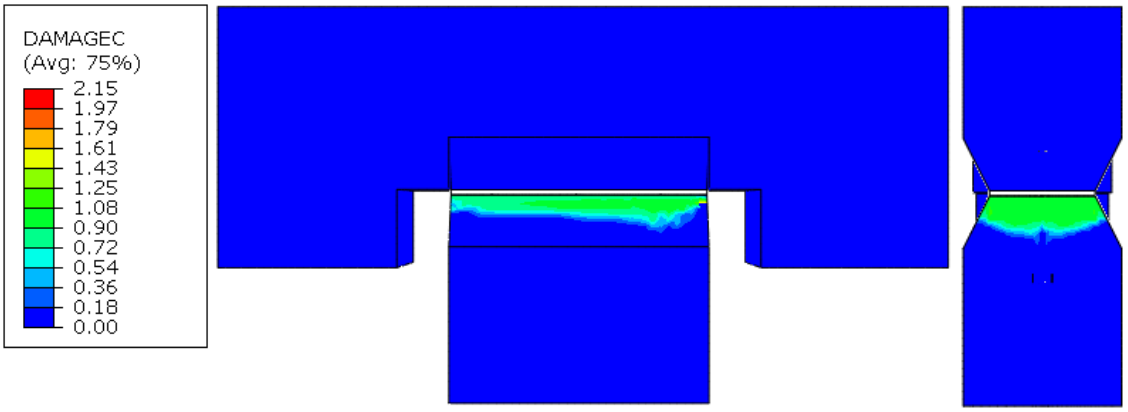

Figure 6-10 Distribution of Compressive Damage in Model V

Regarding the cracking pattern, which can be observed in Figure 6-11 to Figure 6-15, it can be observed that the shape of the pattern does not change significantly from one model to another, as all of them have larger cracked portions around the right part of interface region, at the bottom layer, and around the left part of the middle of the bottom layer. However, the magnitude of the damage changes, as can be evaluated by the colour of the patterns in each model, as they are all in the same scale. Model I presents the lowest magnitudes of damage, while Model V presents the highest magnitudes, which leads to the conclusion that the obtained magnitude of damage increases as the concrete strengths increase. The other three models have similar magnitudes of damage between each other, with intermediate values between the ones of Models I and V.

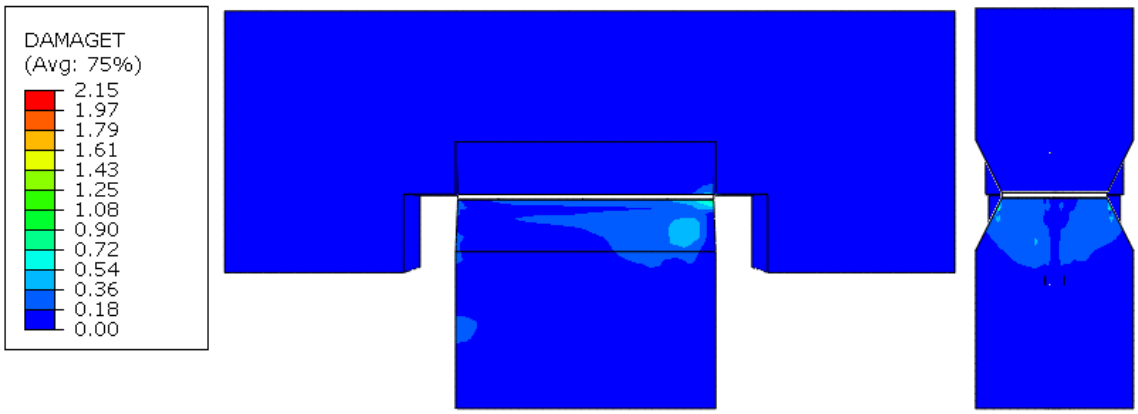

Figure 6-11 Distribution of Tensile Damage in Model I (Bottom C28/35-Top C25/30)

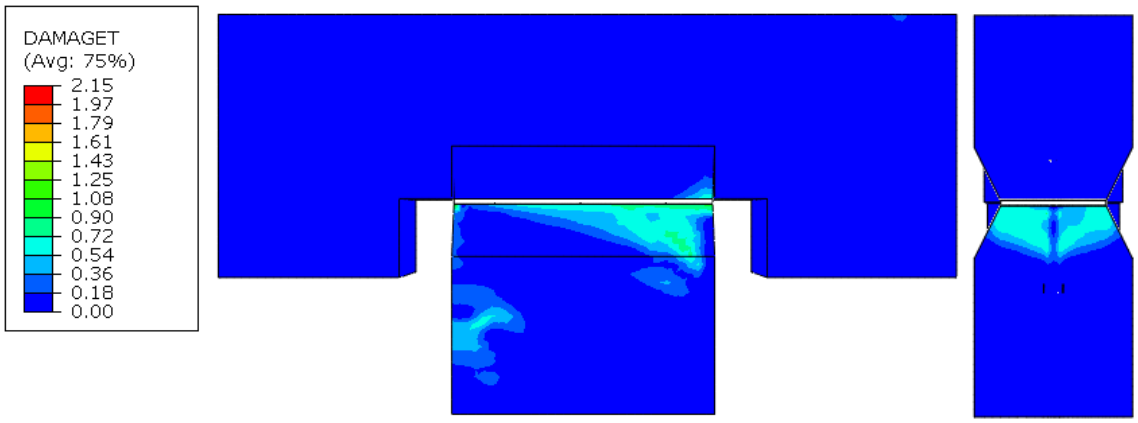

Figure 6-12 Distribution of Tensile Damage in Model II (Bottom C60/75-Top C25/30)

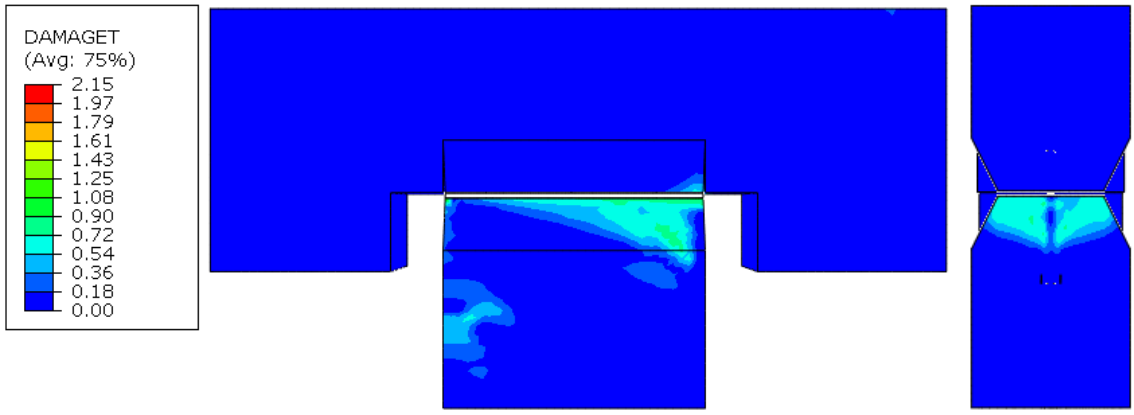

Figure 6-13 Distribution of Tensile Damage in Model III (Bottom C28/35-Top C28/35)

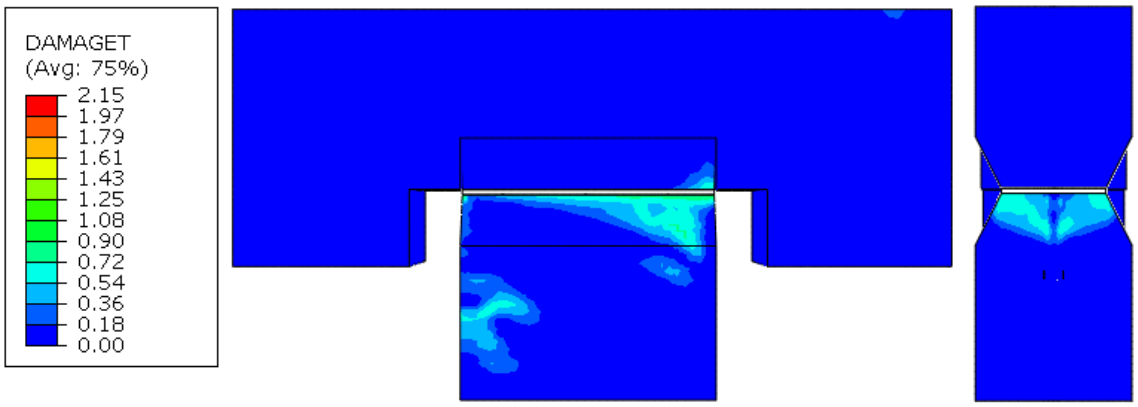

Figure 6-14 Distribution of Tensile Damage in Model IV (Bottom C90/105-Top C25/30)

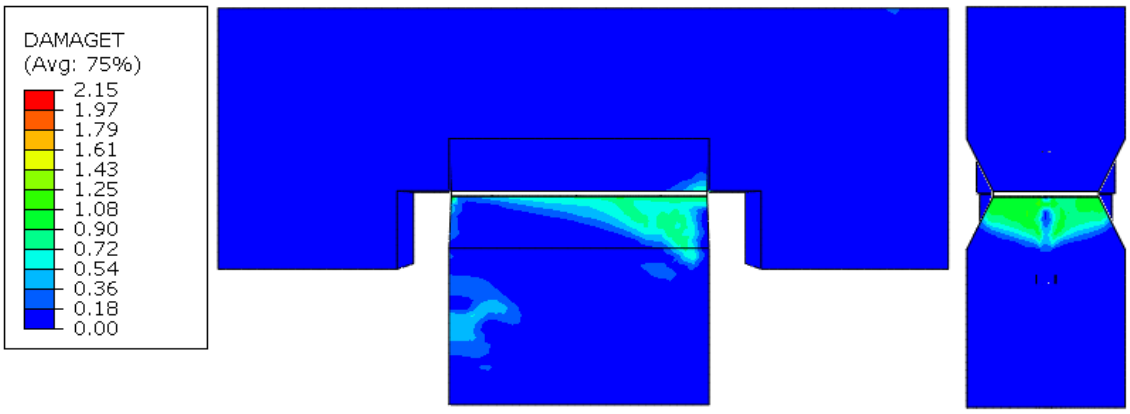

Figure 6-15 Distribution of Tensile Damage in Model V (Bottom C90/105-Top C60/75)

6.5. Comparison of Shear Stresses Distributions along the Interface

In this section, the shear stress along the interface will be presented for each model considering, in each one, two sections defining paths along the x axis, as previously presented and illustrated in Figure 5-12. All stresses presented were extracted from the top of the interface layer, where it is in contact with the concrete of lowest strength and for slips of 2 mm.

In Graph 6-4, Graph 6-6, Graph 6-8, Graph 6-10 and Graph 6-12, that contain the shear stresses along path a) in each model, the anchorage bars were included in the corresponding positions with its Von-Mises stresses represented by colours, in accordance with the scale presented in Figure 6-16. It is noticeable that in all models the higher values of shear stress occur close to the initial section of the interface, that is, the section closest to point of application of displacement, then they decrease along the interface, except for peaks that occur around the anchorage bars. Model I present the lowest values of peak shear stress, while Models IV and V have the highest values, that are very similar between these two models. Models II and III also have very similar shear peak values between each other.

In Graph 6-5, Graph 6-7, Graph 6-9, Graph 6-11 and Graph 6-13 the shear stresses along path b) are presented. It can be observed in them that the higher shear stresses occur at the beginning of the contact surface, in other words the section closest to the point of application of displacement, and then decrease along the x direction, presenting a peak at the level of the section of the third anchor. Observations concerning the magnitude of the shear stresses are the same as the ones made for path a).

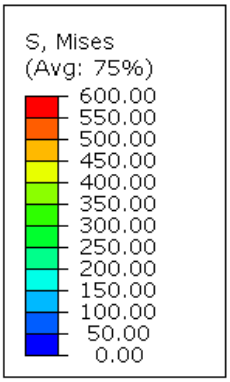

Figure 6-16 Scale of stresses used for the representation of the anchorage bars

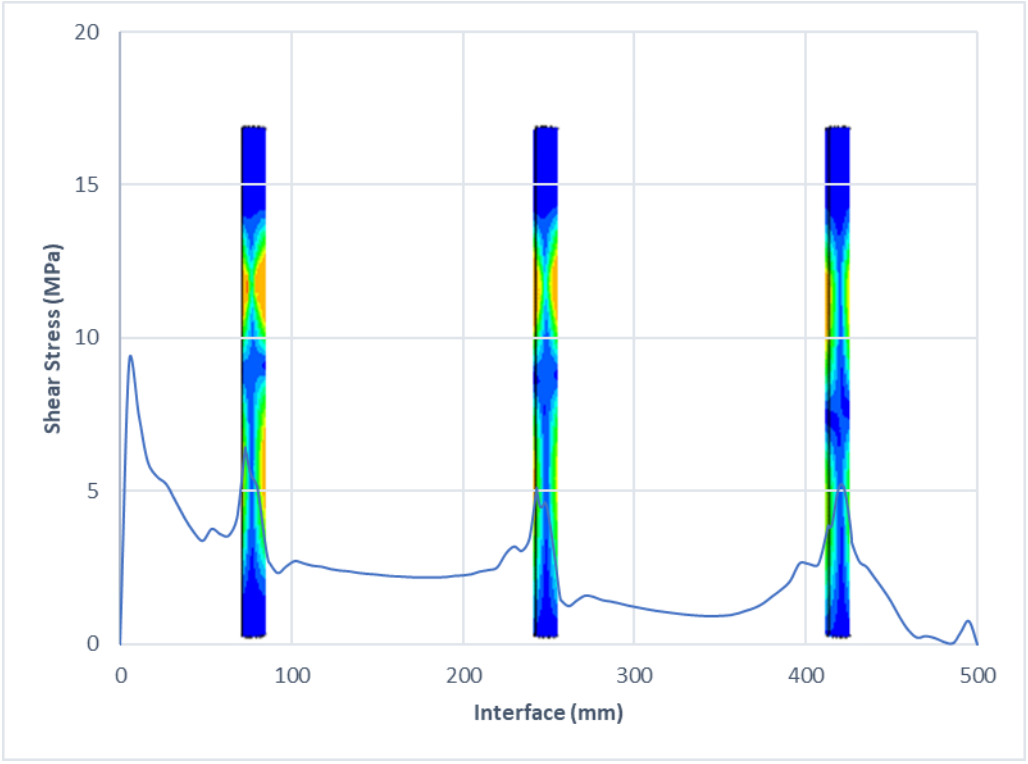

Graph 6-4 Shear stress along path a) in Model I (Bottom C28/35-Top C25/30)

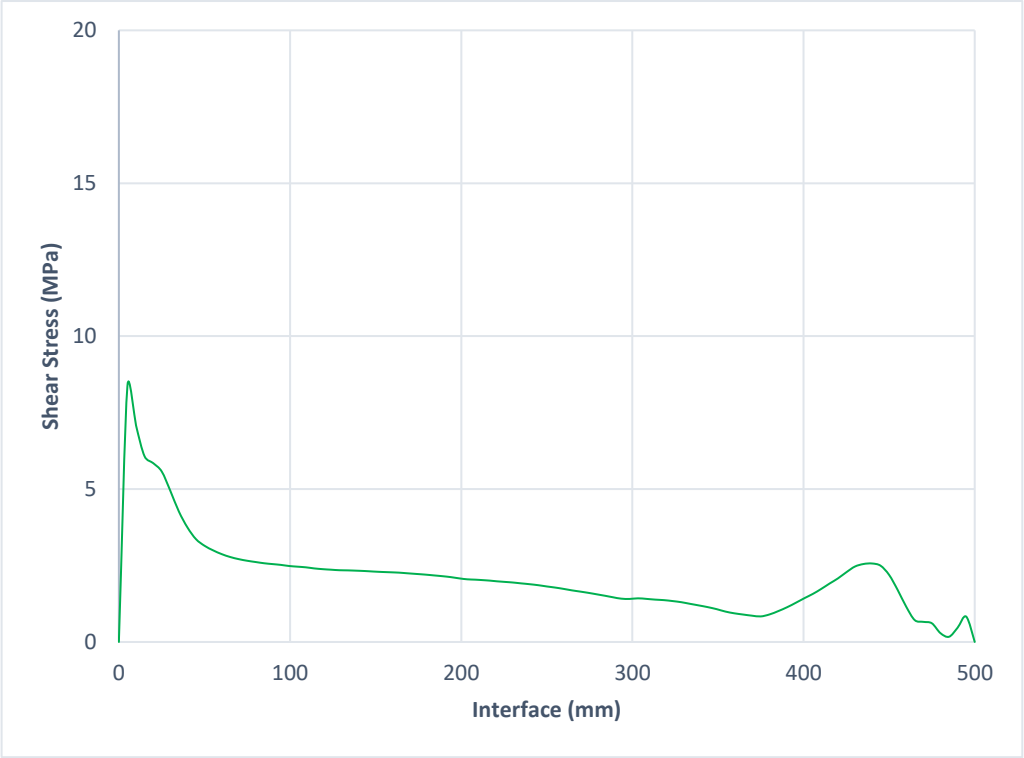

Graph 6-5 Shear stress along path b) in Model I (Bottom C28/35-Top C25/30)

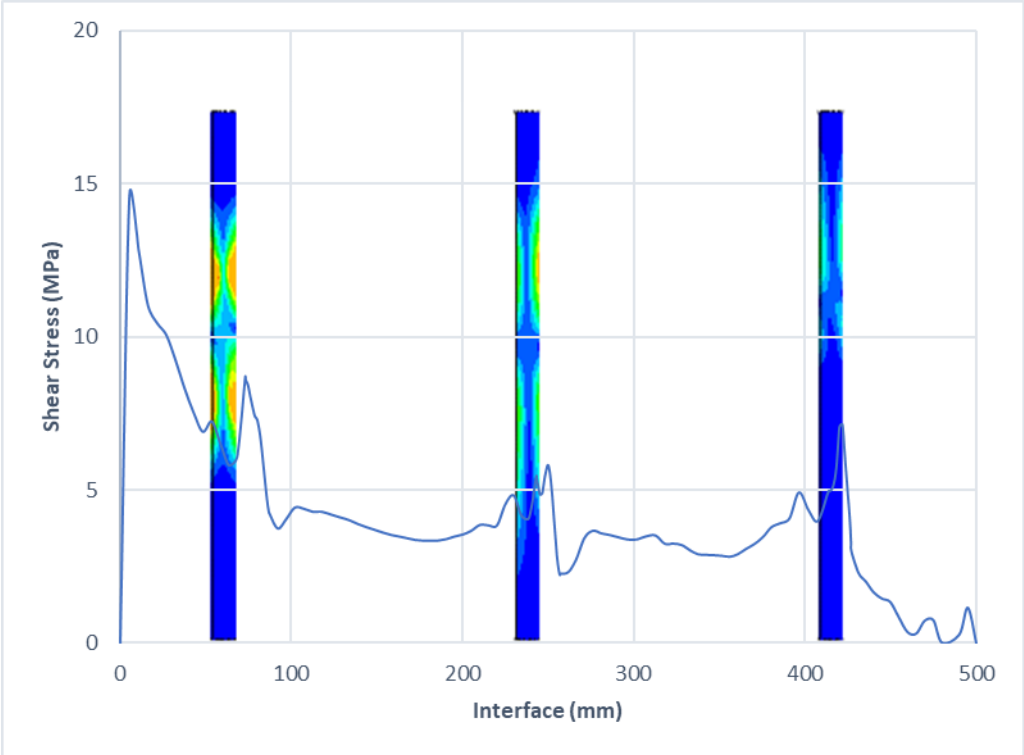

Graph 6-6 Shear stress along path a) in Model II (Bottom C60/75-Top C25/30)

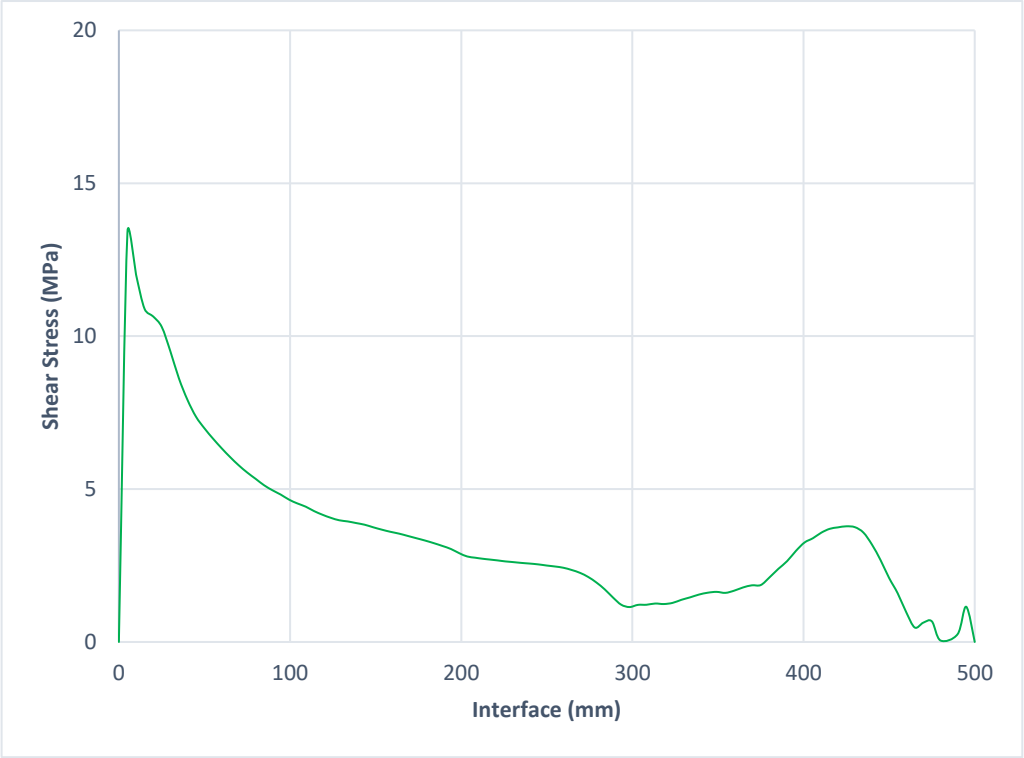

Graph 6-7 Shear stress along path b) in Model II (Bottom C60/75-Top C25/30)

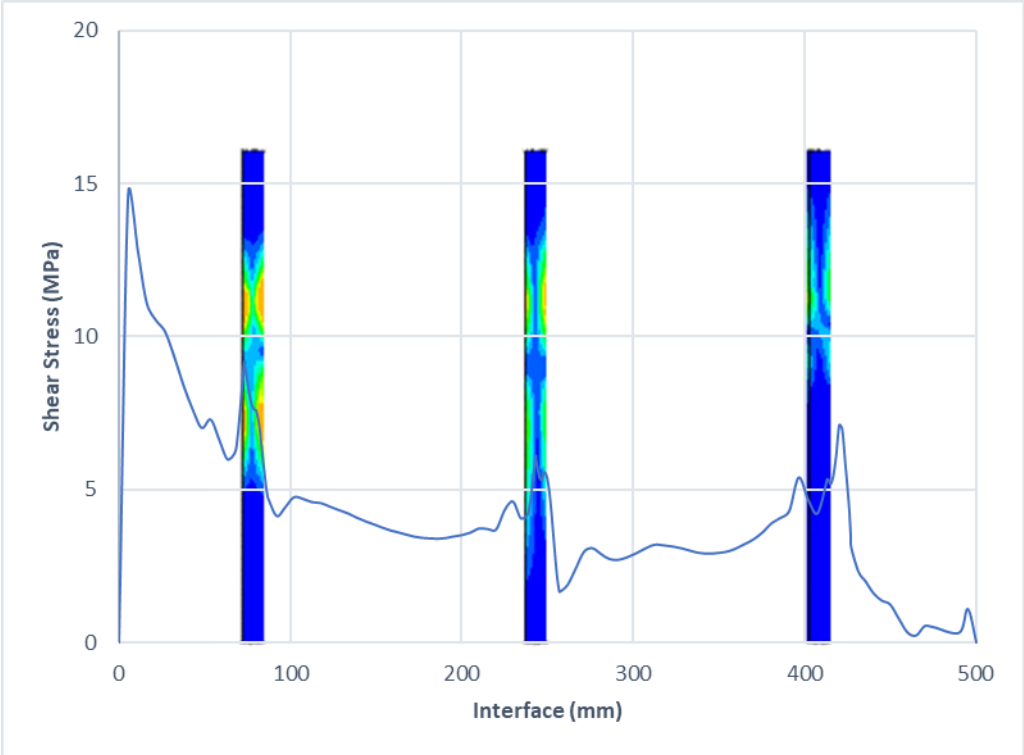

Graph 6-8 Shear stress along path a) in Model III (Bottom C28/35-Top C28/35)

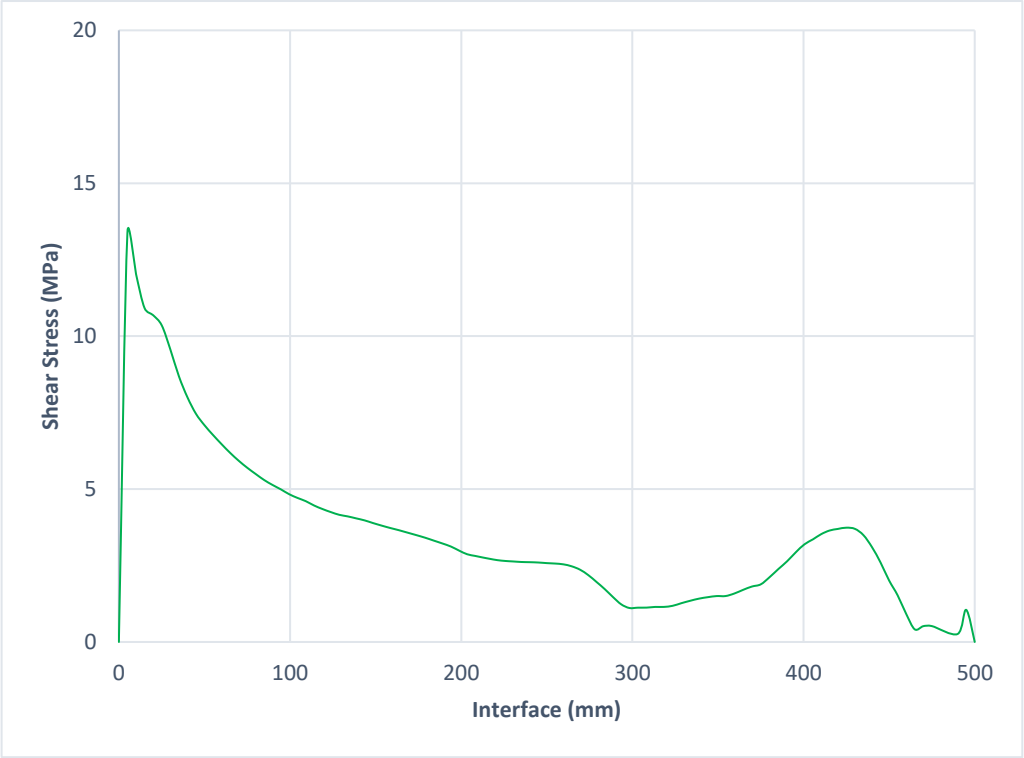

Graph 6-9 Shear stress along path b) in Model III (Bottom C28/35-Top C28/35)

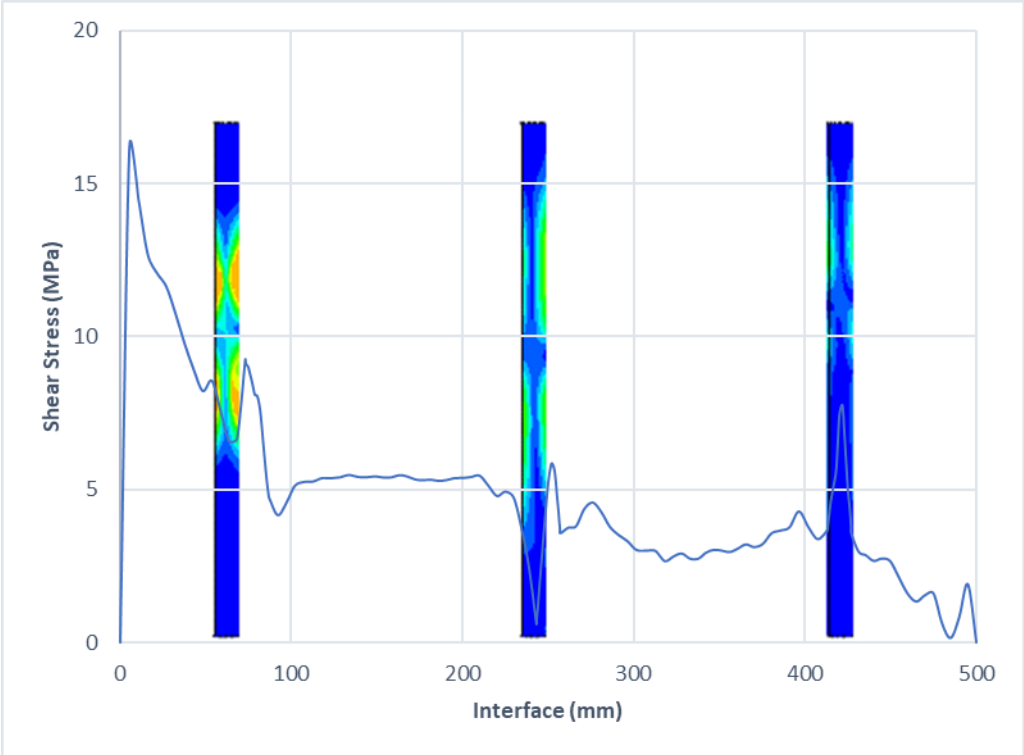

Graph 6-10 Shear stress along path a) in Model IV (Bottom C90/105-Top C25/30)

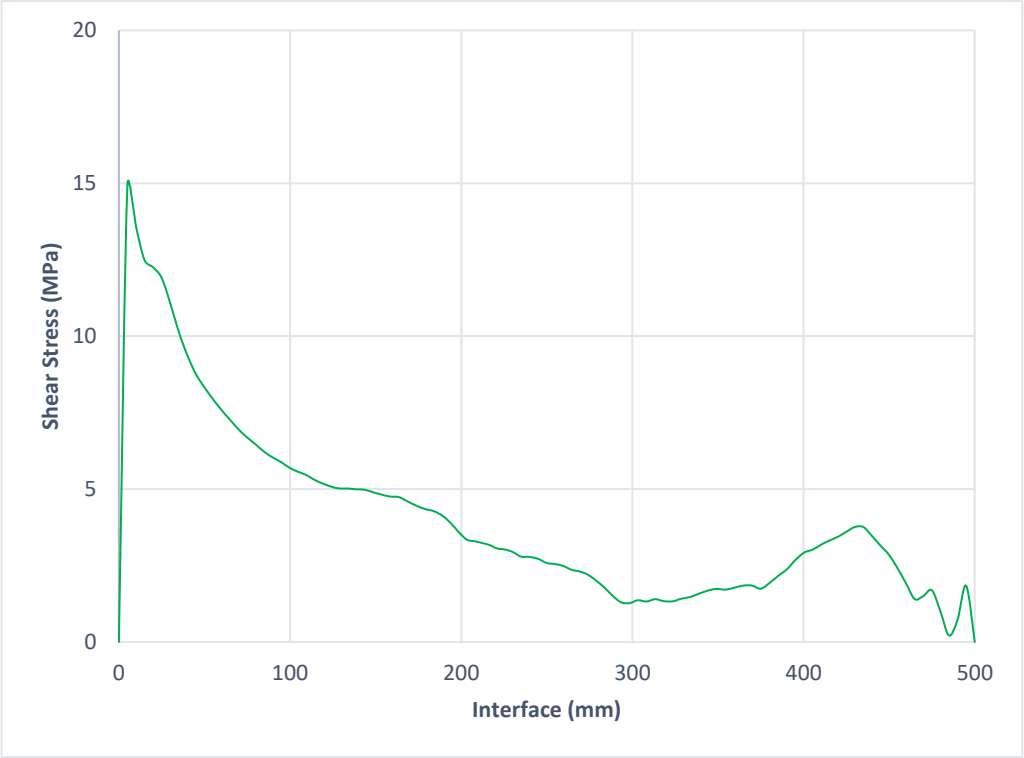

Graph 6-11 Shear stress along path b) in Model IV (Bottom C90/105-Top C25/30)

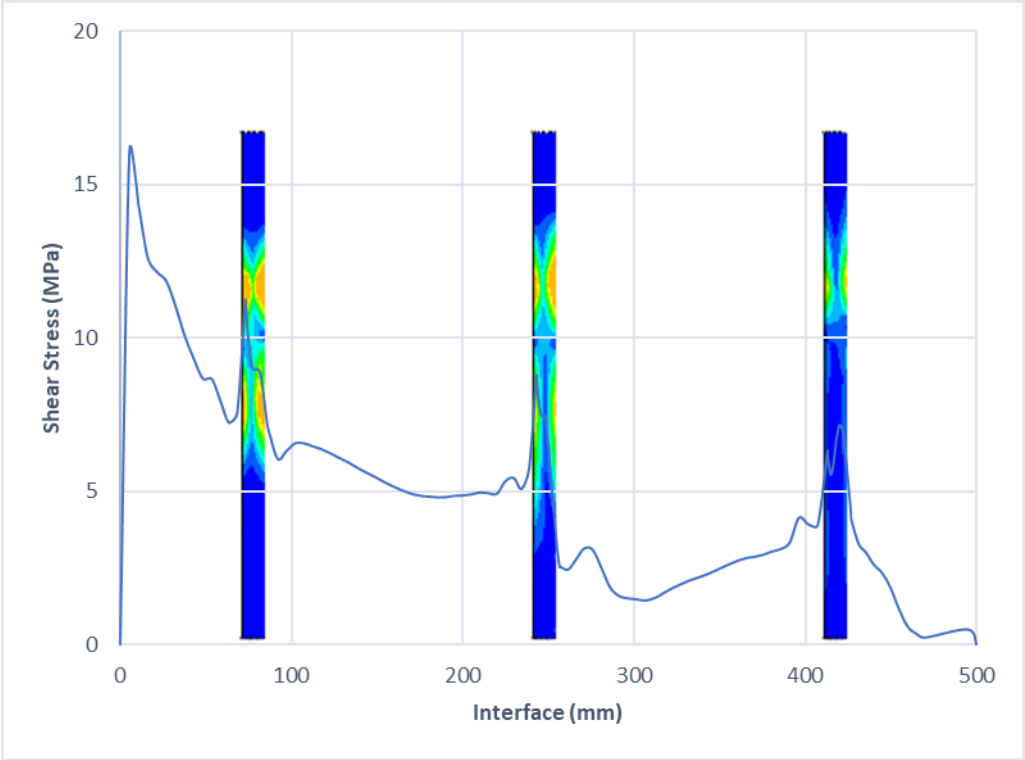

Graph 6-12 Shear stress along path a) in Model V (Bottom C90/105-Top C60/75)

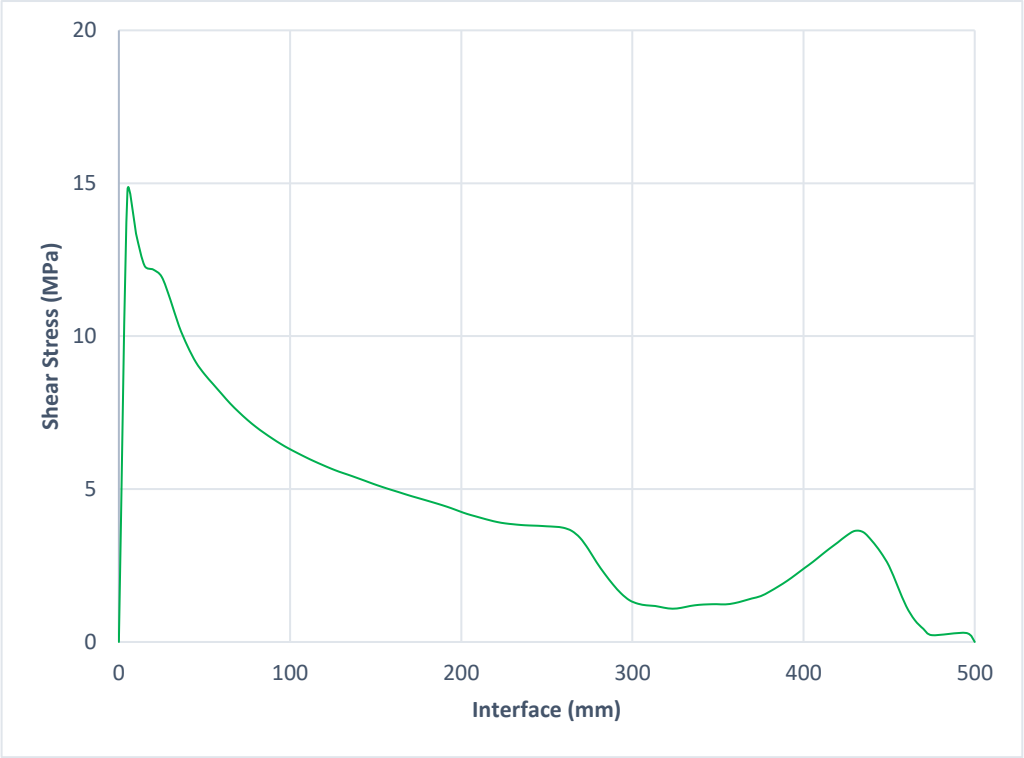

Graph 6-13 Shear stress along path b) in Model V (Bottom C90/105-Top C60/75)

6.6. Comparison of Principal Stresses Distributions

The principal maximum and minimum stresses in the anchors of each model, presented in their deformed configuration, are presented in this section, in Figure 6-17 to Figure 6-21. It is noticeable that in Model I the anchorage bars present similar deformations and stresses between each other, while in Models II to V the deformation decreases significantly from the first anchor (the one at the left) to the third one, that deforms mostly at the top part, while being mostly straight at the bottom section. The distribution of stresses is in accordance with the deformations, that is to say that the deformed sections concentrate the higher stresses, while the rest of the anchor presents very small stress values.

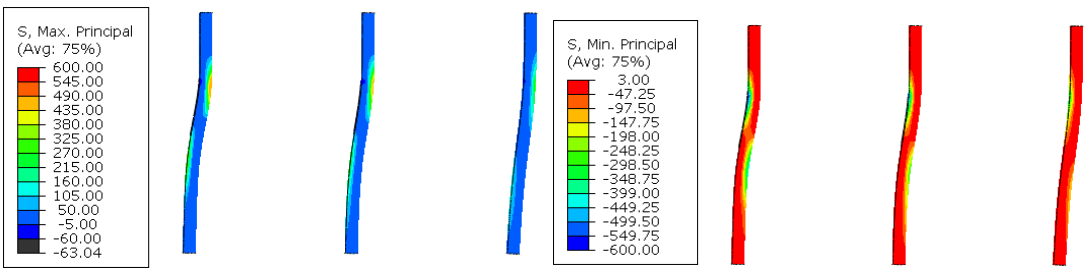

Figure 6-17 Maximum and minimal principal stresses in Model I's anchors (Bottom C28/35-Top C25/30)

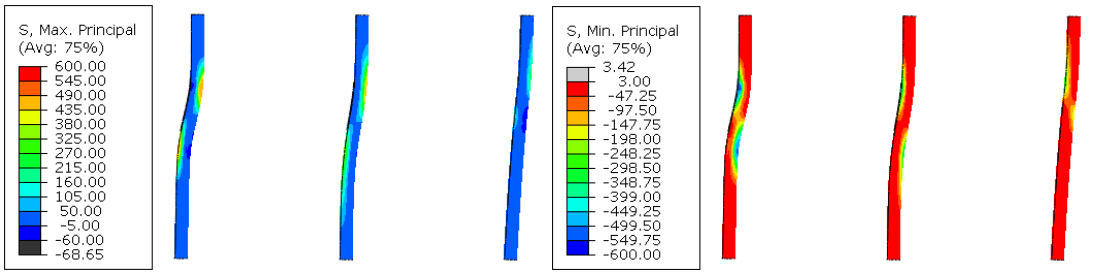

Figure 6-18 Maximum and minimal principal stresses in Model II's anchors (Bottom C60/75-Top C25/30)

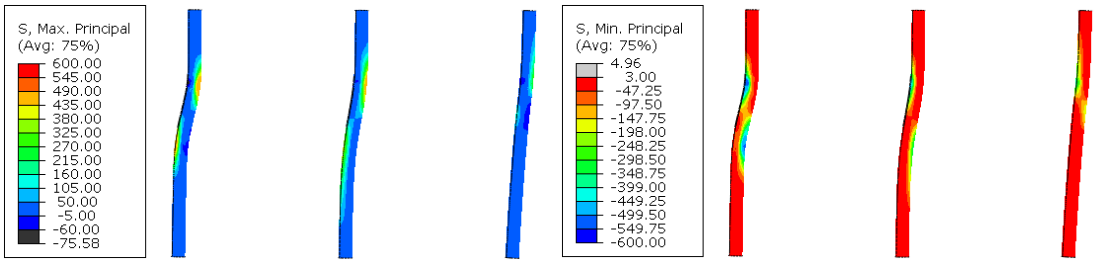

Figure 6-19 Maximum and minimal principal stresses in Model III's anchors (Bottom C28/35-Top C28/35)

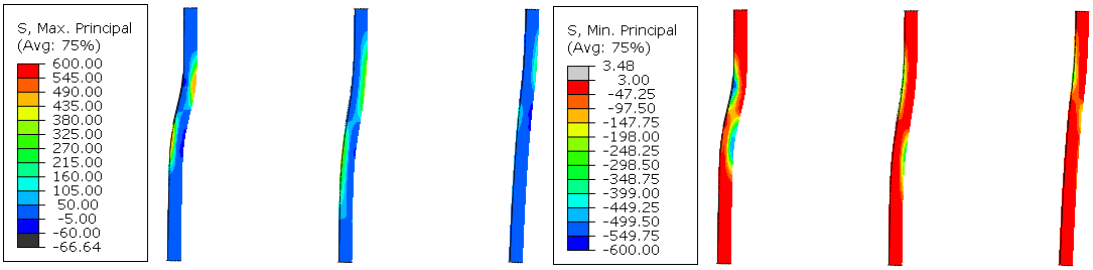

Figure 6-20 Maximum and minimal principal stresses in Model IV's anchors (Bottom C90/105-Top C25/30)

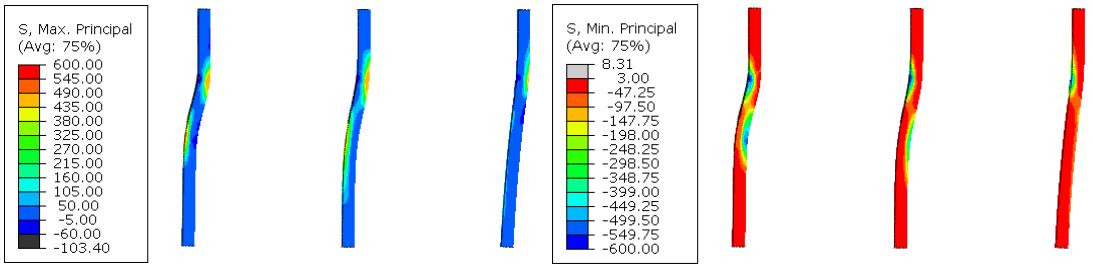

Figure 6-21 Maximum and minimal principal stresses in Model V's anchor (Bottom C90/105-Top C60/75)

In Figure 6-22 to Figure 6-26, the minimal principal stresses can be observed in the concrete parts of the five models, which are presented in their deformed configurations. One can observe that the distribution of minimal principal stresses overall is of similar shape for all models studied, being the stresses of highest magnitude in absolute values concentrated at the left side of the top concrete layer, that is where the application of the displacement occurs, at the points where the condition of orthogonality restraint is

imposed (Reference Points 2 and 3) and at the left of the interface. For the bottom concrete layer, stresses concentrate at the right side, near the point of imposition of restraints for this layer (Reference Point 5).

It can be seen that the Models IV and V present greater regions of higher stresses (represented by blue colours in the figures below), while Model I presents the smallest high stress regions. The increase of high stress regions occurs for both concrete layers, that is to say that, for instance, comparing Model I to Model IV, that have concretes of same strength class in the top layer, it can be seen that the stress distribution at this layer differs between the models, showing that a change in strength class for the bottom concrete layer affects the stress distribution at the top one.

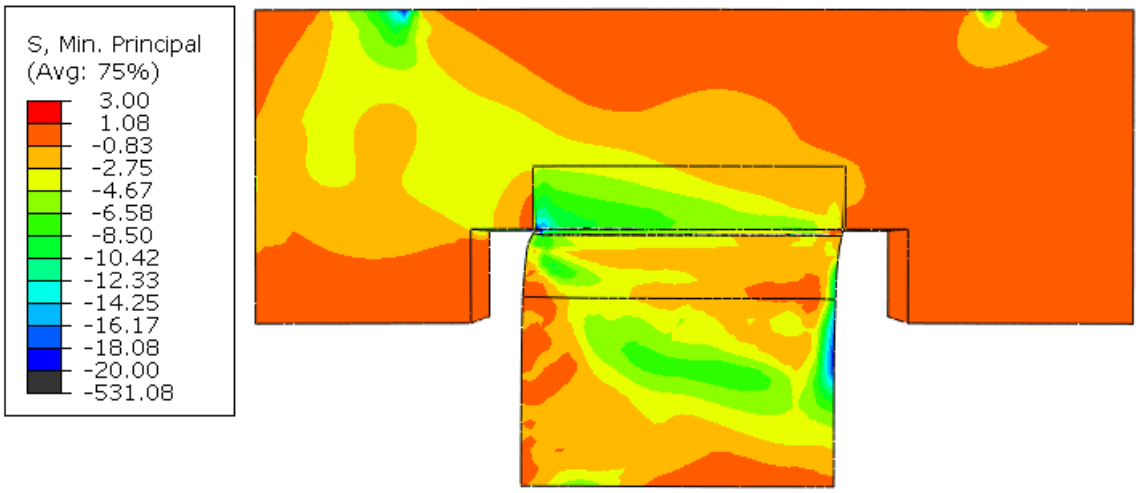

Figure 6-22 Minimal principal stresses in Model I (Bottom C28/35-Top C25/30)

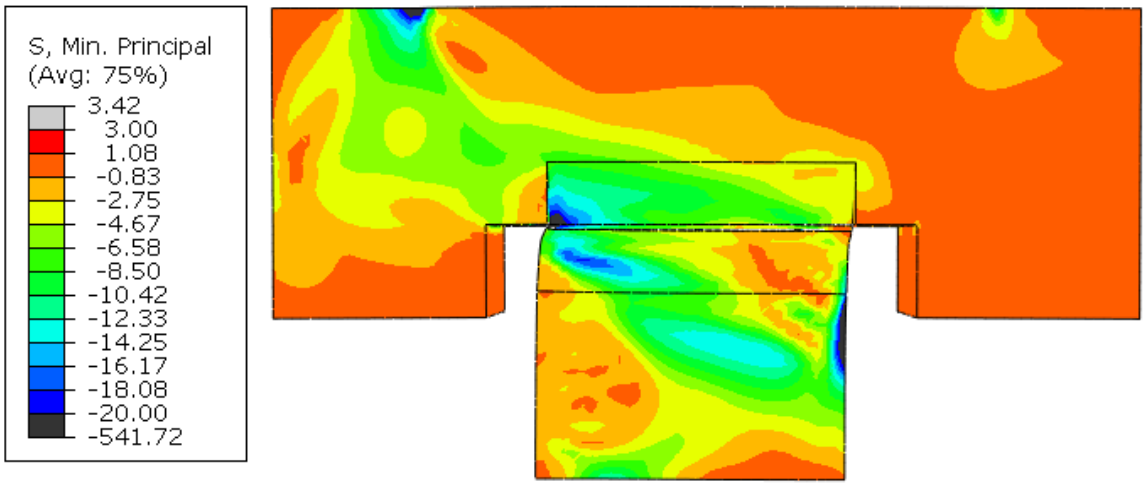

Figure 6-23 Minimal principal stresses in Model II (Bottom C60/75-Top C25/30)

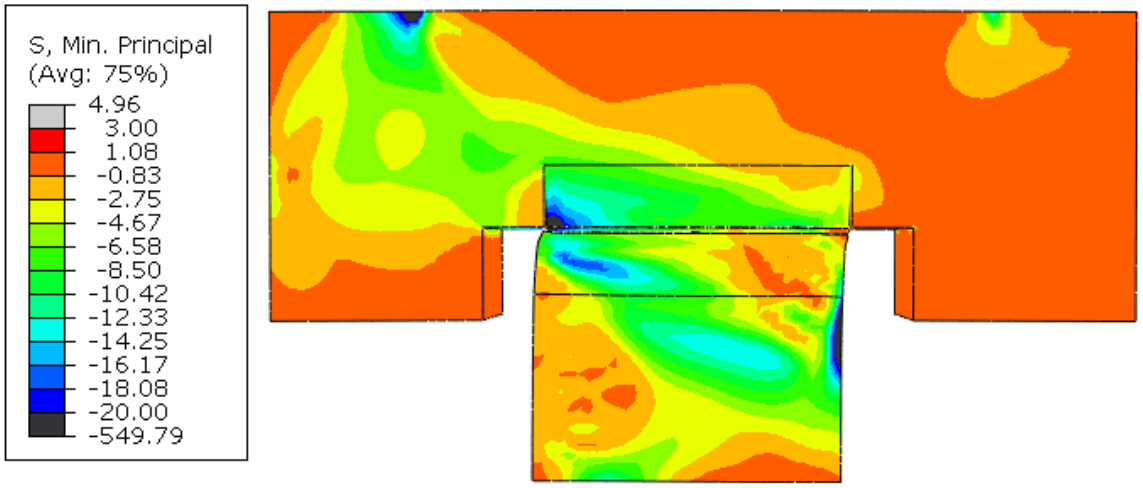

Figure 6-24 Minimal principal stresses in Model III (Bottom C28/35-Top C28/35)

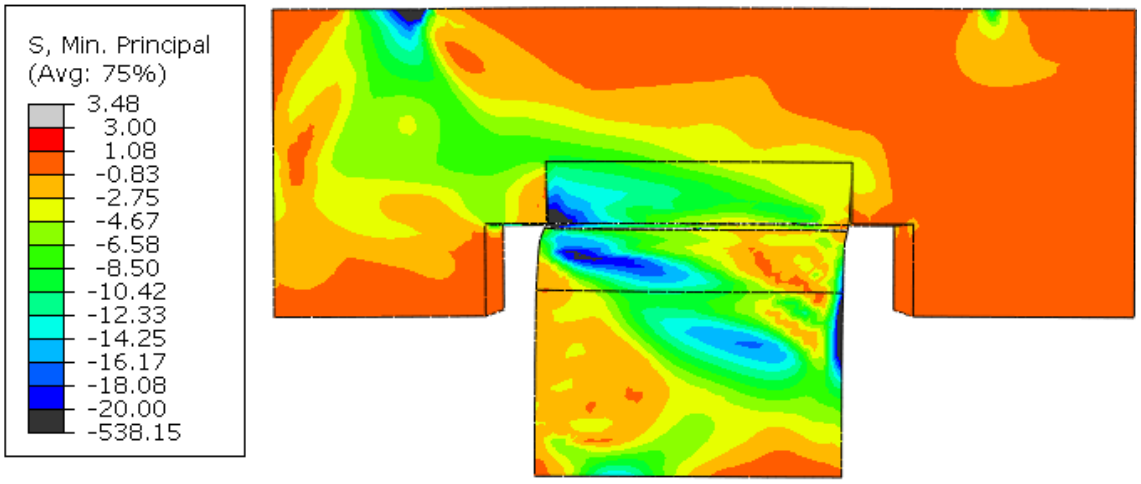

Figure 6-25 Minimal principal stresses in Model IV (Bottom C90/105-Top C25/30)

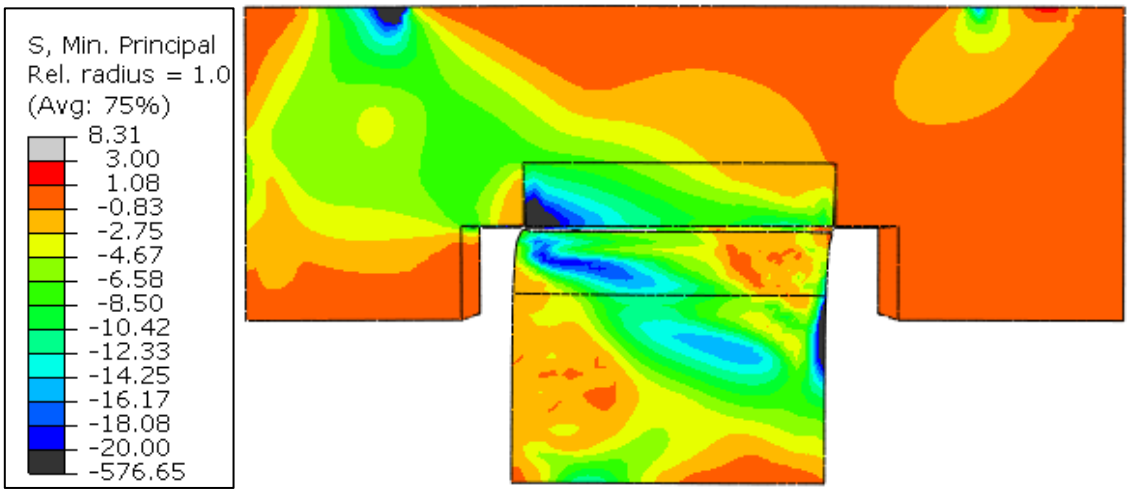

Figure 6-26 Minimal principal stresses in Model V (Bottom C90/105-Top C60/75)

Conclusion

The conclusions drawn throughout the development of the research study presented in this thesis are summarised in this final chapter. Specifically, conclusions were drawn in Chapters 4, 5 and 6, and therefore refer to one of these three topics:

- Influence of input parameters introduced in a Concrete Damaged Plasticity model created in Abaqus on the computational cost of the analysis and the results obtained;
- Effect of the specimen's size on the behaviour of concrete-to-concrete interfaces subjected to shear, concerning load *versus* slip curves, displacement distributions, crushing and cracking patterns and stresses distributions;
- Influence of the concrete strength on the interface between reinforced concrete layers under shear action, concerning load *versus* slip curves, displacement distributions, crushing and cracking patterns and stresses distributions.

Regarding the first topic, it was possible to conclude that the viscosity parameter has considerable influence on the magnitude of the load obtained and on the computational cost of the analysis. It was found that introducing lower values of the viscosity parameter on specifications of the added layer, that has the highest concrete strength, an almost linear decrease in the peak load is obtained. Additionally, an increase in the computational cost is also obtained. The viscosity parameter of the concrete of the existing layer, namely the lowest strength concrete, was found to have negligible influence on the peak load, but a noticeable influence on the computational cost, decreasing it when it is set to higher values than the one of the added concrete layer. However, when the viscosity parameter of the existing concrete layer is set to a lower value than the one of the added concrete, a distortion in the shape of the load *versus* slip curve occurs. Additionally, the introduction of very small values of viscosity parameters for both concrete layers also produced distortions in the shape of the curve, proving the importance of the viscoplastic regularization for this model.

It was also found that the dilation angle influences the peak load obtained and the computational cost of the simulation. Its value has also shown an almost linear direct relation with the peak load, however with less sensibility than the one obtained for variations in the viscosity parameter. The value introduced for the concrete of highest strength has been proven to be more influential to the peak load than the one introduced for the other concrete layer, as occurred for the viscosity parameter. Introducing a higher

dilation angle for the existing concrete layer than the one introduced for the added concrete layer, there is a negligible change in the peak load, while an increase in the computational cost occurs. In the opposite direction, that is to say, introducing a lower dilation angle for the existing concrete layer, a small but considerable decrease in the peak load occurs.

Models with different dilation angles and viscosity parameters that have resulted in similar peak loads it was found that the model with lowest viscosity parameter value tends to have the highest final load. The eccentricity and the ratio between biaxial and uniaxial compression strengths (f_{b0}/f_{c0}) were found to have negligible influence on the load results.

The concrete uniaxial tensile strength, which is a defining parameter for the tensile damage curve, has presented a direct relation with the peak load. It has also presented an influence in the relationship between the value of the peak load and the value of the corresponding slip, in such a way that for a fixed peak load value, higher values of concrete uniaxial tensile strength can be related to lower slip values associated with the peak. The fracture energy, that also influences on the tensile damage curve, has also led to negligible variation on the results (probably due to the limited variation in the considered range).

Regarding the second topic, the decrease in the size of the specimen was found to be associated with decrease in the peak load and increase in ductility. Evaluating the peak load variation according to the contact area between the concrete layers, a direct non-linear relation could be observed. Concerning the maximum shear stress between the concrete layers, its variation according to the contact area was evaluated. It was found that the increase in the contact area can be associated in an approximately linear trend with a decrease in the maximum shear stress.

The size of the specimens was also found to affect the shape of the displacements field, even though the region of lowest displacement does not change. The portion of the specimen with negligible displacements decrease in proportion to the total volume as the size of the specimen decreases. Additionally, the symmetry of the field in the YZ plane with respect to the y axis is maintained regardless of the size of the specimen.

The crushing pattern did not present significant changes as the size of the specimen changed, only presenting an increase in the proportional penetration at the interior of the specimen as its size decreased, specially under the extremities of the contact area. The cracking pattern presented similar changes, with small changes at the exterior of the

specimen, and, at its interior, presenting an increase in the proportional penetration, more significant under the interface's extremities.

The shear stresses distribution along the interface presents some changes with the variation of the specimen's size. As the size decreased, the shear stresses around the anchors increase, becoming higher than the stresses at the initial section of the contact area. The maximum and minimum stresses at the anchors change due to the change of their length, being concentrated at the deformed regions. Finally, the minimum stresses at the concrete layers have similar distributions regardless of the size of the specimen, being concentrated around points of application of displacements and of imposition of restraints (Reference Points 2, 3 and 5) and around the interface, specially at the left side. The magnitude of the stresses increases as the size of the specimens decrease.

Finally, regarding the third topic, it was possible to observe an influence of the concrete strength on the resulting loads and stresses. Concerning the load *versus* slip curve, an increase in the loads can be observed as the concrete strength class increases. A change in the slip value associated with the peak load can also be observed, leading to the conclusion that changes in ductility occur. The increase of the peak load is non-linear with the increase in concrete strength of the added concrete layer, with the variation of peak load for a fixed variation of concrete strength decreasing as the concrete strength increases. The variation of peak load was found to be negligible for changes in the concrete strength of the existing concrete layer. The slip value associated with the peak load increases as the concrete strength of the added concrete layer increases, as occurs for the peak load. However, the slip decreases with the increase of concrete strength of the existing concrete layer, which indicates a decrease in the ductility.

The distribution of displacements is also affected by the change in concrete strength classes. The portion of the bottom layer with negligible displacements decreases as the strength class increases. For the top concrete layer, the portion that presents the maximum value of displacements decreases as the ratio between concrete strength classes of the two layers increases. In the YZ plane, symmetry occurs for all models.

Regarding the damage distribution, the change in the crushing pattern between the models is not so significant, with the main change being the appearance of crushing at the top layer, near the interface, for models with higher ratio between the concrete strengths of the layers. In the cracking pattern, the main change is in the magnitude of the damage, that increases as the concrete strength classes increase.

The distribution of shear stresses along the concrete-to-concrete interface does not change significantly in shape between the models, being the higher values found at the initial section and around the anchors. However, the stresses change in magnitude, increasing mainly according to the increase of concrete strength for the added concrete layer.

The maximum and minimum principal stresses distributions along the anchorage bars are in accordance with their deformation, with concentrated stresses occurring at the deformed sections and very small stresses occurring at the rest of the bar. In the model with only normal strength concretes, all three anchors deform similarly, while in the models with at least one high strength concrete layers, there is a significant decrease in deformations comparing the first anchor (the one more to the left) to the last one. The distribution of minimum principal stresses in the concrete layers is very similar for all models, being similar to the one described in the conclusions related to the size effect section. The region with high value of stresses increases in size mainly according to the increase of the strength class of the added concrete layer.

Bibliography

1. **Holly, I. and Abrahoim, I.** Connections and Joints in Precast Concrete Structures. *Slovak Journal of Civil Engineering.* 2020, Vol. 28, pp. 49-56.

2. **Birkeland, P. W. and Birkeland, H. W.** Connections in precast concrete. *ACI Journal.* 1966, Vol. 63, pp. 345-367.

3. **Mast, R. F.** Auxiliary reinforcement in concrete connections. *Journal of the Structural Division.* 1968.

4. **Santos, P. M. D.** *Assessment of the Shear Strength between Concrete Layers.* Coimbra : Departamento de Engenharia Civil, Faculdade de Ciências e Tecnologia da Universidade de Coimbra, 2009.

5. **Santos, P. M. D. and Júlio, E. N. B. S.** A state-of-the-art review on shear-friction. *Engineering Structures.* 2012, Vol. 45, pp. 435-448.

6. **Zilch, K. and Reinecke, R.** *Capacity of shear joints between high-strength precast elements and normal-strength cast-in-place decks.* Orlando, USA : fib International symposium on high performance concrete., 2000.

7. **Palieraki, V., Vintzileou, E. and Silva, J.F.** Behavior of RC interfaces subjected to shear: State-of-the art review. *Journal of Construction and Building Materials.* 306, 2021.

8. **Palieraki, Vasiliki, et al.** Design of Interfaces Between Concretes Cast at Different Times Subjected to Cyclic Loading. *Concrete Structures: New Trends for Eco-Efficiency and Performance.* 2020.

9. **Santos, P.M.D. and Júlio, E.N.B.S.** Factors Affecting Bond between New and Old Concrete. *ACI Materials Journal.* 2011.

10. **Yang, Keun-Hyeok.** Shear Stress-Relative Slip Relationship at Concrete Interfaces. *Advances in Materials Science and Engineering.* 2016.

11. **Cattaneo, Sara, Zorzato, Giacomo and Bonati, Antonio.** Assessing method of shear strength between old to new concrete interface. *Journal of Construction and Building Materials.* 2021.

12. **EOTA.** TR049 - Post-installed fasteners in concrete under seismic action. 2016.

13. —. *EAD 332347-00-0601-v01 Connector for strengthening of existing concrete.*

14. **Comité Euro-International du Béton.** *CEB-FIP-model Code 2010.* Lausanne, Switzerland : s.n., 2010.

15. **Cornelissen, H., Hordijk, D. and Reinhardt, H.** Experimental determination of crack softening characteristics of normal weight and lightweight concrete. *Heron.* 1986.

16. **Lee, J. and Fenves, G. L.** Plastic-Damage Model for Cyclic Loading of Concrete Structures. *Journal of Engineering Mechanics, vol. 124, no. 8.* 1998, pp. 892-900.

17. **Lubliner, J., et al.** A Plastic-Damage Model for Concrete. *International Journal of Solids and Structures, vol. 25.* 1989, pp. 299-329.

18. **Hordijk, D. A.** *Local Approach to Fatigue of Concrete.* Delft University of Technology. Delft : s.n., 1991.

19. **Simulia ABAQUS 6.14.** Abaqus analysis user's guide. [Online] 2011.

20. **Focacci, F., D'Antino, T. and Carloni, C.** The role of the fiber–matrix interfacial properties on the tensile behavior. *Journal of Construction and Building Materials.* 2020.

21. **Edgmond, Nikkolas J.** *Examination of shear friction design provisions.* Missouri : Master Theses, 2018.

22. **European Commitiee For Standardization.** EN 1992-1-1 - Eurocode 2: Design of concrete structures - Part 1-1 : General rules and rules for buildings. Brussels : s.n., 2004.

23. **Genikomsou, Aiaterini S. and Polak, Maria A.** *Damaged plasticity modelling of concrete in finite element analysis of reinforced concrete slabs.* Waterloo, Canada : s.n., 2016.

24. **Palieraki, Vasiliki, Vintzileou, Elizabeth and Trezos, Konstantinos.** Shear Transfer Along Interfaces: Constitutive Laws. *Second European Conference on Earthquake Engineering and Seismology.* 2014.

25. **Soltani, Mahmoodreza.** Interface Shear Transfer in Reinforced Concrete Members: Code Evaluation, Modeling, and Testing. *All Dissertations.* 2016, Vol. 1819.

26. **Casal, Bruno Baleia.** Connections Between Concrete Layers with Different Ages. Lisboa : Instituto Superior Técnico, Universidade Técnica de Lisboa.

27. **Júlio, Eduardo N. B. S. and Branco, Fernando A. B.** Reinforced Concrete Jacketing—Interface Influence on Cyclic Loading Response. *ACI STRUCTURAL JOURNAL.* 2008.

28. **Kovacovic, M.** Shear Resistance Between Concrete-Concrete Surfaces. *Slovak Journal of Civil Engineering.* 2013.

29. **Paulay, T.** The Shear Strength of Shear Walls. Canterbury : University of Canterbury.

30. **Zhang, Xuhui, et al.** Effects of Interface Orientations on Bond Strength between Old Conventional Concrete and New Self-Consolidating Concrete. *ACI Structural Journal.* 2020.

31. **Wairaven, Joost, Frenay, Jerome and Pruijssers, Arjan.** Influence of Concrete Strength and Load History on the Shear Friction Capacity of Concrete Members. *PCI JOURNAL.* 1987.

32. **Zhang, Xuhui, et al.** Interface Shear Strength between Self-Compacting Concrete and Carbonated Concrete. *ASCE.* 2020.

33. **Kwon, eung-Jun, Yang, Keun-Hyeok and Mun, Ju-Hyun.** Mechanical Model for Shear Friction Capacity of Concrete at Construction Joints. *Advances in Materials Science and Engineering.* 2018.

34. **Mattock, Alan H., Li, W. K. and Wang, T. C.** Shear transfer in lightweight reinforced concrete. *PCI JOURNAL.* 1976.

35. **Mattock, Alan H., Johal, L. and Chow, H. C.** Shear transfer in reinforced concrete with moment or tension acting across the shear plane. *PC! JOURNAL.* 1975.

36. **Wieneke, Katrin Marie.** Horizontal Shear Design of Concrete Interfaces. 2019.

37. **Habouh, Mohamed.** Shear Transfer Strength of Concrete Placed Against Hardened Concrete. s.l. : University of Akron, 2015.

38. **Barbosa, Andre R., Trejo, David and Nielson, Drew.** Effect of High-Strength Reinforcement Steel on Shear Friction Behaviour. *ASCE.* 2017.

39. **Maili, Cheng and Jing, Ma.** Experimental Study on Shear Behavior of the Interface between New and Old Concrete with Reinforcement. *KSCE Journal of Civil Engineering.* 2017.

40. **Dias-da-Costa, D., Alfaiate, J. and Júlio, E.N.B.S.** FE modeling of the interfacial behaviour of composite concrete members. *Journal of Construction and Building Materials.* 2011.

41. **Guezouli, Samy, Lachal, Alain and Nguyen, Quang-Huy.** Numerical investigation of internal force transfer mechanism in push-out tests. *Journal of Engineering Structures.* 2013.

42. **Fang, Zhuangcheng, et al.** Shear-friction behaviour on smooth interface between high-strength and lightweight concrete. *Magazine of Concrete Research.* 72, 2020.